Experimental investigation of the characteristics of prompt gammas produced in tissue during proton therapy treatment

Jeyasingam Jeyasugiththan

Department of Physics
University of Cape Town

Thesis Presented for the Degree of
DOCTOR OF PHILOSOPHY
in the Department of Physics
UNIVERSITY OF CAPE TOWN

08 October 2014

Abstract

Protons entering matter have a finite range while photons have a gradual, exponential attenuation as they travel through material. Proton radiation therapy takes advantage of this difference, by aligning the cancerous tissue with the end of the proton range where it deposits the maximum amount of energy, resulting in significant tissue sparing compared to traditional photon therapy. These properties of protons also require a more precise delivery of the radiation since a small uncertainty in the positioning of the proton beam could result in the over- or under-dosing of critical structures. This highlights the importance of an in-vivo dose measurement technique. Due to the nature of protons, there are no primary particles exiting the patient to be used for verification purposes. One option is to use secondary radiation for dose verification purposes, like prompt gammas produced by proton-nuclei inelastic collisions.

The primary aim of this work was to report on the detection of prompt gammas and their specific characteristics when produced by the important elements of tissue, like oxygen, carbon, hydrogen and nitrogen. A number of different targets containing these elements such as water, Perspex, graphite and liquid nitrogen were irradiated in a passive-scatter proton therapy treatment facility and the gammas were detected by a high resolution 2" x 2" $LaBr_3$ detector. The measurements were carried out at iThemba LABS in Somerset West, South Africa using the proton therapy beamline. In order to determine the shielding required to sufficiently block the secondary neutrons and scattered gamma-rays emitted from the beam line elements, a significant problem in a passive-scatter proton beam, preliminary Monte Carlo simulations were performed. The energy spectra of the prompt gammas produced in the various targets was measured, looking specifically at the discrete elemental prompt gamma peaks at 4.44 MeV from ^{12}C and 6.13 MeV from ^{16}O. Measurements were also performed to investigate prompt gamma emission as a function of depth along the beam path. The depth measurements were carried out for water and Perspex phantoms at several detector positions surrounding the depth location of the Bragg peak in each material. The discrete prompt gamma-ray measurements reveal that in-vivo range verification is feasible for clinical passive-scatter proton irradiations.

The secondary aspect of this work was to develop a Monte Carlo model of the entire experimental measurement set-up including the entire iThemba LABS passive-scatter proton beam line. In recent years, the Geant4 Monte Carlo toolkit has played an important role in the development of a device for real time dose range verification purposes using prompt gamma radiation. Unfortunately, in Geant4, the default physics models were not suitable for replicating measured prompt gamma emission. Determining a suitable physics model for low energy proton inelastic interactions will boost the accuracy of prompt gamma simulations. Among the Geant4 physics build-in models, we found that the precompound model with a modified initial exciton state of 2 (1

particle, 1 hole) produced more accurate discrete gamma lines from the most important elements found within the body such as ^{16}O, ^{12}C and ^{14}N when comparing them with the available gamma production cross section data.

Using the modified physics model, we also investigated prompt gamma spectra produced in a water phantom from both a 200 MeV pencil beam and passive-scatter beam of protons. The spectra were attained using a $LaBr_3$ detector with a time-of-flight (TOF) window and BGO active shield to reduce the secondary neutron and gamma background. The simulations show that a 2 ns TOF window (1.8 ns in case of passive-scatter beam) could reduce 99% of the secondary neutron flux hitting the detector.

Finally, an absolute comparison of the Monte Carlo simulations and the experimental measurements was made to validate the Geant4 physics model. The selected Geant4 Monte Carlo model for prompt gamma-ray production underestimated the measured values of up to 10% except for the 4.44 MeV peak from the water target, which shows almost a 50% overestimation of the number of produced prompt gammas. Overall, the Monte Carlo model of the iThemba LABS proton therapy beamline performed well, matching validation treatment dose profiles to within 3% and replicating prompt gamma production numbers to within 10%. The gross overestimation for the 4.44 MeV peak produced by the water target will be investigated and may lead to changes to the physics models within Geant4. The present simulation proved able to adequately model the prompt gamma production and will continue to be used for prompt gamma studies at iThemba LABS.

Contents

Acknowledgments

Firstly, I wish to express my thanks and appreciation to my supervisor Dr. Steve Peterson of the Department of Physics, University of Cape Town for accepting me as a student and providing me with a suitable project to undertake towards achieving my PhD. His invaluable guidance and encouragement kept me focused and helped me to make key decisions during my research. I also wish to thank him for performing a great deal of proofreading and helping me achieve what I have done today.

Specially I would like to thank my friend Thirunavukkarasu Pathmathas (Pat) for his support and introducing me to this opportunity and to Steve.

I would especially like to thank Professor Andy Buffler and Mr Dieter Geduld for their assistance and moral support in the set-up of the electronics throughout the experiments and for providing valuable discussions on technical topics.

At iThemba LABS, I firstly would like to thank the director for allowing me to carry out my experiments on their premiss. Secondly, I would like to say thanks to Mr Jaime Nieto-Camero, the radiation physicist in charge of the hadron therapy program at iThemba LABS and Mr Julyan Symons, medical physicist, who assisted with the experiments and allocated the time for the experiments.

I would like to thank my friend Sivananthan Sarasanandarajah (Siva) for his support, discussions and sharing research materials with me during this time.

I am grateful to Dr. Indresan Govender for his support and giving his desktop computer for my simulation work.

I would also like to thank the Center for High Performance Computing (CHPC), CSIR Campus, 15 Lower Hope St., Rosebank, Cape Town, in South Africa for providing me access to their clusters and resources.

During the course of this work I have been fortunate to receive funding from a number of sponsors. I am grateful to the Postgraduate Funding Office at the University of Cape Town for the award of an International & Refugee Students Scholarship for the last two years of my study and for the conference travel grant in 2013. I am thankful to Professor Andy Buffler, Head of the Department of Physics for the award of a Joseph

Stone Bursary (Physics) in 2012. Finally I appreciate the support from my supervisor for his contribution over the first two years and assisting to get above-mentioned funding from various resources.

I am most indebted to Diana Peterson, the wife of Steve, for her friendship and support shown to my wife and kids during this time. It is greatly valued.

Finally, I want to thank my family, and my wife, Sureka for their encouragement, understanding, patience and loving support throughout whole period of my research work and for being willing to relocate for the duration of this process. A special thank to my brother-in-law Suthakaran Mathanasurenthiran (Sutha) who gave me invaluable encouragement and support.

Part I

Introduction

Chapter 1

Background

1.1 Aim and outline of this study

The aim of this study is to measure the discrete prompt gammas produced in tissue by examining the prompt gammas produced in water, perspex, carbon and liquid-nitrogen targets irradiated by a clinical passive-scatter proton beam of 200 MeV. The measurements were taken in cooperation with the medical division at iThemba LABS in Faure, South Africa, using the proton therapy beamline that has been used to treat patients for many years. A secondary aspect of this work was to develop a Monte Carlo model of the experimental measurement set-up including the entire iThemba LABS passive-scatter proton beam line using the Geant4 Monte Carlo particle transport code (version 9.6.p02).

This thesis is divided into four parts including an introduction (chapter 1) describing the background information for this work, including a discussion on the sources of range uncertainties that arise during proton beam radiotherapy treatment. It outlines previous research work in prompt gamma detection, as well as several proposed methods of prompt gamma imaging are also discussed. The introduction concludes with a brief motivation of this work in section 1.8.

The second part describes the materials and methodology discussed in chapters 2 and 3. In chapter 2, we report on the Monte Carlo model of the iThemba LABS passive-scatter beamline. Chapter 2 also contains methods of validation of the beamline model and the physics within Geant4. Simulations for prompt gamma spectra from a water phantom irradiated with a clinical passive and active proton beam are also reported.

Chapter 3 provides the details of our experimental study for prompt gamma detection.

The third part presents the results, discussion and conclusion of the research, divided into chapters 4, 5 and 6. Chapter 4 provides the results of all the simulations described in chapter 2. In chapter 5, the measured prompt gamma spectra from different targets are analysed and the results are used to evaluate the accuracy of the existing Monte Carlo simulations and to make comparisons with the experimental data. In chapter 6, we conclude our overall works and findings briefly.

The last part of this thesis contains Appendices. In Appendix A, we listed material definitions used in our Geant4 Monte Carlo passive beamline model whereas Appendix B provides the General Particle Source (GPS) macro commands for the modelled AmBe neutron source.

1.2 Physics of proton beam radiotherapy

According to the World Health Organization (WHO) report, about 13% of all deaths worldwide in 2008, were due to cancer. Utilization of radiation is one of the most important methods to treat localized solid tumours. Over 50% of cancer treatments are covered by radiotherapy. Nowadays, many commercially available treatment facilities, producing X-rays, electrons, protons and heavy ions, are being used for cancer treatments. Among them, proton therapy is one of the most technologically advanced methods to treat tumours seated deep in the human body while offering good dose conformity. Moreover, protons can cause less damage to the normal tissue compared to traditional beam radiotherapy. As a result, it is possible to increase the tumour dose while reducing the dose to the surrounding normal tissue or organs at risk.

In 1946, Robert Wilson proposed protons for cancer treatment and the first patient-based treatment was carried out in 1954 at the Lawrence Berkeley National Laboratory (LBNL) in the USA. A major advantage of proton beam radiotherapy over traditional radiotherapy is no exit dose beyond the tumour, as seen in Figure 1.1. This is because of the sharp distal fall-off at the end of the proton range. In contrast, as gamma-rays move through the body, they will damage tissue and organs all along their path. Figure 1.2 shows the simulated energy deposited by a proton within a water target. When a proton moves through matter, it continuously slows down by losing its energy through one or all of the following interactions: electromagnetic excitation and ionization of the atoms and molecules of the target material (called electromagnetic interactions), inelastic

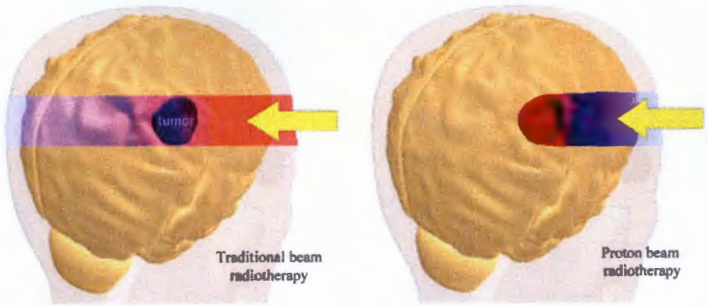

Figure 1.1: *Comparison of traditional (gamma-rays) beam radiotherapy (left) with proton beam radiotherapy (right) edited from http://www.proton-therapy.org*

and elastic nuclear interactions. The rate of energy loss is inversely proportional to the proton velocity. Therefore, the rate of energy deposit per unit length increases as the proton slows down. The proton finally deposits all of its remaining energy at a particular depth. The maximum energy deposition at the sharp peak is called the Bragg peak.

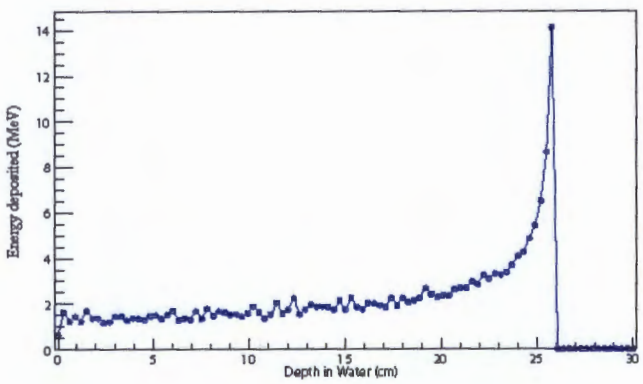

Figure 1.2: *Energy deposited by a 200 MeV proton along its track in a water phantom.*

The proton energy loss is characterized by the term *stopping power*. According to the ICRU (1993), stopping power is defined as the average energy loss per unit track length. The stopping power depends on proton energy and material in which the proton is traversing. Moreover, the stopping power is the sum of electronic (or collision) and nuclear stopping power. The *nuclear stopping power* results from the elastic nuclear collisions

between protons and nuclei in which the proton loses its energy by transferring kinetic energy to the recoil nuclei. The energy lost due to elastic collisions is less significant than collision stopping power particularly at higher proton energies. For example, a 0.1 MeV proton only contributes to 0.1% of the total energy loss (Janni (1966)). The electronic stopping power involves with the atomic electrons of the target atoms produce the primary proton energy loss via excitation or ionization. The electromagnetic interactions are the dominant mode of energy loss for low and moderate energy protons (Janni (1966)). A proton also undergoes multiple scattering while interacting with the atomic nuclei rather than the electrons and emits *bremsstrahlung* photon as a result.

In addition to electromagnetic interactions, proton inelastic nuclear interactions occur throughout the entire stopping process, but do not change the shape of the Bragg peak. This energy loss during inelastic nuclear interactions should not be neglected because it reduces the primary proton fluence as a function of depth. For a 160 MeV beam, 19.6% (about 1% per centimetre range of the beam) of the primary protons are involved in nuclear interactions as they slow down (Paganetti (2002)).

The energy loss from atomic ionization and excitation (*mass collision stopping power*) is given by Bethe-Bloch equation 1.1 (ICRU (1993)).

$$\frac{S_{col}}{\rho} = -\frac{1}{\rho}\left(\frac{dE}{dx}\right)_{el} = \frac{4\pi r_e^2 mc^2}{\beta^2}\frac{1}{u}\frac{Z}{A}z^2 L(\beta) \qquad \frac{MeV}{g/cm^2} \tag{1.1}$$

where, $r_e = e^2/mc^2$ is the classical electron radius, $mc^2 \approx 0.511$ MeV is the rest mass of an electron, $\beta \equiv v/c$ (v is the speed of proton), u is the atomic mass unit, Z and A are the atomic number and relative atomic mass of the target atom, z is the charge number of the projectile and $L(\beta)$ is called *stopping number* which is expressed by equation 1.2.

$$L = L_0(\beta) + zL_1(\beta) + z^2 L_2(\beta) \tag{1.2}$$

and,

$$L_0(\beta) = \frac{1}{2}ln\left(\frac{2mc^2\beta^2 W_m}{1-\beta^2}\right) - \beta^2 - ln(I) - \frac{C}{Z} - \frac{\delta}{2} \tag{1.3}$$

where, $\delta/2$ and C/Z are corrections for the density and shell effect, respectively, and are

negligible in the radiotherapy energy range. Therefore, for protons in the energy range 3 - 300 MeV, the mass stopping power can be written (while ignoring all negligible corrections) as seen in the equation 1.4 [Paganetti (2012a)]. The uncertainty of the mean excitation energy of the target material (I) is discussed in Section 4.2.2.

$$\frac{S_{col}}{\rho} = -\frac{1}{\rho}\left(\frac{dE}{dx}\right)_{el} = 0.3072\frac{Z}{A}\frac{1}{\beta^2}\left(ln\frac{W_m}{I} - \beta^2\right) \qquad \frac{MeV}{g/cm^2} \tag{1.4}$$

where,

$$W_m = \frac{2m_e c^2\beta^2}{1-\beta^2} \tag{1.5}$$

from equation 1.4,

$$\frac{S_{col}}{\rho} \propto \frac{1}{v^2} \tag{1.6}$$

Since the incident proton speed is very high, the initial energy loss is very low. As the proton slows down it can be clearly demonstrated using equation 1.6 that the rate of energy loss of the proton in the track is continuously increasing even if there is a very small change in speed. While the proton approaches the end of its range, the proton has a very low speed. Therefore, the rate of energy loss becomes very high and the proton loses all of its remaining energy at the end of track and gives rise to the Bragg peak.

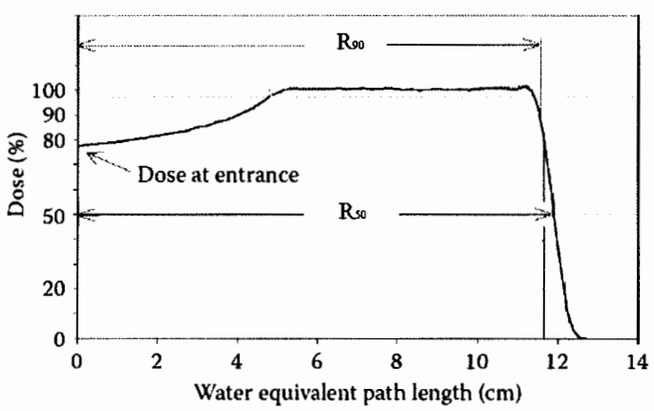

Figure 1.3: *Spread-out Bragg peak (SOBP) distribution edited from Paganetti (2012a).*

The effective depth of a proton travelling in matter before losing all its energy is defined as its *range*. It is noted that not all protons with the same energy will stop at the same position and the proton range will be broadened or spread out. Therefore, the mean projected range ($R_{50\%}$) of a proton is measured at a point on the broadened Bragg peak or the spread-out Bragg peak (SOBP) where the dose has decreased to 50% of the maximum dose as shown in Figure 1.3. However, in most proton centres, the 90% falloff position ($R_{90\%}$) in water or the 90% isodose line in a patient is considered the prescribed dose range (see Figure 1.3).

1.3 Prompt gamma creation

During a proton therapy treatment, some of the incident protons interact directly with target nuclei in the patient producing gamma-rays. These proton-nucleus interactions excite the nucleus, which de-excites very quickly (10^{-9} - 10^{-19} s) by emitting one or more gamma-rays, called prompt gamma (PG) rays. Each emitted prompt gamma ray has a characteristic energy, defined by the elemental nuclei of origin. These characteristic gamma rays (0 - 8 MeV) have been shown to closely imitate the location of the dose distribution within the patient (Polf et al. (2009a) and Min et al. (2006)). The prompt gamma creation within the tissue generally depends on the energy of the incident proton and the elemental composition of the tissue (Polf et al. (2009a)). The details of prompt gamma lines generated by proton inelastic collision with ^{12}C, ^{16}O and ^{14}N are given in Table 1.1.

1.3.1 Inelastic nuclear reactions

Inelastic nuclear reactions can occur in any of the three processes, through direct reactions, compound nuclear emissions or pre-equilibrium emissions. For low incident energy proton nuclear interactions, a compound nucleus is formed from the combination of an incident proton and the target nucleus. The incident proton remains inside the target nucleus and no emission occurs directly after the interaction. The incident proton energy is then diffused statistically among all the nucleons of the target nucleus through successive collisions and eventually transferred to the compound nucleus. It can release energy by emission of particles through statistical fluctuation that concentrates enough energy on a single nucleon or cluster (Singh and Mukherjee (1996)). The unstable equilibrated compound nucleus is in an excited quasi-stationary state between

Table 1.1: *Prompt gamma lines produced during proton inelastic reactions on ^{12}C, ^{16}O and ^{14}N. Source: Kozlovsky et al. (2002a).*

$E_\gamma(MeV)$	Transition	Reaction	Mean Life (s)
0.718	$^{10}B^{*0.718} \rightarrow$ g.s	$^{16}O(p,x)^{10}B^*$	1.0×10^{-9}
		$^{12}C(p,x)^{10}C(\epsilon)^{10}B^*$	27.8
		$^{12}C(p,x)^{10}B^*$	1.0×10^{-9}
1.022	$^{10}B^{*1.740} \rightarrow {}^{10}B^{*0.718}$	$^{16}O(p,x)^{10}B^*$	7.5×10^{-15}
		$^{12}C(p,x)^{10}B^*$	7.5×10^{-15}
1.635	$^{14}N^{*3.948} \rightarrow {}^{14}N^{*2.313}$	$^{16}O(p,x)^{14}N^*$	6.9×10^{-15}
		$^{14}N(p,p')^{14}N^*$	6.9×10^{-15}
2.000	$^{11}C^{*2.000} \rightarrow$ g.s	$^{12}C(p,x)^{11}C^*$	1.0×10^{-14}
2.124	$^{11}B^{*2.125} \rightarrow$ g.s	$^{12}C(p,x)^{11}B^*$	5.5×10^{-15}
2.313	$^{14}N^{*2.313} \rightarrow$ g.s	$^{16}O(p,x)^{14}N^*$	9.8×10^{-14}
		$^{14}N(p,p')^{14}N^*$	9.8×10^{-14}
		$^{14}N(p,n)^{14}O(e^+,\epsilon)^{14}N^{*2.313}$	102
2.742	$^{16}O^{*8.872} \rightarrow {}^{16}O^{*6.130}$	$^{16}O(p,p')^{16}O^*$	1.8×10^{-13}
3.684	$^{12}C^{*3.685} \rightarrow$ g.s	$^{16}O(p,x)^{13}C^*$	1.6×10^{-15}
		$^{13}C(p,p)^{13}C^*$	1.6×10^{-15}
3.853	$^{12}C^{*3.854} \rightarrow$ g.s	$^{16}O(p,x)^{13}C^*$	1.2×10^{-11}
		$^{13}C(p,p)^{13}C^*$	1.2×10^{-11}
4.438	$^{12}C^{*4.439} \rightarrow$ g.s	$^{16}O(p,x)^{12}C^*$	6.1×10^{-14}
		$^{12}C(p,p')^{12}C^*$	6.1×10^{-14}
		$^{14}N(p,x)^{12}C^*$	6.1×10^{-14}
4.444	$^{11}B^{*4.445} \rightarrow$ g.s	$^{12}C(p,2p)^{11}B^*$	5.6×10^{-19}
		$^{14}N(p,x)^{11}B^*$	5.6×10^{-19}
5.105	$^{14}N^{*5.106} \rightarrow$ g.s	$^{16}O(p,x)^{14}N^*$	6.3×10^{-12}
		$^{14}N(p,p')^{14}N^*$	6.3×10^{-12}
5.180	$^{15}O^{*5.181} \rightarrow$ g.s	$^{16}O(p,x)^{15}O^*$	$< 4.9 \times 10^{-14}$
5.240	$^{15}O^{*5.241} \rightarrow$ g.s	$^{16}O(p,x)^{15}O^*$	3.25×10^{-12}
5.269	$^{15}N^{*5.270} \rightarrow$ g.s	$^{16}O(p,x)^{15}N^*$	2.58×10^{-12}
5.298	$^{15}N^{*5.299} \rightarrow$ g.s	$^{16}O(p,x)^{15}N^*$	1.2×10^{-14}
6.129	$^{16}O^{*6.130} \rightarrow$ g.s	$^{16}O(p,p')^{16}O^*$	2.7×10^{-11}
6.175	$^{15}O^{*6.176} \rightarrow$ g.s	$^{16}O(p,x)^{15}O^*$	$< 2.3 \times 10^{-14}$
6.322	$^{15}N^{*6.324} \rightarrow$ g.s	$^{16}O(p,x)^{15}N^*$	1.0×10^{-15}
6.337	$^{11}C^{*6.339} \rightarrow$ g.s	$^{12}C(p,x)^{11}C^*$	$< 1.1 \times 10^{-13}$
6.476	$^{11}C^{*6.478} \rightarrow$ g.s	$^{12}C(p,x)^{11}C^*$	8.7×10^{-15}
6.741	$^{11}B^{*6.743} \rightarrow$ g.s	$^{12}C(p,x)^{11}B^*$	4.3×10^{-20}
6.790	$^{11}B^{*6.792} \rightarrow$ g.s	$^{12}C(p,x)^{11}B^*$	5.6×10^{-19}
6.916	$^{16}O^{*6.917} \rightarrow$ g.s	$^{16}O(p,p')^{16}O^*$	6.8×10^{-14}
7.115	$^{16}O^{*7.117} \rightarrow$ g.s	$^{16}O(p,p')^{16}O^*$	1.2×10^{-19}
7.299	$^{15}N^{*7.301} \rightarrow$ g.s	$^{16}O(p,x)^{15}N^*$	1.4×10^{-16}

the absorption of the incident proton and the emission of several particles with relatively low kinetic energy. Moreover, a compound nucleus can form through a number of different nuclear reaction processes and also decays through many different channels. The compound nuclear model is applied for low-energy incident protons (10-20 MeV) due to the low chance for the incident proton to escape with its identity intact from the target nuclei. It is also used for medium-weight and heavy target nuclei where the target nuclei have a large enough interior to absorb the incident proton. The particle emission from a compound nucleus is nearly isotropic because of the random collisions among the nucleons within the target nucleus.

By contrast, an increase in the incident proton energy sees a change in the reaction mechanism from the compound nucleus mechanism to the direct reaction mechanism, in which the proton interacts with only one or at most a few nucleons in the target nucleus (Williams (1991)). After interaction, either the incident proton or a target particle can escape from the composite nucleus. Also, the incident particle can pick up one or more nucleons from the target nucleus. The particle emission from a direct reaction (about 10^{-22} s) is much quicker than from a compound-nuclear reaction (about 10^{-16} s to 10^{-18} s).

However, experimentally, typical nuclear reactions are observed with a time longer than the direct reaction and shorter than compound nuclear reaction. Thus, a third mechanism, where particle emission occurs before statistical equilibrium was reached must be possible. This mechanism is known as pre-equilibrium, in which secondary particles are emitted with a relatively higher energy and a specific angular distribution. At the end of the pre-equilibrium stage, a single nucleon may be able to gain enough energy to escape from an excited composite nucleus. The emission of nucleons from a compound nucleus is known as evaporation process and is described as the escape of molecules from hot water or fluid.

1.3.2 Nuclear reaction models

As the proton energy is increased above 10 MeV (above the evaporation peak), semi-classical pre-equilibrium reaction models, such as the internuclear cascade model (INC) or the exciton model proposed by Griffin (1966) are widely used for nuclear reactions (Singh and Mukherjee (1996)).

Intranuclear cascade model (INC)

The INC model has been developed for the Monte Carlo simulation of nucleon-nucleon reactions that make use of free nucleon-nucleon experimental cross sections. The INC model is shown schematically in Figure 1.4, where a proton is incident on a target nucleus with an impact parameter b. The proton will then interact with the nucleons inside the target nucleus after travelling a certain distance. The cascade model is responsible for the individual nucleon trajectory. If an excited particle has sufficient energy to reach the nuclear surface after the cascade, it may be emitted immediately from the nucleus, as seen in Figure 1.4. Otherwise, it will fall below a cut-off value to be captured by the nucleus in order to raise the nucleus to an excited stage. At the end of each cascade, after having traced all the particles of a given cascade, the details of the residual nucleus and emitted particles are stored and a new cascade with a new impact parameter is registered. During each cascade process, several particles may be ejected and the residual nucleus generally remains in an excited state. The de-excitation of the residual nucleus generates gamma emissions. Although the INC model is accurate for protons with high incident energy (approximately 100-200 MeV), it has been successful at low energy even as low as 20 MeV (Brenner and Prael (1989)).

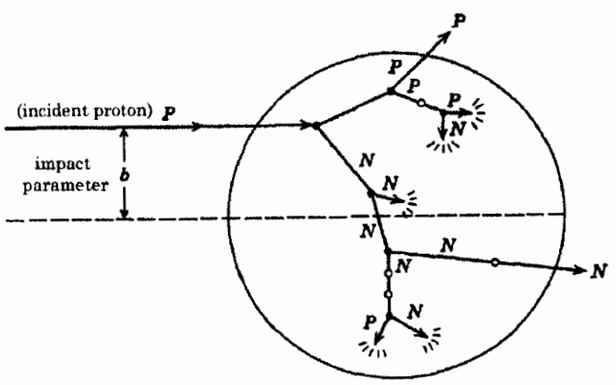

Figure 1.4: *A schematic representation of an intranuclear cascade generated by a proton in a target nucleus, where, the solid circles indicate points of collisions and open circle represent collisions forbidden by the Pauli exclusion principle. The short arrows indicate the positions of nucleons captured to contribute the overall excitation. Source: Friedlander et al. (1955).*

Exciton model

Figure 1.5 shows a schematic diagram of a simple exciton[1] model. As the target nucleus is initially in the ground stage ($n = 0$), there are no vacant energy levels below the Fermi energy E_f and all energy levels above are empty. Assume a proton with energy E enters the target nucleus where it forms a state with exciton n = 1 (1p + 0h). This is the initial stage of a nuclear interaction and the incident proton may escape from the target nuclei field without any interaction with the nucleon. In this case, the reaction will be completely elastic. By contrast, a proton interaction with an individual target nucleon will raise the nucleon above the Fermi level and result in a vacancy below the Fermi level. Thus, the absorption of an incident proton by a target nucleon forms an exciton state of n = 3 (2p + 1h). At this stage, either of the excited particles may be emitted from the nuclei if it has sufficient energy to escape. Otherwise, there will be a two-body interaction between either the excited particles and the nucleons under the Fermi energy level to form an exciton state of n = 5 (3p + 2h) or the excited particles themselves that will form an exciton state of n = 3 (2p+1h) (or back to the initial stage with an exciton n = 1). Therefore, the transition changes the excitons by 0 or ± 2, which is proportional to the level density of excited states. Once the equilibrium state (n = 0) is reached (the number of excitons will be a constant after equilibrium state), the pre-equilibrium model will be handled by evaporation model.

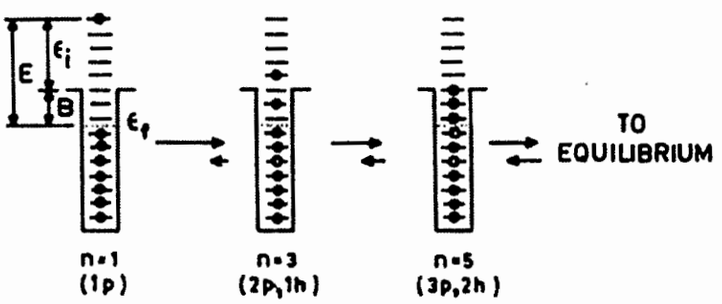

Figure 1.5: *A schematic diagram of the equilibrium process in the exciton model, where, E is the excitation energy, n is the number of excitons ($n = p + h$), E_f is the Fermi energy and E_i is the energy of the incident particle. The solid and open circles indicate particles (p) and holes (h), respectively. Source: Singh and Mukherjee (1996).*

[1] the excited degrees of freedom (n) that is the sum of particles (p) excited above the Fermi level and holes (h) under the Fermi level (i.e. $n = p + h$)

1.4 Sources of range uncertainty

A disadvantage of proton radiotherapy is the uncertainty in the proton range while calculating the dose, preparing the patient for the treatment or delivering the prescribed dose. Liu et al. (2007) has reported that if the water equivalent depth (WED) changes by 1 cm, there is at most a 3-5% variation in depth dose for 10 MeV photon, but up to 90% variation in depth dose for a typical proton beam (see Figure 1.6). Further, Liu demonstrated that the result of this range uncertainty could cause either *undershoot* (lowered tumour dose because of missing tumour region being treated), or *overshoot* (treating normal tissue beyond the tumour with the full dose), as demonstrated in Figure 1.6. Therefore, in order to deliver the accurate prescribed dose to the planned tumour region, verifying the proton range during the treatment would be extremely desirable.

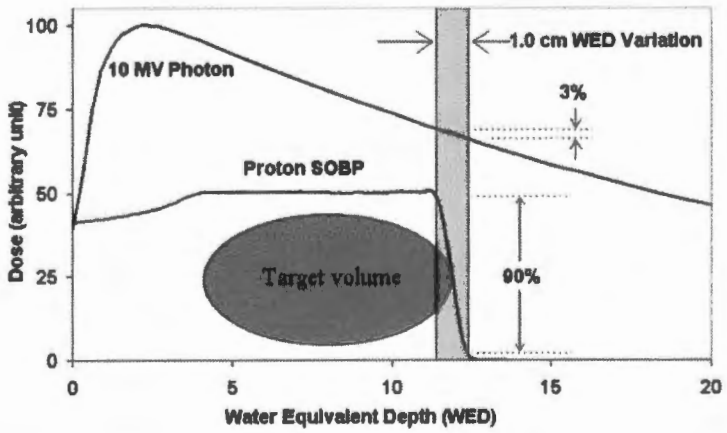

Figure 1.6: *Dose difference for a 1.0 cm water equivalent depth of a 10 MeV photon beam and a SOBP proton beam editted from Liu et al. (2007).*

Table 1.2 summarizes the estimated range uncertainty values during treatment planning, preparation and delivering dose. In proton beam radiotherapy, the dose calculation is based on computed tomography (CT) images in which the tumour volume is defined using density or contrast variation of tissue. The precision of the proton treatment planning depends on stopping power values that are converted from Hounsfield values of the CT image obtained through a calibration curve. The Hounsfield scale is defined as the transformation of linear attenuation of x-rays into the radiodensity of water (Schaffner and Pedroni (1998)). The uncertainty in stopping power is not

Table 1.2: *Range uncertainties during treatment planning, preparation and delivering dose.*

Source of range uncertainty	Range uncertainty	Reference
CT image and conversion of stopping power		
for bone	±1.8%	Schaffner and Pedroni (1998)
for soft tissue	±1.1%	Schaffner and Pedroni (1998)
Mean excitation energy (I-value)	±1.2%	Matsufuji et al. (1998)
Image artefact in the CT		
tooth filling	−3%	Jaekel and Reiss (2007)
titanium hip prosthesis	−5%	Jaekel and Reiss (2007)
steel	−18%	Jaekel and Reiss (2007)
Beam reproducibility	±0.2%	Paganetti (2012c)
Patient set up	±0.7%	Paganetti (2012c)
Compensator design	±0.2%	Paganetti (2012c)
During commissioning (water)	±0.2%	Paganetti (2012c)
Anatomic changes (patient weight changes)		
gained weight	+8 *mm*	Albertini et al. (2008)
lost weight	−13 *mm*	Albertini et al. (2008)
Estimated overall uncertainty	3.0–3.4%	

only due to the HU conversion but also caused by the I-value[1]. Matsufuji et al. (1998) suggested a ±0.82% safety margin on treatment planning for range uncertainty due to CT number variation. Also, the attenuation of the x-rays in any metal is very strong, therefore an image artefact in the CT image by the presence of any surgical metal or tooth filling will directly affect the CT number, and hence, lead to huge uncertainty in the proton range (Wei et al. (2006), Jaekel and Reiss (2007) and Newhauser et al. (2008)). Furthermore, the uncertainty due to reproducibility of the proton beam for daily treatments and in patient set-up are ±0.2 and ±0.7 % respectively. In the passive beam proton delivery, there is an additional uncertainty of ±0.2 %, due to compensator design. Moreover, anatomic changes because of patient weight changes, tumour mass reduction or filling of internal cavity during the course of proton treatment cause a significant range uncertainty which is up to +8 mm while the patient gained weight and up to -13 mm while the patient lost weight. The overall uncertainties of the proton range calculation for most clinical sites is in the range of 3.0–3.4%.

Nowadays, in addition to the prescribed range, a safety margin is being applied to ensure tumour coverage, for instance, 3.5% + 1 mm at the Massachusetts General Hospital

[1] mean ionization or excitation energy

(MGH) in Boston, 3.5% + 3 mm at the MD Anderson proton therapy center in Houston, the Loma Linda University Medical Center and the Roberts Proton Therapy Center at the University of Pennsylvania and 2.5% + 1.5 mm at the University of Florida Proton Therapy Institute (Paganetti (2012c)). However, applying these additional safety margins leads to overshoot and damages normal tissue surrounding the target (Trofimov et al. (2007) and Lu (2008)). As a result, there is significant interest in developing a method to verify the range of protons during treatment.

1.5 Positron annihilation gammas for in-vivo treatment verification

In proton beam radiotherapy, nuclear fragmentation reactions between incident protons and the target nuclei produce short-lived positron emitted isotopes; ^{15}O ($t_{1/2}$ = 2.04 min), ^{14}O (1.18 min), ^{13}N (9.96 min), ^{11}C (20.39 min) and ^{10}C (0.32 min). Among them ^{11}C and ^{15}O are easily observed isotopes as seen in Figure 1.7. The range of positrons in tissue is very short (a few millimetres) and will then annihilate with an electron in the surrounding tissue. During the positron annihilation process, two back-to-back gamma-rays of equal energy 0.511 MeV are created via the reaction $e^+ + e^- \rightarrow \gamma + \gamma$ which can then be used for positron emission tomography (PET) imaging (Parodi et al. (2002), Vacchio et al. (2007) and Fourkal et al. (2009)). The use of a PET scanner for range verification was proposed by Maccabee et al. (1969) and is the only currently available method that clinically implements dose verification either immediately following treatment (on-time) or sometime after the treatment (Parodi et al. (2008)).

Immediate range verification using PET is limited because of long half-lives (1-20 min) of the relevant nuclear reaction products. Therefore, the post-treatment verification option is preferred for dose verification (Parodi et al. (2007) and Knopf et al. (2011)).

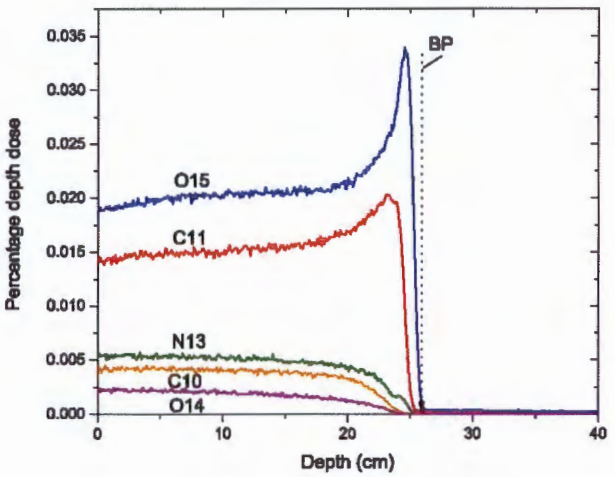

Figure 1.7: *Simulated distribution of positron emitted isotopes created along the path of 200 MeV proton in a water phantom.*

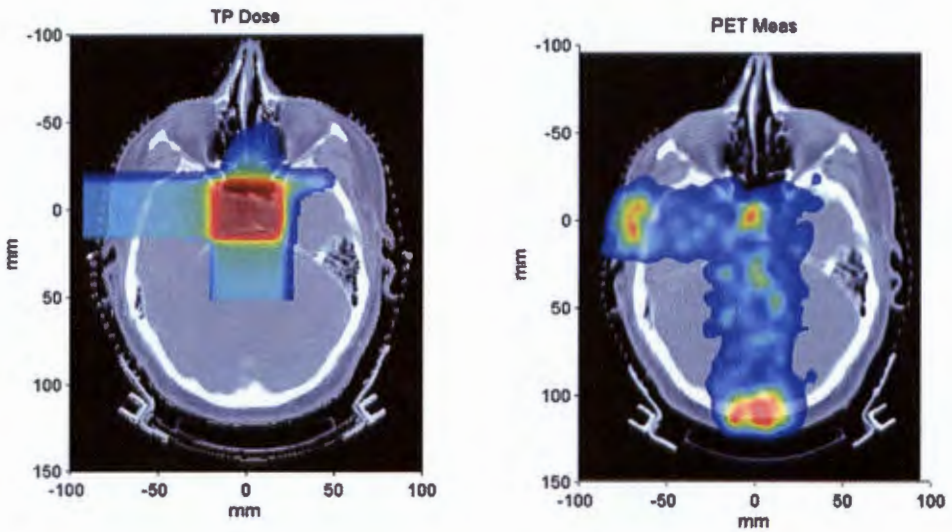

Figure 1.8: *Treatment planning (left) and measured activity using PET/CT (right). Source: Parodi et al. (2007).*

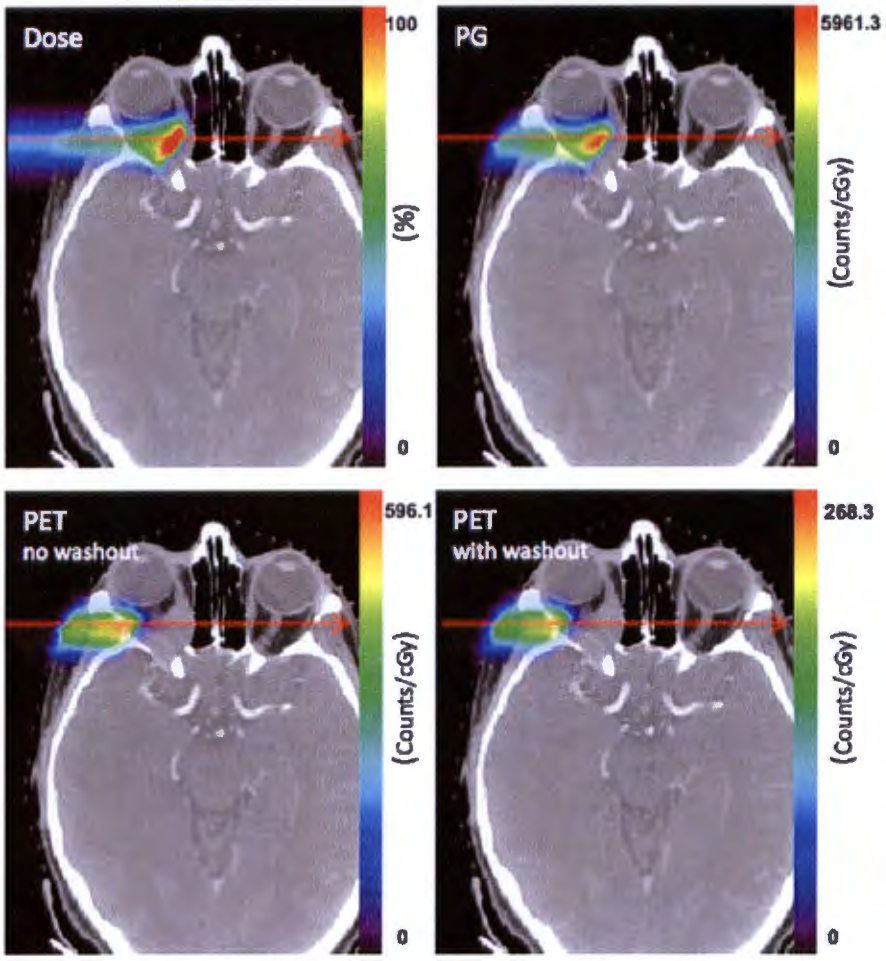

Figure 1.9: *Top: Dose distribution (left)and simulated PG (right) and bottom: PET distribution without (left) and with washout (right). Source: Moteabbed and Paganetti (2011).*

Parodi et al. (2007) investigated the feasibility of using PET/CT for post-proton treatment verification. The PET/CT image seen in Figure 1.8 (edited from Parodi et al. (2007)) was performed 20 minutes after the treatment delivery with an acquisition time of 30 minutes. The spatial reproducibility of the measured activity distribution from PET/CT has been reported to be within 1 mm (Parodi et al. (2007) and Knopf et al. (2009)). However, the quantitative agreement between the measured and planned distributions is complicated by many factors such as blood perfusion, tissue composition, motion of internal organs and co-registration uncertainties. Also, the image quality is limited by the number of positrons created during a treatment fraction. In proton

radiotherapy, the production of positron-emitted isotopes is very sensitive to tissue elemental composition. Even though the spatial reproducibility of the measured activity distributions can be achieved within 1 mm, the range can only be verified with an accuracy of $1-2$ mm in the best case scenario of a low blood-perfused bony structures of the head-and-neck patient with accurate co-registration of the imaging and planned treatment position (Parodi et al. (2007) and Knopf et al. (2009)). In contrast, in soft tissue, blood perfusion continuously wash-out the positron-emitted isotopes (Parodi et al. (2008)). Therefore, the wash-out process introduces a discrepancy between measured and expected spatial accuracy of about 4 mm, if the proton beam-end position is situated within the soft tissue (Knopf et al. (2009)). Unfortunately, the quantitative spatial accuracy due to the patient motion during the long imaging time (it is about 30 mm) of PET/CT is relatively high, possibly up to 3 cm (Knopf et al. (2009)).

Based on these results, the treatment verification by PET/CT is seen to be insufficient at this time. Yet, it so far is the only available method that can be used as an *in-vivo* proton range verification device until a more precise method for online verification is developed.

1.6 On-line verification using prompt gammas

Prompt gamma (PG) production rates are approximately 10 times higher than the number of gammas produced by positron annihilation in the therapeutic dose rate range (Moteabbed and Paganetti (2011)). Moreover, geometrical interface between the detector and the treatment gantry is not required for PG image reconstruction because there are no coincidence events. The first patient based comparison between prompt gamma imaging and positron emission tomography (PET) was studied in detail by Moteabbed and Paganetti (2011). It can be seen in Figure 1.9 where the PG and PET gamma distributions for the same treatment plan CT were simulated for comparison. The comparisons confirmed that on-line verification using the PG method has an advantage over the PET method when an active beam is used to treat a small target. Furthermore, it was reported that the PG distribution was 5 mm to 1 cm closer to the dose at both the 50% and 20% distal falloff positions than the PET. Unfortunately, no direct correlation between PG and dose was found when using a passively scattered beam.

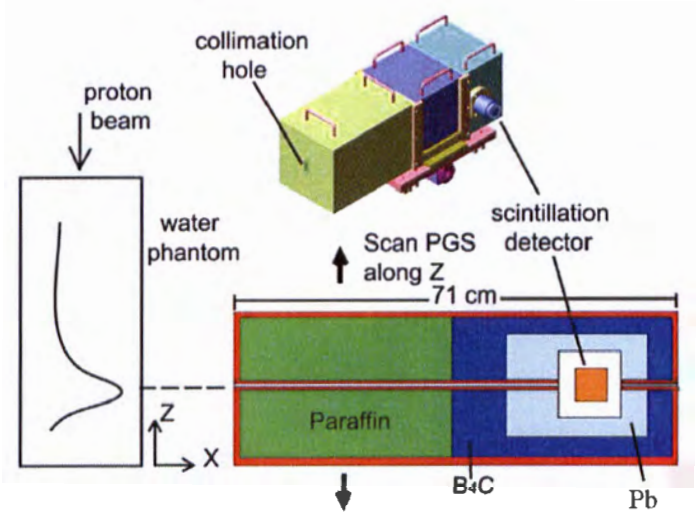

Figure 1.10: *The prompt gamma scanning system to verify proton range experimentally developed by Min et al. (2006).*

Within the last few years, detection of instantaneous prompt gamma emissions have been proposed as a suitable and alternative method over PET/CT to verify depth dose distribution clinically (Min et al. (2006), Polf et al. (2009a), Polf et al. (2009b) and Testa et al. (2010)). However, no developed prompt gamma imaging system exists to date.

The first prompt gamma scanning system was designed by Min et al. (2006) to experimentally locate the distal fall-off of the proton dose distribution. It is seen in Figure 1.10, and was built using three layers of shielding to stop neutrons from the phantom: the paraffin layer to moderate the fast high energy neutrons, the B_4C layer to capture low-energy neutrons and the lead block to attenuate neutron-captured gamma rays. The beam scan was performed perpendicular to the proton beam. A CsI(Tl) scintillator was used to detect the prompt gammas after travelling through a long collimated hole from the water phantom. In Figure 1.11, the depth dose curve measured in the water phantom by the ionization chamber was compared with the prompt gammas measured by the PG scanning system, for which gammas of energy over 4 MeV were summed. In conclusion, the correlation between the depth dose and the prompt gamma distribution clearly demonstrate the feasibility of using prompt gammas for online range verification.

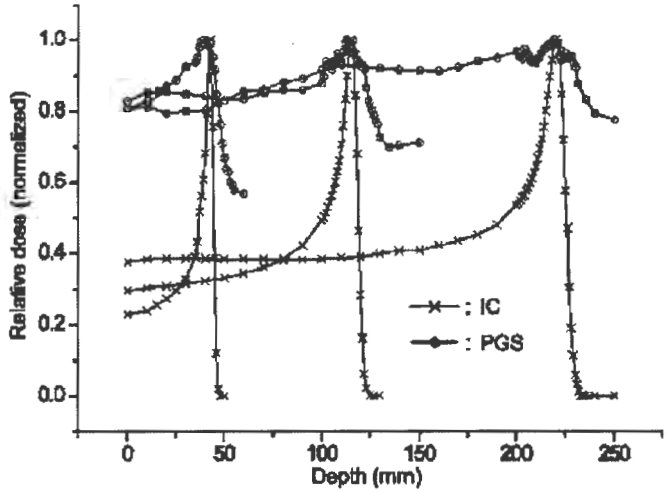

Figure 1.11: *Comparison of the Bragg Peak (depth dose) measured by an ionization chamber (IC) with the prompt gamma scanning system (PGS) measurements at proton energies of 100, 150 and 200 MeV. Source: Min et al. (2006).*

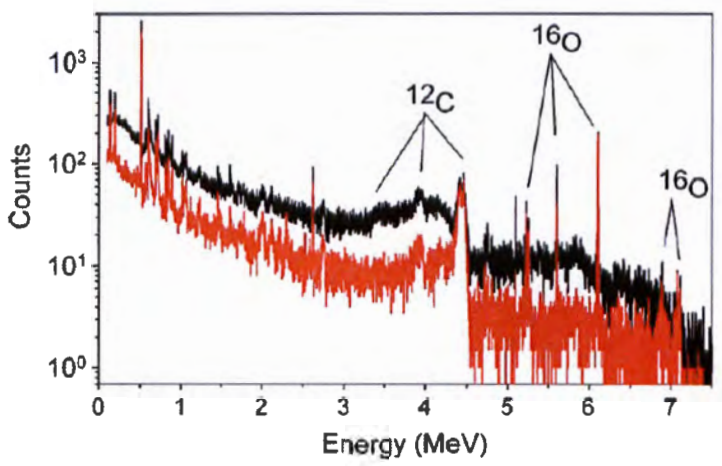

Figure 1.12: *Prompt gamma spectra emitted from Lucite measured with the passive lead shielding (black) and the active BGO shielding (red). Source: Polf et al. (2009b).*

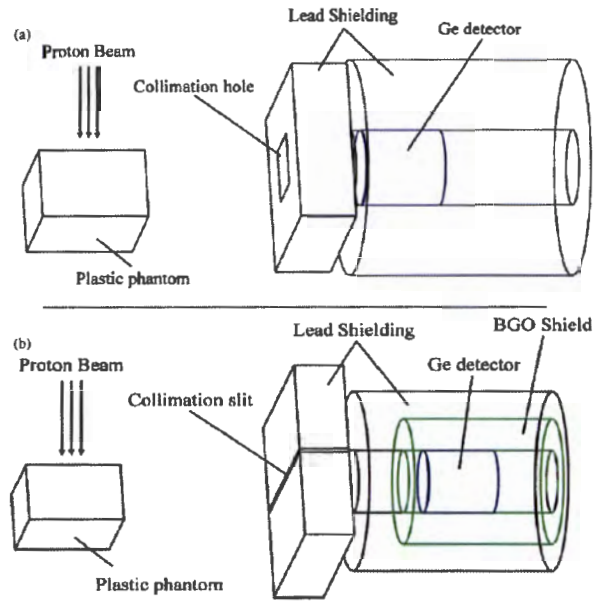

Figure 1.13: *Experimental setup of prompt gamma measurements with (a) passive shield and (b) an active shielding. Source: Polf et al. (2009b).*

An experimental measurement of prompt gamma-ray spectra emitted from a plastic phantom was performed by Polf et al. (2009b). The measured spectra are shown in Figure 1.12. As illustrated in Figure 1.13, the energy spectra were acquired by a cylindrical high purity germanium (HPGe) detector with active and passive shielding. A 2.5 cm thick lead collimator having a 2 cm x 2 cm square hole was used for the measurement with the passive shielding and it was replaced by a 4 cm slit type collimator in the active shielding configuration. The purpose of the active shielding was to avoid the continuous Compton background signal in the measured spectra due to the incomplete energy deposition of incident prompt gammas within the detector. As seen in Figure 1.12, peaks at 6.13 MeV from oxygen and 4.44 MeV from carbon were easily identified in both measured spectra with active and passive detector shielding. Also their single and double escape peaks were clearly visible. Furthermore, the use of active shielding reduced 40-70 % of the Compton scattered signal and increased the peak to background ratio over the entire energy range. As a result, the high energy peak of 7.12 MeV from oxygen could also be identified.

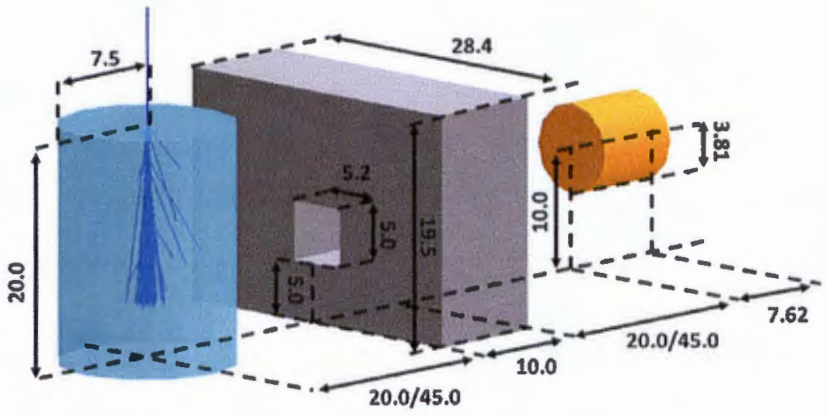

Figure 1.14: *Experimental setup of prompt gamma measurements with a NaI detector at 50 cm. All the dimensions are in cm. Source: Smeets (2011-2012).*

The prompt gamma creation within the tissue is generally dependent on the energy of the incident proton and the elemental composition of the tissue (Polf et al. (2009a). In addition, the PG signal intensity is also dependent on the concentration of elements within the tumour. Polf et al. (2013) showed the emission of the 6.13 MeV line is directly proportional to the amount of oxygen in the tumour volume, and that the 4.44 MeV signal was dependent not only on the concentration of oxygen but also on the carbon concentration. As a consequence, measuring this 6.13 MeV gamma over the course of a treatment cycle could help to track changes in the oxygenation levels and blood flow of tumour and could be used to readjust the treatment plan accordingly.

Smeets et al. (2012) made measurements of prompt gammas emitted from a PMMA ($C_5O_2H_8$) target using a NaI detector with a 160 MeV proton pencil beam. The experimental geometry is shown in Figure 1.14 where the collimator was 5.2 cm wide, 5.0 cm high and 10 cm thick. The measured spectra are shown in Figure 1.15 which were acquired during 120 s with a beam current in the range of 0.02 - 0.03 nA. Fast secondary neutrons produced together with the prompt gamma rays reached the detector and obscured the prompt gamma signal. Therefore, the spectra obtained with the collimator closed were subtracted from the spectra measured with the collimator open in order to reduce both the secondary neutrons from the target passing through the lead shielding and the secondary radiation scattered from the treatment nozzle and room walls. In the spectra, the 4.44 MeV and 6.13 MeV peaks and their single and

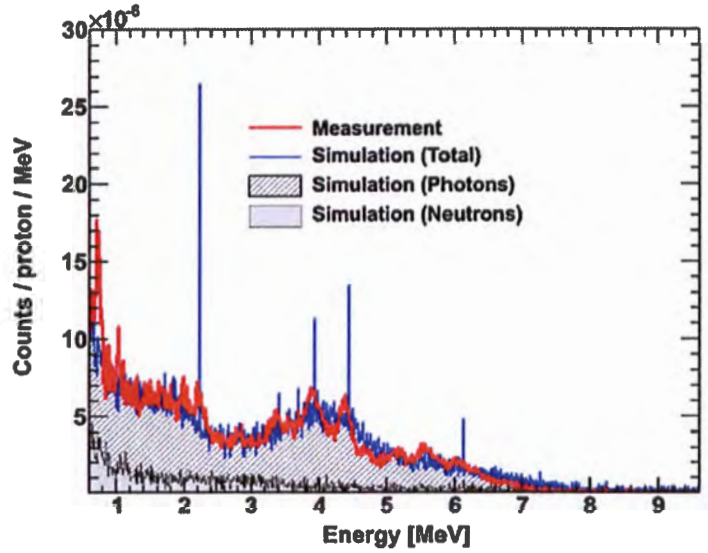

Figure 1.15: *Measured and simulated prompt gamma spectra emitted from PMMA phantom for a 160 MeV proton beam at 50 cm distance. Source: Smeets (2011-2012).*

double escape peaks were visible. However, high energy peaks at 6.92 MeV and 7.12 MeV could not be seen.

Biegun et al. (2012) proposed a method of shifting the time-of-flight (TOF) window to reject the neutron contamination in the PG signal. Their Monte Carlo simulation confirmed that the TOF window produced significant neutron background rejection. The TOF is defined as the time difference between the time when a prompt gamma is detected by the detector (stop pulse) and the time of a short RF pulse, produced when the protons enter the target (start pulse). The time of flight for photons is shorter than that for the neutrons. Therefore, the detector will be disabled for the later-arriving neutrons and as well as the background gamma rays.

Recently, Verburg et al. (2013) implemented this TOF technique into their experimental prompt gamma measurements on an active-scanning proton therapy beamline. The spectra emitted from a water target seen in Figure 1.16 were measured 9 mm before the 80% dose fall-off level (R_{80}) with a 2 ns time window using a cylindrical LaBr3 (5% Ce) detector. The 80% dose fall-off level is defined at a point on the Bragg peak where the dose decreased to 80% of the maximum dose. An active shielding of BGO ($Bi_4Ge_3O_{12}$) crystal surrounding the detector was used to reduce both the Compton background

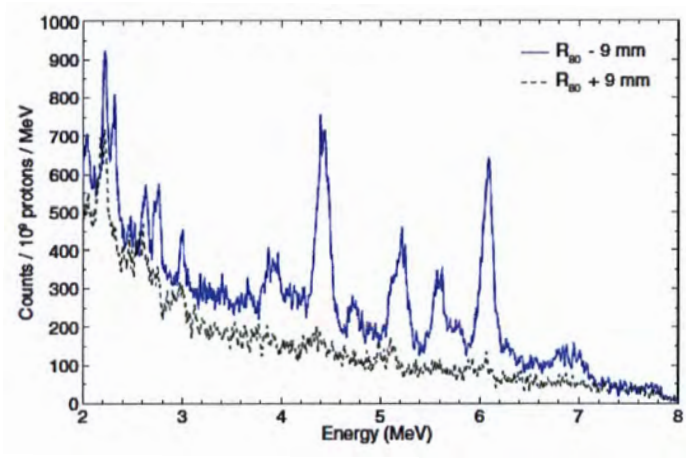

Figure 1.16: *Prompt gamma spectrum emitted from a water phantom performed with a 2 ns time window. Source: Verburg et al. (2013).*

and the neutron-induced gamma ray background by anti-coincidence methods. The detector was placed perpendicular to the beam direction 30 cm away from the surface of the water phantom and there was a 15 cm-thick collimator between them with a 4.8 mm slit opening. The prompt gamma lines at 4.44, 5.2 and 6.13 MeV were clearly resolved. Moreover, the correlation between prompt gamma emission and depth dose was reasonable.

All these prompt gamma studies were carried out using active-scanning proton beamlines. Unfortunately, during passive-scatter beam radiotherapy, additional secondary radiation such as neutrons and photons created in the beam line elements are concerns for prompt gamma measurements. The secondaries produced along a passive scatter beam line can be minimized using proper shielding and collimators. However, neutrons or secondary gamma rays produced in the final collimator and in the patient can not be avoided and produces additional signal in the detector that may hide the desired prompt gamma signal.

1.7 Proposed prompt gamma imaging devices

A number of devices have been proposed that use prompt gamma radiation for online proton range verification. Some of them have already been discussed in section 1.6. All of these devices have been designed for use with an active-scanning proton or carbon beam. Early prompt gamma imaging devices contained a single lead collimator

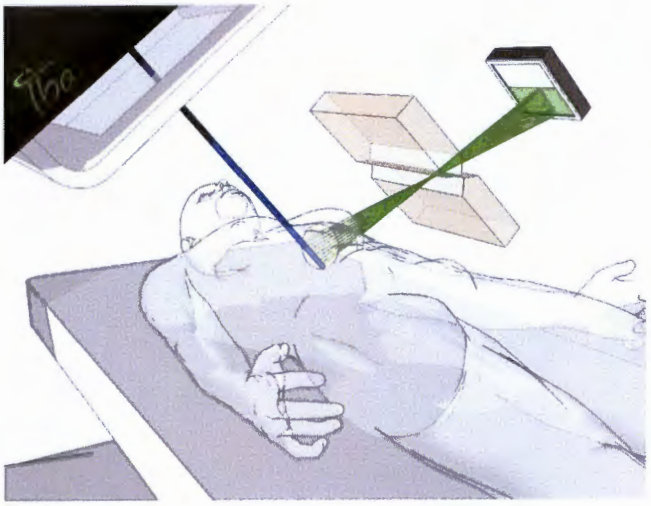

Figure 1.17: *Prompt gamma detector with slit collimator and prototype HiCam gamma detector. Source: Smeets (2011-2012).*

mounted perpendicular to the beam axis in order to scan the proton or carbon ion range in a phantom by moving it along the beam direction (Min et al. (2006), Testa et al. (2008) and Polf et al. (2009b)). Kim et al. (2009) constructed a pinhole camera to scan the proton range in a water phantom. The slit and pinhole cameras can only produce a one-dimensional prompt gamma distribution. A first prototype device consisting of a slit collimator with a knife-edge aperture and a HiCam gamma detector (High resolution Camera) was successfully built and tested for real-time range monitoring by Smeets (2011-2012). Figure 1.17 shows the arrangement of the device with the slit collimator mounted between the patient and the camera. The prototype camera projected the one-dimensional prompt gamma distribution and was therefore well suited only for a single pencil beam.

An electronically collimated (or non-collimated) detector system, called the Compton camera, is currently being investigated as an alternative method for on-line treatment verification (Richard et al. (2009), Richard et al. (2010), Peterson et al. (2010), Robertson et al. (2011) and Roellinghoff et al. (2011)). The Compton camera can produce either 2D or 3D prompt gamma images. The design of a Compton camera is completely different from a collimated camera. The initial prompt gamma energy and direction are calculated from the energy deposition and interaction position information gathered from intermediate detector stages and a final absorber stage. The detection efficiency is limited due to the smaller number of successive interactions at

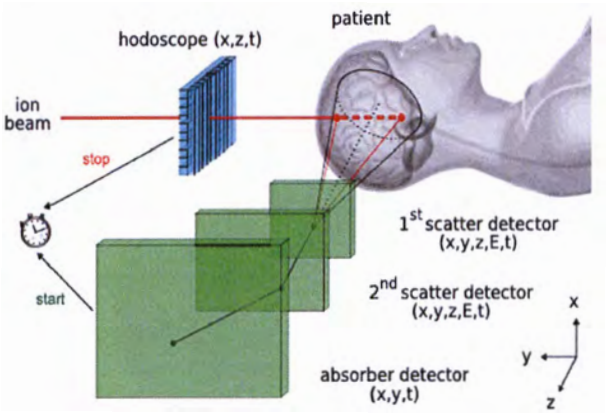

Figure 1.18: *Compton camera detection system. Source: Richard et al. (2009).*

different stages compared to the number of incident particles. The traditional Compton camera consists of a single detector composed of a stack of scatterers to improve the detection efficiency (Roellinghoff et al. (2011)). A three-stage Compton camera with two Compton scatterers is shown in Figure 1.18. To produce an active event, a photon must undergo at least one Compton scatter in the first or second detector and at least one interaction in the third absorber detector. It is therefore possible to confine the direction of the original prompt gamma along the surface of a reconstructed cone. The line drawing from the second scattered point to the first gives the direction of axis of the cone. The Compton scattering angle at the first detector is the half-angle of the cone. This scattering angle is dependent on the exact position of the gamma interaction on each scatterer. Therefore, position uncertainty will affect the image resolution (Peterson et al. (2010)). Moreover, to determine the total energy deposited, the remaining gamma energy must be absorbed completely by the absorber, but the higher energy gamma rays are able to escape easily from the absorber. So far, the feasibility of Compton camera for real-time monitoring have not yet been reported experimentally. However, the Compton camera have already been optimized with Monte Carlo simulation (Peterson et al. (2010) and Robertson et al. (2011)).

1.8 Motivation for this study

As introduced in this chapter, the detection of prompt gammas remains a challenge in developing a device for online range verification for use with proton and ion beam radiotherapy treatments. These challenges drive the motivation for this work and result in the two specific aims for the thesis. 1. The measurement of prompt gamma production from elements found in tissue in the clinical passive-scatter treatment environment. 2. The development of a Monte Carlo model of the experimental setup for preliminary predictions regarding the measurements, for comparison to final measured results and investigation into the physics behind the simulated results.

Specific Aim 1

A number of different prompt gamma experimental measurements have been completed or are on-going, but all of them have been performed for active (or pencil beam) irradiation. Although active-beam proton therapy is continuing to grow in popularity, passive-scatter proton therapy is still the dominant form of treatment and any prompt gamma imaging device will need to operate in this environment. There are a number of challenges for passive-scatter, such as the additional secondary radiation activated in the beam line elements and in the final collimator, but prompt gamma detection is still possible. The objective of this work is to perform the first prompt gamma measurements using a clinical passive-scatter proton beam. These measurements will look at the most likely discrete prompt gammas emitted from a tissue by examining those produced in water, Perspex, carbon and liquid-nitrogen targets.

Specific Aim 2

The transition from simulation to experiment can be challenging, but in the design process, both are critical tools. In order to produce an effective design, both tools need to be in agreement, producing identical results. The aim of this work is to develop a Monte Carlo model of the experimental setup (proton beam line, phantom set-up and detector) that can be used to predict experiment in the preliminary stage of research and to compare the experimental measurements in the final stage. This comparison will be crucial for investigation into how this prompt gamma production processes are modelled within Geant4. Thus, the plan is also to test various Geant4 physics models for discrete gamma emission from the excited states of ^{16}O, ^{12}C and ^{14}N, the most abundant elements in human tissue, against the currently available experimental cross-section data. In addition, we will look at several Geant4 parameters (number of excitons (n),

Doppler broadening, Fermi breakup and Geant4 inelastic reaction cross-section data set) and try to identify areas of weakness. In the end, this will all work towards lining up the simulations as closely as possible to the experimental cross section data and our experimental measurements. The Geant4 beamline model will be validated against standard proton therapy calibration measurements and the response of the gamma detectors will be modelled using a uniquely-determined detector response function.

Part II

Materials and Methods

Chapter 2

Geant4 Monte Carlo model for the prompt gamma simulations

This chapter reports on the Monte Carlo model developed for the prompt gamma simulations. The prompt gamma experimental measurements were carried out at the passive-scatter proton therapy facility at iThemba LABS (Laboratory for Accelerator Based Sciences) in Somerset West, South Africa. A Monte Carlo model of the entire experimental set-up including the beam line elements and both NaI and $LaBr_3$ detectors was developed and is based on the Geant4 Monte Carlo code (version 9.6.p02). First, we describe the method of Geant4 physics validation, and then the design of the Monte Carlo model of the iThemba LABS passive-scatter beam line and detectors. Finally, we discuss the prompt gamma simulation using both pencil beam and passive scatter beam models.

2.1 The Geant4 simulation toolkit

Geant4 is an object-oriented toolkit and implemented in the C++ environment (Agostinelli et al. (2003)). It is being used to simulate the interactions of particles transversing through matter in the fields of particle physics, nuclear physics, astrophysics, accelerator design and medical physics. The first version of the Geant4 was released in 1998, and in the following year, the Geant4 collaboration was established for further developments, maintenance and user support. Our simulation work was based on Geant4 (version 9.6.p02) released in 2013. Geant4 has been already successfully implemented in proton therapy treatment nozzle applications (Paganetti et al. (2004), Cirrone et al. (2005) and Peterson et al. (2009)). Because of its flexibility and transparency, Geant4 provides a well-defined interface to connect external software tools and allows these other tools to use its components. In addition, Geant4 allows users to develop their own geometry and material, set relevant physics lists, produce a range of source particles and provides access to any desired output data.

In the present thesis, three different Geant4 inelastic nuclear reaction models (the binary cascade (BIC), precompound (PRECO) and intra-nuclear cascade (INCLXX)) and the relevant cross-section data sets (Willish and Axen (WA) and Tripathi (TP)) were tested with different settings as summarised in Table 2.1. The physics models are described in the following sections.

Table 2.1: *Details of the physics models and settings used to evaluate the prompt gamma emission from elements ^{12}C, ^{16}O and ^{14}N. *Combined model was considered with the BIC model used below 19 MeV, the INCLXX model used between 19 MeV and 40 MeV, the PRECO model used above 40 MeV and Fermi break-up was activated below 20 MeV.*

Sim	Elements	PG energy (MeV)	Cross -section	Fermi breakup	Physics Model	Excitons number
1	^{12}C	4.44	WA	No	BIC	3
2	^{12}C	4.44	WA	No	BIC	2
3	^{12}C	4.44	WA	No	PRECO	3
4	^{12}C	4.44	WA	No	PRECO	2
5	^{12}C	4.44	WA	No	INCLXX	N/A
6	^{12}C	4.44	TP	No	BIC	3
7	^{12}C	4.44	TP	No	BIC	2

Continued on next page

Table 2.1 – *Continued from previous page*

Sim	Elements	PG energy (MeV)	Cross -section	Fermi breakup	Physics Model	Excitons number
8	^{12}C	4.44	TP	No	PRECO	3
9	^{12}C	4.44	TP	No	PRECO	2
10	^{12}C	4.44	TP	No	INCLXX	N/A
11	^{16}O	6.13 4.44 6.92 7.12	WA	<20MeV	PRECO	2
12	^{16}O	6.13 4.44 6.92 7.12	WA	No	PRECO	2
13	^{16}O	6.13 4.44 6.92 7.12	TP	<20MeV	PRECO	2
14	^{16}O	6.13 4.44 6.92 7.12	WA	<20MeV	BIC	2
15	^{16}O	6.13 4.44 6.92 7.12	WA	<20MeV	PRECO	2
16	^{16}O	6.13 4.44 6.92 7.12	WA	No	INCLXX	N/A
17	^{16}O	6.13 4.44 6.92 7.12	WA	<20MeV	*COMBINED	2
18	^{14}N	0.728	TP	No	BIC	2

Continued on next page

Table 2.1 – *Continued from previous page*

Sim	Elements	PG energy (MeV)	Cross -section	Fermi breakup	Physics Model	Excitons number
		1.635				
		2.313				
		2.793				
		3.378				
		3.890				
		5.106				
		7.027				
19	^{14}N	0.728	TP	No	INCLXX	N/A
		1.635				
		2.313				
		2.793				
		3.378				
		3.890				
		5.106				
		7.027				
20	^{14}N	0.728	TP	No	PRECO	2
		1.635				
		2.313				
		2.793				
		3.378				
		3.890				
		5.106				
		7.027				
21	^{14}N	0.728	WA	No	PRECO	2
		1.635				
		2.313				
		2.793				
		3.378				
		3.890				
		5.106				
		7.027				

2.1.1 Geant4 parameter settings

Primary protons are generated using the Geant4 general particle source package (GPS) which has many common pre-defined options for particle generation operating via interactive user interface (UI) commands. The accuracy of particle tracking is limited by the secondary particle production threshold (or range cut) and the maximum step size (or step max). When a charged particle transverses matter, it loses its energy by electromagnetic interactions between the particle and the atoms in the material producing secondary particles. If the threshold is reached, the particle stops producing secondaries and deposits its remaining energy locally by the process of discrete or continuous energy loss. In Geant4, the threshold energy is defined by a distance which is converted into a threshold energy at initialisation according to the particle type and target material; the particle is then tracked until it reaches the threshold energy. It is also possible to extend the lowest-energy threshold limit for all particles down to 1 keV in the entire simulated volume. The choice of range cut mainly depends on the size of the sensitive element within the simulated volume and available CPU. In contrast, the step max is applied for any particle and limited by all processes assigned to the particle. The step max is the maximum distance allowed for a particle before the next interaction occurs. It is also possible to assign different range cuts and step size values for different geometry regions.

The range cuts in this work are used for the electromagnetic processes of electrons, positrons and gammas. For our simulation, the range cut inside the detector was set to 0.1 μm for all particles to increase the number of electron-ion pair and more closely replicate the detector response while a 1 μm was used for the detector shielding and collimator. In the target region, the range cut was set to 0.01 mm to increase prompt gamma production. The range cut for the remaining geometry was set to 1 mm. To reduce CPU usage, a maximum step size of 10 mm was used throughout the geometry, except inside the target where it was set to 0.5 mm which is smaller than the bin size of 1 mm.

2.1.2 Geant4 physics model

The Geant4 provides complete physics process models for electromagnetic and hadronic interactions. In this study, we constructed the recommended physics list for proton radiotherapy QGSP_BIC_EMY (Cirrone et al. (2011)) by means of a modular physics list approach that allows inserting all the pre-packaged pre-build physics lists. The QGSP model (Quark-Gluon-String-Precompound) consists of hadronic models collision between hadrons and nucleons. The low-energy electromagnetic package *standard_opt3* was used and includes the processes of ionization, bremsstrahlung, multiple scattering, Compton scattering, photoelectric effect, pair production and annihilation for electromagnetic interactions of leptons, gammas, hadrons and ions tracking without magnetic field. By default, the selected physics list provides the binary cascade model for inelastic nuclear reactions.

2.1.3 Geant4 binary cascade model

In the binary cascade model, an inelastic nuclear interaction is described by the two-particle binary inelastic collision between an incident proton and the nucleons inside the target nucleus. Further interactions between the remaining nucleons in the target nucleus and resulting secondaries are allowed to create an intra-nuclear cascade. To check the resulting secondaries, the Fermi exclusion principle is applied. If the momentum of a secondary particle falls below the Fermi level (momentum), the interaction is suppressed. Therefore the original primary particle is taken to the next interaction. On the other hand, if an interaction does occur, the secondaries are then treated like primary particles. The particle propagated into the nuclear field is calculated by solving the equation of motion numerically. The cascade is terminated if the secondaries do not reach the threshold energy required for the interaction. After each interaction, particle-hole states or excitons will be added to the target nucleus and at the end of cascade, the remaining residual nuclear system with its corresponding exciton state is then handled by the precompound and de-excitation models. The binary cascade model is valid for incident proton energies from 0 to 10 GeV.

2.1.4 Geant4 precompound model

The precompound model is an alternate low-energy inelastic nuclear reaction model for prompt gamma simulations (Polf et al. (2009b)). The initial precompound nucleus

is described by the atomic mass (A) and charge (Z) of residual nucleus, its four momentum vector (P_0), nuclear excitation energy (U) and the number of excitons (n), calculated by summing the particles (p) above the Fermi level and the vacancies or holes (h) under the Fermi level of the compound nucleus. Statistical equilibrium is characterized by an equilibrium number of excitons n_{eq}. Geant4 determines the appropriate transitions by looping through the possibilities until an equilibrium condition is reached for de-excitation based only on excitation energy, not number of excitons. Several nuclear transitions are possible for $\Delta n = \pm 2, 0$ and each is associated with their respective transition probability $w_{\Delta n}(n, U)$ which depends on the exciton number (n) and excitation energy (U). If there is particle emission (neutrons, protons, deutrons, tritium and helium nuclei) before equilibrium reached, the above steps are repeated with the new nuclear fragment. The particle emission is also associated with an emission probability $W_b(n, U, T_b)$, where T_b is the kinetic energy of the emitted nucleon or fragment. At statistical equilibrium, the simulation will be handled by the equilibrium model for emission of photons, nucleons and light fragments from the residual state (Jarlskog and Paganetti (2008)). The evaporation model is considered for the emission of nuclear fragments or gammas from the excited nucleus through one of the five different channels handled by G4ExcitationHandler: evaporation as the main de-excitation, fission for heavy nuclei, Fermi break-up for light ions, photon evaporation as competitive channel in evaporation and multifragmentation for very excited nuclei (Lara and Wellisch (2000)).

2.2 Assessment of prompt gamma emission from Geant4 physics models and cross-section data

The purpose of this work is to find a suitable inelastic nuclear reaction model for prompt gamma simulation using the available gamma production cross-section data. Currently available experimental inelastic cross-section data (measured primarily for astrophysical purposes) for proton-induced nuclear reaction on ^{16}O , ^{12}C and ^{14}N (with statistical and systematic error analysis) are found in Kiener et al. (1998), Dyer et al. (1981), Belhout et al. (2007), Narayanaswamy et al. (1981), Lang et al. (1987), Lesko et al. (1988) and Benhabiles-Mezhoud et al. (2011).

2.2.1 Geant4 physics models and cross-section data specific to prompt gamma emission

Geant4 provides several pre-built physics models for low-energy proton-nuclear inelastic interactions: the binary cascade (BIC), precompound (PRECO) and intra-nuclear cascade (INCLXX) models. The alternate Bertini cascade model was unsuitable as observed prompt gamma spectrum was contentious. Because of the code's flexibility, physics models can be modified to meet user requirements in order to fit their experimental data. Table 2.2 summarizes the first six essential elements found in the human body. Among them ^{12}C, ^{16}O and ^{14}N are the most abundant elements which emit discrete gamma-rays as a result of de-excitation of excited nuclei produced from inelastic nuclear reactions (Kiener et al. (1998), Lang et al. (1987), Benhabiles-Mezhoud et al. (2011) and Verburg et al. (2012)). Prompt gamma production from ^{14}N is of less interest for two reasons. First, atomic concentration of ^{14}N (1.3 %) in tissue is very low compared to other two elements ^{16}O (25.6 %) and ^{12}C (25.6 %). Secondly, the prompt gamma production cross section for ^{14}N in the interested energy range of 3 - 7 MeV (Verburg et al. (2012)) is under few ten mb (Benhabiles-Mezhoud et al. (2011)).

Since up to 90% of living human cells are composed by water, the overall performance of prompt gamma production is highly dependant on ^{16}O. Also water has been used as an alternative to tissue in other prompt gamma measurements (Verburg et al. (2013)). Therefore water (or ^{16}O) is considered as the reference material in our work. However, accurate production cross sections of discrete gamma-rays emitted from ^{16}O and ^{12}C elements are required to identify the best Geant4 physics model for simulation of reasonable prompt gamma spectrum. Unfortunately, in Geant4, there is no direct parametrization of gamma production cross section, only partial cross sections depending on the selected inelastic reaction model invoked by total non-elastic reaction cross-section data. There are two possible options for total non-elastic proton-nuclear cross-sections available: the default cross-section in the precompound and the binary cascade models is the Willish and Axen (1996) data set and the cross-section of Tripathi et al. (1999) which is an alternate option for light systems (Verburg et al. (2012)). So, these two Geant4 total non-elastic cross-section data for proton induced reactions on ^{16}O, ^{12}C and ^{14}N were then evaluated with respect to the available experimental and ENDF/B-VII data.

Once the total non-elastic cross-sections were evaluated, the discrete proton-induced gamma ray emissions from ^{16}O , ^{12}C and ^{14}N were simulated and the results compared

Table 2.2: *Summary of essential elements in the human body. (Source: Chang, Raymond (2010). Chemistry, Tenth Edition. McGraw-Hill. pp. 52.).*

Element	Mass (%)	Atom (%)
Oxygen	65	25.6
Carbon	18	9.5
Hydrogen	10	63
Nitrogen	3	1.3
Calcium	1.6	0.24
Phosphorus	1.2	0.24

to experimental cross-section data. The discrete prompt gamma emission from selected inelastic reaction physics models were considered independently in order to provide the best fit to the data similar to a method described in Verburg et al. (2012). The gamma production cross-sections were calculated from the energy spectra as described in the following sections.

2.2.2 Defining cross-section

Materials are composed of one or more type of element. To determine the number of proton-induced inelastic collisions, it is necessary to know the probability of a proton interacting with each nucleus within the material. This probability is described by the nuclear cross-section which depends on the type of element in the material and the energy of the incident proton. The cross-section for a particular interaction also depends upon the type of interaction involved. The probability of a reaction occurring between a proton and a nucleus is called the microscopic cross-section (σ) of the nucleus for that particular reaction. If a proton interacts with a certain volume of material the interaction probabilty depends not only on the microscopic cross-section of the individual nuclei but also on the number of nuclei within that volume. Therefore it is necessary to define another kind of cross section known as macroscopic cross section (Σ) which is related to microscopic cross-section as shown in the equation 2.1.

$$\Sigma = N\sigma \tag{2.1}$$

where N is the nuclear number density (number of nuclei per cm^3). The microscopic cross-section (σ) represents the effective target area of a nucleus for the proton for a particular interaction, expressed in units of area (cm^2 or barns). The macroscopic cross-section, on the other hand, represents the effective target area that contains all the nuclei in 1 cm^3 of the material. The unit is given as cm^{-1}. The total macroscopic cross-section of a composite material can be defined as the sum of all the individual macroscopic cross-sections.

$$\Sigma_T = N_1\sigma_1 + N_2\sigma_2 + N_3\sigma_3 + ... + N_n\sigma_n \tag{2.2}$$

where N_n is the nuclear number density of the n^{th} element and σ_n is the microscopic cross-section of the n^{th} element. A proton can interact with an atom in a material through an inelastic/non-elastic reaction (σ_R) or an elastic scatter reaction ($\sigma_{elastic}$), therefore the total microscopic cross-section (σ_T) is defined as the sum of all the nuclear reaction cross-sections.

$$\sigma_T = \sigma_R + \sigma_{elastic} \tag{2.3}$$

For the cross-section comparison simulations, in order to specifically measure the inelastic cross section values, the elastic reaction channel was disabled, therefore the total reaction cross-section per atom is equal to the total inelastic reaction cross-section per atom.

$$\sigma_R = \sigma_T \tag{2.4}$$

2.2.3 Calculation of macroscopic cross-section using mean free path

The average distance travelled by a proton before an interaction is called the mean free path (λ) for that interaction. The mean free path is the inverse of the macroscopic cross-section.

$$\lambda = \frac{1}{\Sigma_T} \tag{2.5}$$

The total cross-section per volume (macroscopic) can be calculated from the inverse

of the mean free path of an incident proton. If the material is composed of a single element, using equation 2.1 and 2.5, the cross-section per atom (microscopic) will be defined as

$$\sigma = \frac{1}{N\lambda} \tag{2.6}$$

and

$$\sigma = \frac{M}{\rho\lambda N_A} \tag{2.7}$$

where ρ is the density of the material, N_A is the Avogadro's number (6.022 x 10^{23} atoms/mole) and M is the atomic weight in grams. If the reaction takes place between a primary proton and a nucleus inelastically, the prompt gamma production cross-section (σ_γ) will be defined as

$$\sigma_\gamma = \frac{M}{\rho\lambda N_A} \times \frac{R_\gamma}{N} \tag{2.8}$$

where R_γ is the number of prompt gamma per N incident protons. For the cross-section comparison simulations, each run was carried out with thick targets wide enough for an inelastic interaction to occur for every event. An event was killed after the first inelastic reaction to avoid multiple interactions. 1×10^7 proton inelastic histories were generated for each incident proton energy. The rate of nuclear reactions corresponding to each gamma yield was calculated from the spectra created by the ROOT data analysis tool.

2.3 Monte Carlo model of the iThemba LABS passive-scatter proton therapy beam line

There are two different dose delivery methods available for clinical proton beam radiotherapy: passive-scatter beam and active-scanning beam. In the passive-scatter proton therapy treatment technique, an accelerated mono-energetic proton beam is directed into a treatment nozzle where a single- or double-beam scattering method is used to broaden the proton beam uniformly in the lateral direction by placing high-Z scattering plates into the beam path. The beam can also be spread out along the beam direction

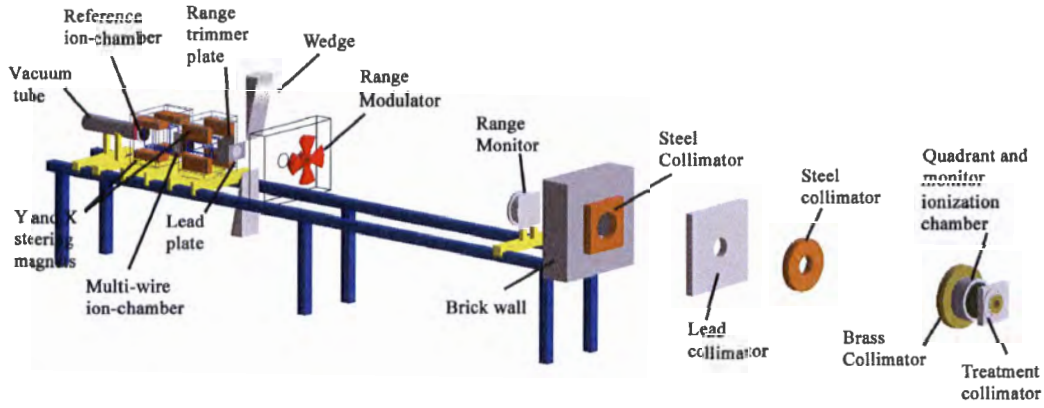

Figure 2.1: *Geant4 Monte Carlo model of the proton passive-scatter beam line at iThemba LABS.*

to form a spread-out Bragg peak (SOBP) with the use of a range modulator wheel. In addition, there are a set of collimators in place to spare the patient and electronics from excess scattered radiation by the beam-line elements. By contrast, in the active-scanning technique, the range modulator is replaced by two perpendicular magnets to steer the proton beam across the tumour volume in the X and Y directions. The mono-energetic high-intensity proton beam then paints the tumour with dose one layer at a time, changing the beam energy at each layer building up a SOBP. This allows treatment of each voxel within the layer. There are no beamline elements required to spread out the beam greatly reducing the amount of secondary radiation produced. There is also no need for the use of patient-specific collimators or compensators in order to conform the dose.

For the present work, the prompt gamma emission measurements were carried out with the passive-scatter proton beam-line facility at iThemba LABS (Laboratory for Accelerator Based Sciences) in Faure, South Africa. The entire beamline modelled in Monte Carlo is shown in Figure 2.1, including all elements that directly interact with the beam. The vacuum chamber is the first element in the treatment nozzle. The reference ionization chamber which was placed next to the vacuum tube acts as the first scatterer. The lead plate or graphite double-wedge degrader is the second scatterer. The lateral dose profile is produced by the range monitor which has a long cylindrical occluding rod and beam retarder plate. The X and Y steering magnets were included in our simulation as a part of the beam line geometry, but the corresponding magnetic fields were not included in the simulation because they remain static during any treatment or

Table 2.3: *Details of beamline elements and their position along the z-axis. The maximum uncertainty in the z distance is 3.0 mm (Kock (2007)).*

Element	Distance z (mm)	Position specification
Vacuum window	0	Downstream face
Reference ionization chamber	47	Center between two lead electrodes
Y-steering magnet	80	Upstream face of pole shoes
Multi-wire ionization chamber	356	Mid point between the two HV plates
X-steering magnet	446	Upstream face of pole shoes
Range trimmer plates	683	Upstream face of 1st plate
Lead plate	774	Upstream face
Double wedge energy degrader	895	Mid point between the two wedges
Range Monitor	3065	Downstream face
Brick wall collimator	3431	Upstream face
Steel collimator	3626	Upstream face
Lead collimator	4519	Upstream face
Steel collimator	5190	Upstream face
Brass collimator	6427	Upstream face
Quadrant and monitor -ionization chamber	6573	HV aluminium foil of monitor chambers
Treatment final collimator	6678	Downstream face of collimator holder
Isocenter	6978	—

measurement and thus, will not impact our validation. The main elements in the beam line and their positions are listed in Table 2.3. The positive z-axis is used to indicate the direction of proton beam. The x-y plane is perpendicular to the beam axis so that the x-axis is in the horizontal direction, while the y-axis is in the vertical direction. The upstream face of an element is the face closest to the vacuum window (i.e., facing the vacuum window), and the downstream face is furthest from the vacuum window. All the distances are measured from the downstream face of the Havar window which acts as the interface between the vacuum chamber and outside air (Kock (2007)). The chemical composition of each individual element and densities of each material in the beam line model are given in Appendix A. A detailed description of each element is given in the following sections.

2.3.1 Reference ionization chamber

The reference ionization chamber is a parallel plate chamber with two circular lead electrodes 60.0 mm in diameter and 0.234 ± 0.0046 mm thick. A 1.0 mm-thickness lexan isolating disc of 40.0 mm inner and 60.0 mm outer diameter is used to separate

the electrodes. A cylindrical Perspex casing, with a 90 mm outer diameter and a circular aperture of 40.0 mm in diameter, is used to pack the lead electrodes and the isolating spacer as seen in Figure 2.2. Both upstream and downstream faces of the casing are covered using two 25 mm-thick Kapton layers. The reference chamber is mounted on a Perspex disc, which is 3.5 mm thick, has an outer diameter of 118 mm and a hole with a diameter of 45 mm at its centre. The Monte Carlo model of the reference ionization chamber is shown in Figure 2.3.

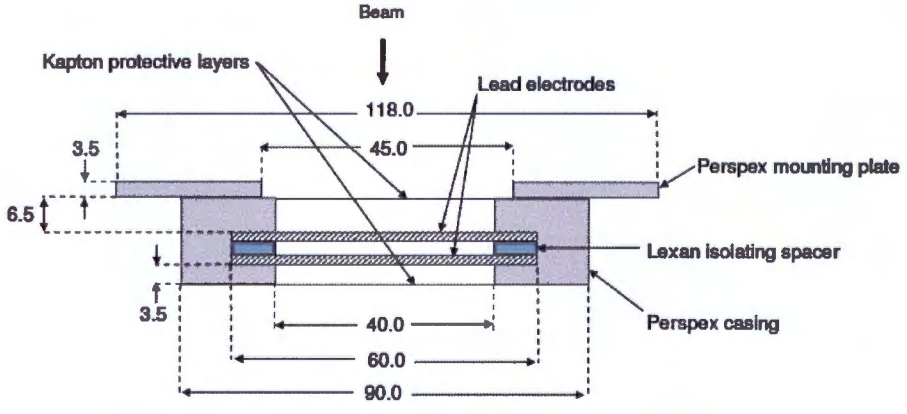

Figure 2.2: *Reference ionization chamber. (Source: Kock (2007)).*

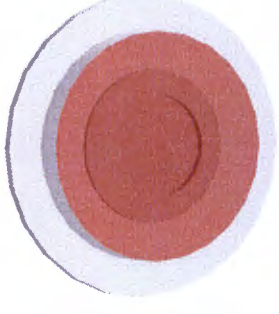

Figure 2.3: *Monte Carlo model of the reference ionization chamber.*

2.3.2 Steering magnets

There are two steering magnets in the beamline: the vertical steering magnet (Y-steering) and the horizontal steering magnet (X-steering). Figure 2.4 shows the lateral dimensions of the X-steering magnet. The steering magnet is 200 mm long (z-axis). The Y-steering magnet is identical to the X-steering magnet but is rotated about the z-axis. The proton beam passes through the centre gap of 159 mm width and 78 mm height (y-axis) between the pole shoes. The yokes, divider plates and poles shoes are all made of iron. The Monte Carlo model of the steering magnets is shown in Figure 2.5.

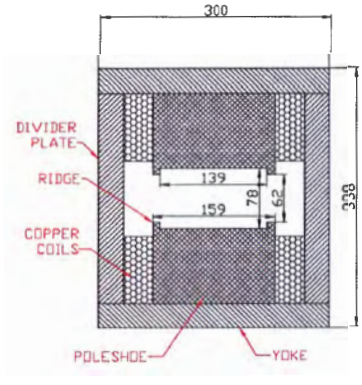

Figure 2.4: *The X-steering magnet (picture taken from Kock (2007)).*

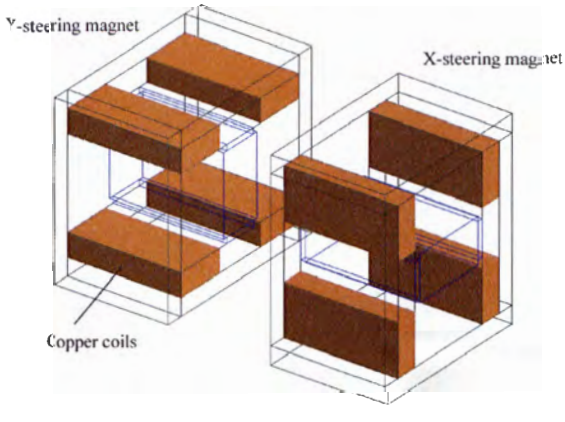

Figure 2.5: *Monte Carlo model of the steering magnets. All elements shown as wire frame except for copper coils.*

2.3.3 The multi-wire ionization chamber

A lateral view of the multi-wire ionization chamber is shown in Figures 2.6 and 2.7. The multi-wire ionization chamber is composed of 49 parallel 0.1 mm diameter tungsten wires used in both vertical and horizontal directions with a 2 mm spacing. There are two aluminium HV plates of 125 μm thickness placed 10.0 mm from the wire planes with 35.0 mm spacing between the plates. The 25 μm thick Kapton layers are used to protect the chamber and maintain a 10 mm distance from the HV plate.

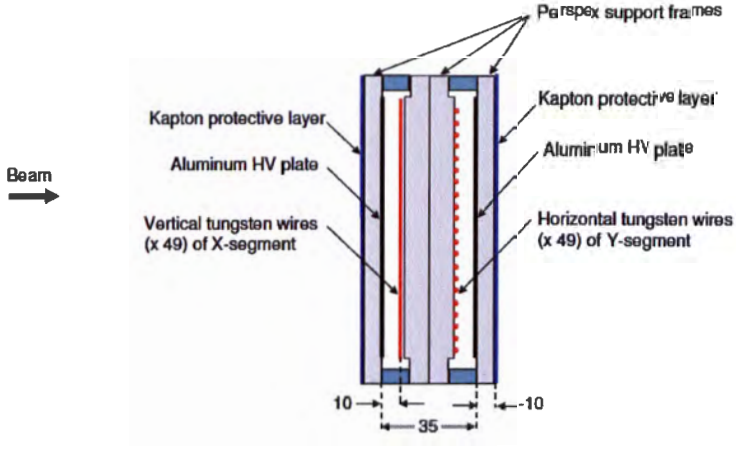

Figure 2.6: *The multi-wire ionization chamber. (Source: Kock (2007)).*

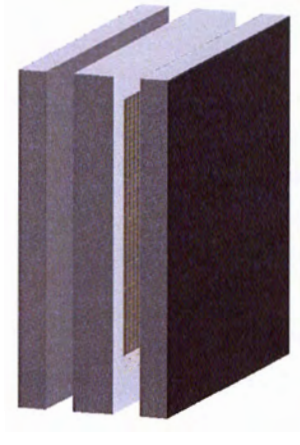

Figure 2.7: *The Monte Carlo model of the multi-wire ionization chamber.*

2.3.4 Range trimmer plates

There are seven range trimmer plates that can be used in the beam line to reduce the beam energy in order to maintain a R_{50} range of 240.0 ± 0.4 mm in water. The trimmer plates are made of thiolyte (paper-based phenolic resin compound). The density of the trimmer plates is 1.426 ± 0.0066 g/cm^3. Each trimmer plate is 0.622 ± 0.009 mm thick, 150 mm wide and 150 mm high. The water equivalence factor of the trimmer plate is 1.353 ± 0.0063.

2.3.5 Lead scattering plate for shoot-through beams

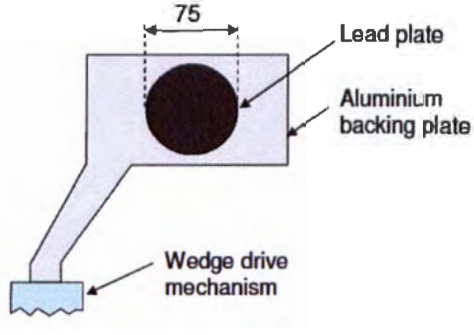

Figure 2.8: *Beam's eye view of the lead plate with aluminium backing plate for shoot-through beams. (Source: Kock (2007))*

A lead scattering plate is used to spread the proton beams laterally. As illustrated in Figure 2.8 a lead plate with a 75 mm diameter circular aperture is placed in the beam path when the two wedges are fully opened. When the wedges are used to degrade the proton beam to a lower energy (below 200 MeV), the lead plate is removed from the beam line. A driver mechanism is used to mount and remove the lead plate. The diameter of the lead plate centred on the beam axis is good enough to cover the beam and the thickness of the lead plate is 0.527 ± 0.007 mm.

2.3.6 Double-wedge energy degrader

The energy degrader system, consisting of two synthetic graphite wedges (density of 1.86 g/cm^3), is 400 mm long (along y-axis), 150 mm wide (along x-axis) and 90 mm

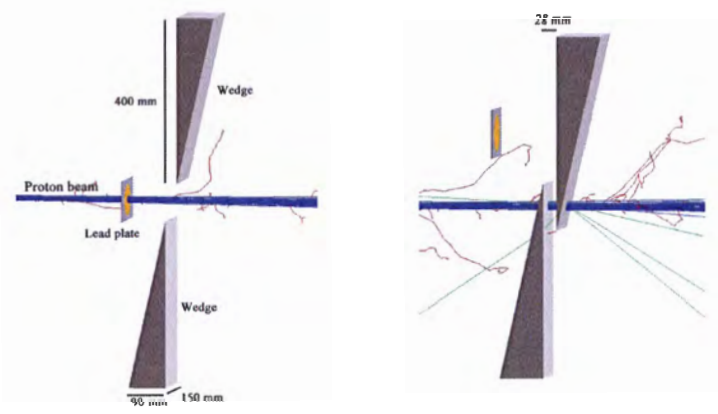

(a) (b)

Figure 2.9: *A Monte Carlo Geant4 model of the double-wedge energy degrader system (a) shoot through beam configuration with the lead plate; (b) SOBP configuration.*

thick at the base of the wedge (along the z-axis) (see Figure 2.9). The horizontal gap between the two wedges is 28 mm. The double wedges are mounted back to back on a driver mechanism that allows them to slide up and down parallel to each other in opposite directions, so that the upstream wedge moves upward, while the downstream wedge moves downwards. Therefore the thickness of the double-wedge energy degrader at the beam axis varies in order to produce a different proton R_{50} range at the isocentre (the reference point marking the center of the treatment beam). The maximum range (R_{50}), measured at the 50% distal edge of the Bragg peak, that can be produced using the wedges is 220 mm. The R_{50} range for the open position of the wedges (shooting through the lead plate) is 240 mm.

2.3.7 Range monitor

The range monitor controls the position of the distal falloff of the spread-out Bragg Peak (SOBP) dose distributions delivered by the passive-scatter proton treatment nozzle at iThemba LABS. The newly designed range monitor detector replaces the existing Multi-layer Faraday cup (MLFC), the occluding rings and the scattering plate used to deliver uniform lateral doses to the tumour for treatment. For ranges less than 24 cm, the double-wedge energy degrader is used to reduce the range of the proton beam. The uncertainty in the range is within 0.3 mm of the prescribed range. The electric signal

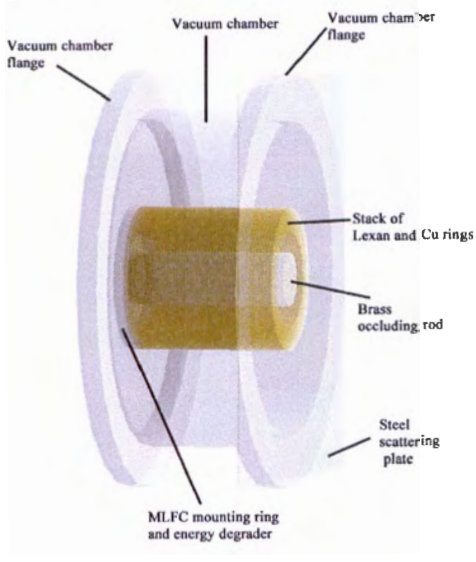

Figure 2.10: *Geant4 Monte Carlo model of range monitor (proton beam comes from left).*

from the range monitor is fed back to the energy degrader controller, where the overlap of the two graphite wedges (i.e. the thickness of graphite) of the energy degrader is adjusted to get the desired range.

The Monte Carlo model of the range monitor is shown in Figure 2.10. The range monitor is a vacuum chamber that consists of a multi-layer Faraday cup (MLFC), a brass central beam stopper and a steel scattering plate. The MLFC is a stack of 46 alternating 1 mm thick Lexan and 45 Cu discs of 0.7 mm thick. The stack starts and ends with a Lexan ring. All Lexan and Cu plates have a 72.22 mm outer radius and a 48.36 mm inner radius. The occluding rod is 81.85 mm long with a 26.88 mm outer diameter and has a 4.35 mm diameter deep recess in one end to fit onto a 4.35 mm diameter mounting platform. A 0.65 mm thick steel disk with outer diameter of 210 mm is used to mount the MLFC and occluding rod. The mounting plate consists of a 4.35 mm-thick steel raised MLFC mounting ring (acting as an energy degrader) that has a 72.22 mm outer and a 48.36 mm inner radius and a 4.35 mm steel raised occluding rod mounting platform with 20 mm outer radius. Three 81.85 mm long and 5 mm diameter Vesconite location rods are on the MLFC mounting ring spaced at 120^o interval. All Lexan and Cu plates are mounted using these Vesconite location rods as illustrated in Figure 2.11. The MLFC and occluding rod are placed into a 10 mm-thick vacuum chamber. The inner and outer radius of the vacuum chamber are 160 mm and 170 mm

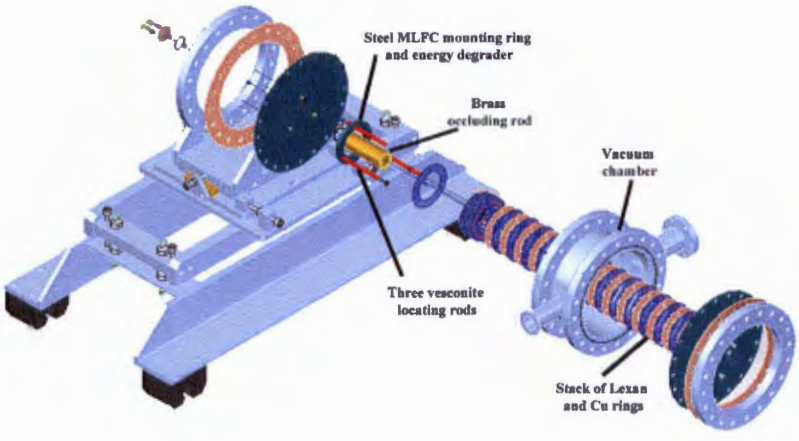

Figure 2.11: *Range monitor. (Source: iThemba LABS)*

respectively. The vacuum chamber has a 10 mm-thick flange with outer radius of 210 mm in both ends. At the end a 0.65 mm thick and 200 mm square steel scattering plate is fixed. The MLFC mounting plate and the steel scattering plate are fixed with vacuum chamber flange using twelve M8 screws each separated by 30^o around the 190 mm diameter. Two 3.53 mm thick Viton O-ring of diameter 170 mm are used to tie the MLFC mounting plate and the steel scattering plate with the vacuum chamber flange.

2.3.8 Shielding collimators

In the beam line, five different type of shielding collimators are used to protect the patient and electronic instruments from scattered radiation. The first shielding collimator is a big brick concrete wall which has a square aperture of 195 x 195 mm^2. The wall thickness is 195 mm. The brick wall isolates the treatment room from the rest of the main beam line elements. The second shielding collimator is made of steel having a circular aperture of 170 mm. The lateral dimensions is 300 x 300 mm^2 and the thickness of the steel block is 51.4 mm. The third collimator in the beam line is a rectangular 500 mm wide, 497 mm high and 48.8 mm thick lead block. The circular aperture in the block has a diameter of 120 mm. The fourth collimator is a circular iron collimator of 380 mm outer diameter and 50 mm thickness with an aperture diameter of 120 mm. Finally, there is a 50.5 mm thick brass shielding collimator with an outer diameter of 380 mm and circular aperture of 100 mm diameter. All five collimators are included in the Monte Carlo model of the iThemba LABS proton therapy beamline.

2.3.9 Quadrant and monitor ionization chambers

The quadrant chamber is used to measure beam position and symmetry while the monitor ionization chamber (a dual transmission chamber) is used to measure the dose delivered. The quadrant chamber has the signal plate etched into quarters, each of which feeds an electrometer. In the ring and quadrant chamber, two circular Kapton protective foils of 25.0 μm thickness are separated by three circular gold-plated Kapton electrodes of 6.67 μm thickness. The five foils with 240 mm diameter are evenly separated over a distance of 47.0 mm. In the dual transmission chamber, two aluminised mylar foils of 5.0 μm thickness and 220 mm diameter are kept together with 5.0 mm separation within a cylindrical Perspex casing having circular aperture of 200 mm diameter in both its faces. A 125-μm thick aluminium HV foil is centred between the foils.

Finally, both chambers are kept together in a cylindrical aluminium housing with Perspex end-caps having a circular aperture of 220 mm diameter and the downstream end-cap is closed by a 0.188 mm thick Mylar film. The transmission chamber is placed so that the downstream aluminised Mylar foil is 10 mm from the protective film and the upstream aluminised Mylar foil is 33.0 mm from the downstream Kapton protective foil of the ring and quadrant chamber as shown in Figure 2.12. The Monte Carlo model is shown in Figure 2.13.

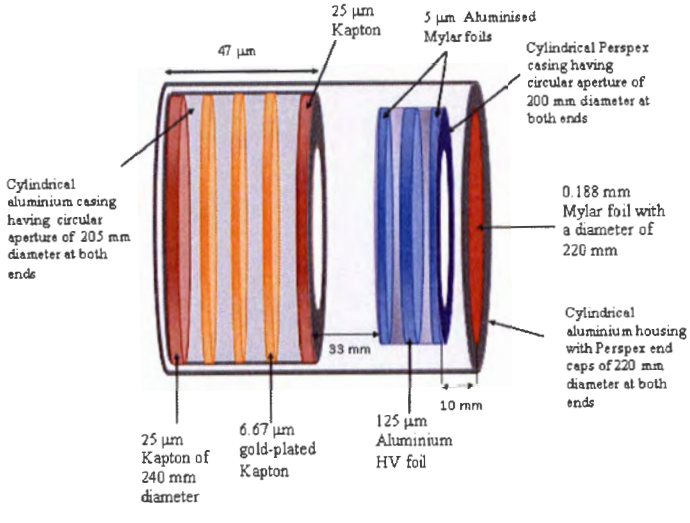

Figure 2.12: *The quadrant and monitor ionization chambers (proton beam comes from left).*

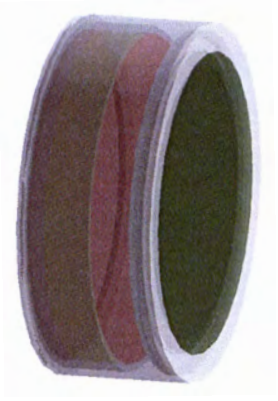

Figure 2.13: *The Monte Carlo model of the quadrant and monitor ionization chambers (proton beam comes from left).*

2.3.10 Treatment collimator assembly

Figure 2.14 illustrates the upstream and downstream faces of the treatment collimator assembly where a short cylindrical collimator holder is fixed coaxially with the circular aperture of the base plate and attached to a pulley on the upstream face of the base plate. The pulley allows the holder to rotate on the stationary base plate. Brass collimators are available with different aperture shapes (circular, elliptical or rectangle) to be used to mount the Cerrobend patient collimator. The maximum radius of the circular field is 5 cm. Figure 2.15 shows the Monte Carlo model of the final collimator.

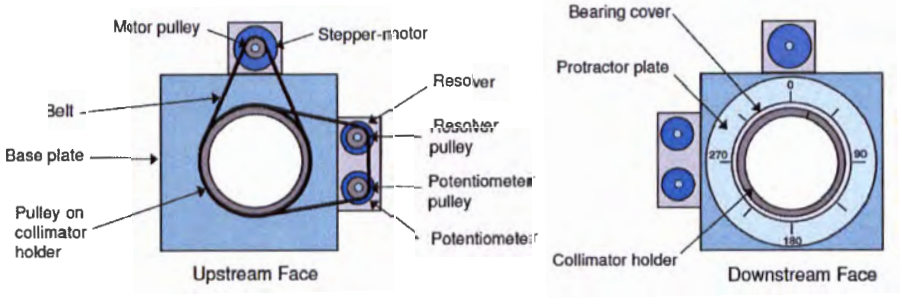

Figure 2.14: *The patient treatment collimator. (Source: iThemba LABS)*

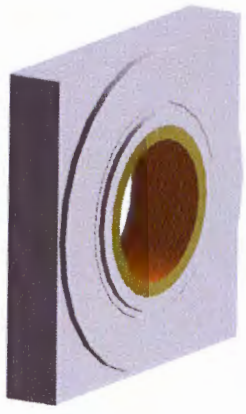

Figure 2.15: *Monte Carlo model of the final treatment collimator.*

2.4 Validation of the Monte Carlo passive-scatter proton beam line model

In order to validate the Geant4 model of the proton beam line, the simulated results should replicate the dose profiles used for the treatment of patients, specifically the depth dose and lateral dose profiles. The iThemba LABS proton therapy beam line is calibrated before every treatment by measuring the range of the beam at the 50% distal fall-off position in water ($R_{50\%}$). Range trimmer plates are added or removed from the beam to adjust for variations in the beam until the 50% distal position is at 24 cm. For the Monte Carlo model, instead of working backwards from a 24 cm range, we must start with a detailed description of the incoming beam of protons.

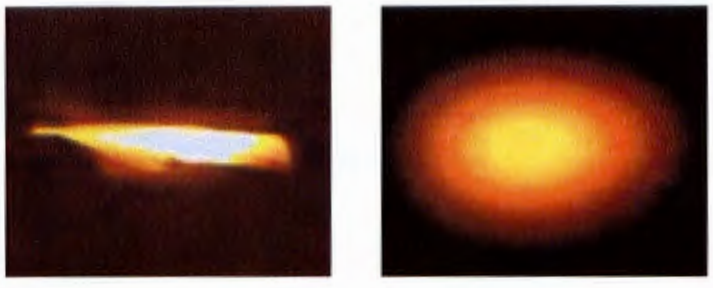

(a) (b)

Figure 2.16: *Actual shape of the beam exiting the vacuum window (a) before and (b) after the first lead scatterer using radiochromic films.*

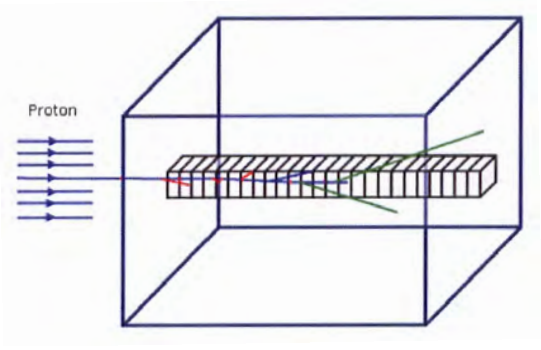

Figure 2.17: *Active volume of scoring geometry around the central axis.*

The actual cross-sectional view of the proton beam exiting the vacuum window before and after the lead scatterer is shown in Figure 2.16. The actual beam shape shown in Figure 2.16(a) is difficult to describe, so the beam spot in the model was depicted as a two-dimensional beam profile like the one shown in Figure 2.16(b). It is assumed that the shape of the beam is an ellipse with dimension of 0.721 cm major radius and 0.586 cm minor radius (Figure 2.16(b)). Since the proton beam energy characteristics (mean energy and energy spread) can not be measured with sufficient accuracy, most Monte Carlo simulations have to be adjusted to fit the experimental range data, which can be measured very accurately (also see Section 4.2.2). The expected proton energy exiting the vacuum window into the treatment room is 199.78 MeV, but this value was adjusted to 201.36 MeV in order for our simulations to line up with the measured[1] depth and lateral dose profiles. The energy spread of the proton beam was set to be 2.0 MeV.

Measured depth dose and lateral dose data measured in a water tank using an ionization chamber were used to validate the beam line model. The simulation measurements were performed in a voxelized region created within the simulated water tank using the ROGeometry classes as seen in the Figure 2.17. The volume of each cubic voxel is 0.01 cm^3, which is equal to the effective volume of the ionization chamber typically used at iThemba LABS for the beam calibration. The thickness of each slice is 1 mm and good enough to produce the same spatial resolution. The energy deposited by the primary protons and any secondaries in each voxel was collected at the end of each run. In our

[1]measured with wedges open and lead shooting plates in place

beam line model, the particle step size was set to 0.01 mm inside the water phantom and the remaining regions. The step limit of 0.01 mm is smaller than thickness of the slice and was good enough to ensure adequate energy deposition within each detector slice. The range cut was set to 0.01 mm, which is translated into an equivalent minimum energy threshold for each type of simulated particles.

2.4.1 Validation of the range monitor

The charge created in each copper plate of the multi-layer Faraday cup (MLFC) of the range monitor is proportional to the number of protons stopped in that plate. Furthermore the charge deposited in each copper plate was calculated using a method described in Gottschalk et al. (1999), Paganetti and Gottschalk (2003) and Rinaldi et al. (2011).

In a typical event, when a primary incident proton is stopped by a copper plate either by a electromagnetic interaction (EM) at the end of range or a inelastic nuclear reaction before the proton range, the total charge deposited on that copper plate is equal to +1 proton charge. At each inelastic nuclear interaction, the charge of the recoil ion is calculated by subtracting the charge of the final state from the charge of the initial state (+1 proton charge). The appropriate amount of charge from the recoil ion is immediately added at the position where the nuclear reaction occurred. The charge of any secondary particle produced is also added at the position where it stops. The procedure is repeated until there are no further nuclear reactions. If a charged particle entered into the copper plate from the Lexan plate or outside, the appropriate charge is added immediately and then removed if it leaves the plate. The same approach is followed to score the secondary electrons and hole charges deposited during the hadron ionization process, +1e to score the charge of a hole where it is created and -1e to score the charge of a secondary electron where it comes to rest.

2.5 Generation of IAEA phase space file

In the present work, the IAEA phase-space (phsp) format was used to generate phase-space files in Geant4. All the details described in this section refer to Cortés-Giraldo et al. (2009) and Cortés-Giraldo et al. (2012). The IAEA phsp format is implemented by a set of read/write routines composed by IAEA classes (.hh and .cc) of iaea_config,

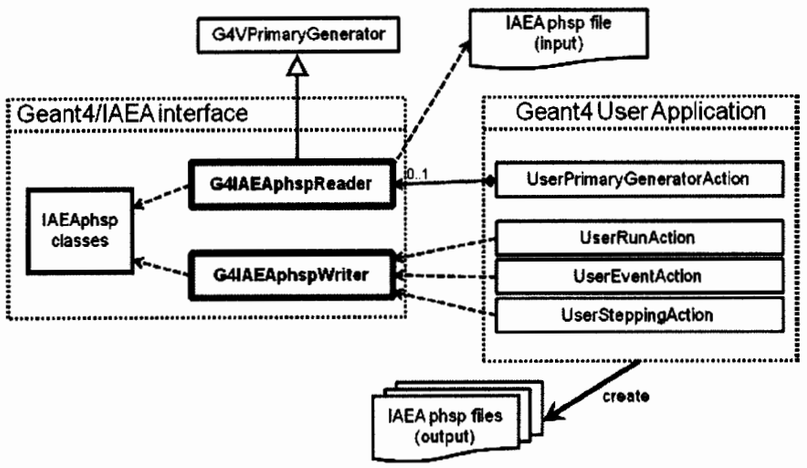

Figure 2.18: *The scheme of the IAEA phase-space format taken from Cortés-Giraldo et al. (2012).*

iaea_header, iaea_phsp, iaea_record and utilities. The IAEA phase-space format can be described as shown in Figure 2.18. The G4IAEAphspWriter class is used to create phase-space files and record the information including energy, position and momentum of particles crossing the designated phsp plane. The phsp plane is defined by its z coordinate. G4IAEAphspReader class is derived from the G4VPrimaryGenerator class of the GEANT4 toolkit to retrieve the stored source particle information. It is used in the UserPrimaryGeneratorAction class of the GEANT4 to generate particles using either the G4ParticleGun or G4GeneralParticleSource classes. An ASCII file is generated along with the IAEA phsp data file and gives a statistical summary of the generated phase-space data.

For the passive-scatter beam line simulations, phase-space files were used to save computation time by splitting up the simulations into two phases. In phase one, all the secondary and primary particles were started at the vacuum window and stopped at the position just before the final collimator (56 cm from the isocenter) and the detailed information of the primary and secondary particles were recorded in an IAEA phase-space format data file. In the second phase, the phase-space file was then used as the event generator in the primary generator action class in the subsequent simulation, allowing for changes to be made to the target and detector set-ups in the simulation without having to re-run the proton all the way through the beam line. The generated phase-space files were 100 gigabytes in size containing 10^{10} primary proton histories.

2.6 Determination of detector response functions (DRFs) for NaI and $LaBr_3$ detectors

A detector response function is essential for generating a realistic detector spectral response within a Monte Carlo simulation (Gardner and Sood (2004)). The ideal mono-energetic gamma ray spectrum is a sharp line at the energy of the incident gamma (E_o) as shown in Figure 2.19, but due to statistical fluctuations in the number of electron-ion pairs produced by the photo-electron and Doppler broadening during the proton-nuclei collisions, the actual gamma ray spectrum has a Gaussian shape (Knoll (2000)).

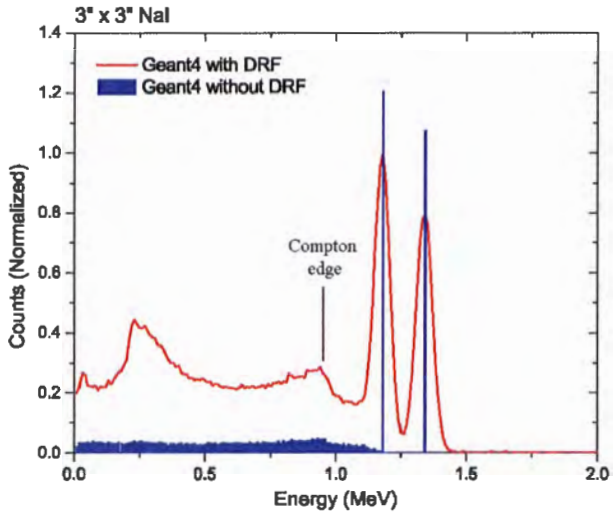

Figure 2.19: *Comparison of simulated ^{60}Co spectra using the 3 x 3 inch NaI detector with (red) and without (blue) the DRFs.*

The comparison of the simulated energy spectrum (with and without detector response) from a ^{60}Co point source for a 3 x 3 inch NaI detector is shown in Figure 2.19. When a gamma-ray enters the detector, it deposits part or all of its energy via electrons through different interactions such as photoelectric effect and Compton scatter. These electrons then transfer their kinetic energy through a series of collisions with other atomic electrons in the detector medium. A photoelectric interaction transfers all of the incident photon's energy to a photoelectron while a Compton scatter transfers only part of the incident photon energy to an electron. This partial energy deposit will not equate to the original incident photon energy, but multiple Compton interactions

can produce a total energy deposition closer to the full peak (photo-peak) energy. The detector pulses generated by the Compton electrons are therefore spread out at energies below the photo-peak energy and form the Compton continuum. The maximum energy deposition can occur when the photon scattering angle is 180^o (head-on collision) and produces the Compton edge (see Figure 2.19).

Detector resolution is the ability of a detector to resolve two peaks that are close to each other. Each detector has a unique response, thus producing slightly different energy resolution values. The parameter FWHM (full width of the photo peak at half its maximum) measures a detector's resolution. A high resolution detector has a small FWHM. If the shape of a photo peak has a standard Gaussian shape, the FWHM is given by

$$FWHM = \sigma\sqrt{8ln2} \tag{2.9}$$

$$g(\varepsilon) = \frac{A}{\sigma\sqrt{2\pi}} exp\left(-\frac{(\varepsilon - E)^2}{2\sigma^2}\right) \tag{2.10}$$

where $g(\varepsilon)$ is the Gaussian function with its centre at the incident gamma energy E, ε is the broadened energy, A is a normalization constant and σ is the width parameter of the Gaussian (standard deviation) (Wang et al. (2012)). Using a MCNP Monte Carlo simulation, equation 2.11 was used to determine a gaussian function for the detector response (Amgarou et al. (2009)).

$$\sigma = \frac{a + \sqrt{b(E + cE^2)}}{\sqrt{8ln2}} \tag{2.11}$$

where a, b, and c are user-defined parameters. Equation 2.11 shows that the standard deviation of the Gaussian shape thus depends on the incident gamma energy E. This relationship can be simplified to equation 2.12 and was reported as a good choice to determine the detector response function because of its simplicity (Wang et al. (2012)).

$$\sigma = xE^y \tag{2.12}$$

also written as

$$ln(\sigma) = yln(E) + lnx \tag{2.13}$$

The parameters x and y are determined by measuring the energy resolution of a specific detector.

The 3" x 3" and 2" x 2" NaI detectors used in this work were developed by Canberra and the 2" x 2" $LaBr_3$ detectors developed by Saint-Gobain (Saint-Gobain Crystals and Detectors, Nemours, France). $LaBr_3$ detector also includes its own photomultiplier tube and a preamplifier which was connected to a PC with a pocket multi-channel analyser (Amptek Pocket MCA-8000A). An external preamplifier was used for the NaI detectors. Six standard gamma emitting sources, ^{133}Ba, ^{22}Na, ^{137}Cs, ^{54}Mn, ^{60}Co and $^{241}AmBe$ with an energy range from 0.356 to 4.438 MeV were used for the detector resolution calibration. The Geant4 model of the $^{241}AmBe$ source is described in the following section. The detector response was then validated against the measured energy spectra for each of the different radioactive sources.

2.7 Geant4 model of ^{241}Am-Be neutron source

An isotopic ^{241}Am-Be neutron source was used to validate the NaI and $LaBr_3$ detectors. ^{241}Am produces neutrons via the ^{9}Be(α,n)^{12}C reaction. Sixty per cent of these neutron emissions are in coincidence with a 4.438 MeV gamma ray from the first excited state of ^{12}C (Vitorelli et al. (2005)). The ^{241}AmBe source was modelled in Geant4 according to the manufacturer's specifications as seen in Figure 2.20(a). The neutron energy spectrum shown in Figure 2.20(b) was generated using the Geant4 general particle source (GPS) package (via macro commands) to emit neutrons isotropically from the active volume of the source. A complete list of the macro commands used for ^{241}AmBe simulation is given in Appendix B. In addition to the neutron spectrum, a proportional number of 4.438 MeV γ-rays were added to the ^{241}AmBe source so that the ratio of 4.438 MeV γ-rays to neutrons was R = 0.575 $\pm$ 4.8% as reported in Liu et al. (2007).

Figure 2.21 shows the Geant4 models of the 3 x 3 NaI and 2 x 2 $LaBr_3$ detectors with the ^{241}AmBe source. Detector materials and dimensions were taken from manufacturer specifications. In the simulations, all the possible electromagnetic interactions for photons, electrons and positrons (Compton scattering, photo electric absorption, pair production followed by the positron annihilation, bremsstrahlung and radioactive loss of the secondary electrons) were considered. Calculation of the total energy deposited within the NaI and $LaBr_3$ crystals (the energy deposited in each step by the incident gammas is passed to secondary electrons and positrons which go through

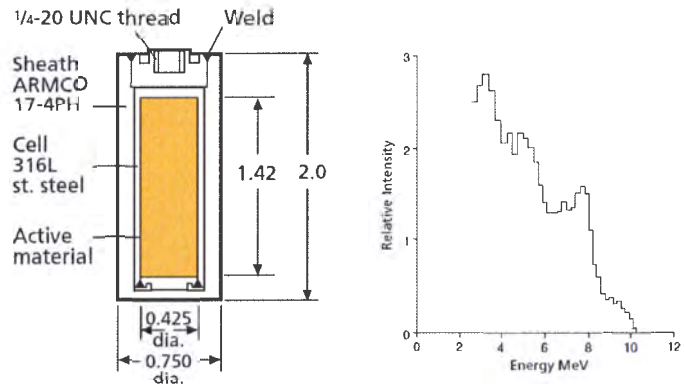

(a) (b)

Figure 2.20: *(a) ^{241}Am-Be source specification and (b) its neutron spectrum.*

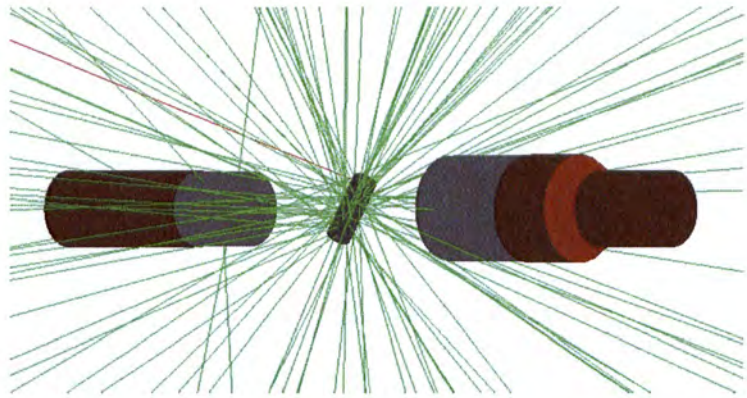

Figure 2.21: *GEANT4 Monte Carlo simulation of detectors with gamma rays from ^{241}Am-Be neutron source.*

multiple Coulomb interactions with surrounding atoms) was performed. The detector response function was then applied to generate the actual detector response at the end of each event. In Geant4, the secondary particle threshold cut value determines the secondary electron production. A low threshold (1 μm) was used in order to produce more electron ion pairs within the detectors.

2.8 Simulations of detected prompt gamma production from proton beam line

Geant4 simulations for the production of prompt gamma spectra from a water phantom were carried out with both active-scanning and passive-scatter proton beams of 200 MeV. The simulation geometry set-up for the active-scanning proton beam is shown in Figure 2.22(a). The target is a cylindrical water phantom of radius 10 cm and length 40 cm. A cylindrical $LaBr_3$ (2" x 2") detector (surrounded by both 18 mm thick BGO ($Bi_4Ge_3O_{12}$) active shielding and 10 cm thick lead) was modelled perpendicular to the beam axis with a 40 cm distance between the detector front face and the beam axis. A 15 cm thick lead collimator having a 5 cm x 5 cm square hole was used to collimate the prompt gammas between the target and the detector. The purpose of the BGO active shielding was to reduce the continuous Compton background caused by incomplete Compton-scattered gammas depositing energy in the $LaBr_3$ crystal. The BGO also reduces the number of neutron-induced gamma-rays produced in the lead detector shielding. Uncollimated gamma rays scattering from objects surrounding the detector were also attenuated by the lead shielding. A time-of-flight (TOF) approach was introduced in the simulation in order to reduce secondary neutrons hitting the detector from the target and scattered background gamma rays, a significant problem in passive-scatter beam radiotherapy. The simulation set-up for the passive-scatter beam line is shown in Figure 2.22(b), where the detector set-up is identical to the active-scanning beam set-up. The time of flight for the prompt gamma rays is shorter than the neutrons and greater than the scattered secondary gamma rays that are generated at the passive-scatter beam line elements. Therefore an appropriate TOF window can filter out the late-arriving neutrons as well as early-arriving background gamma rays.

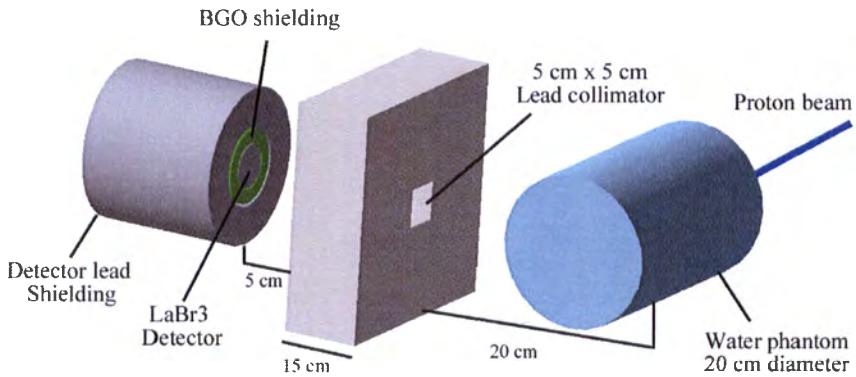

(a)

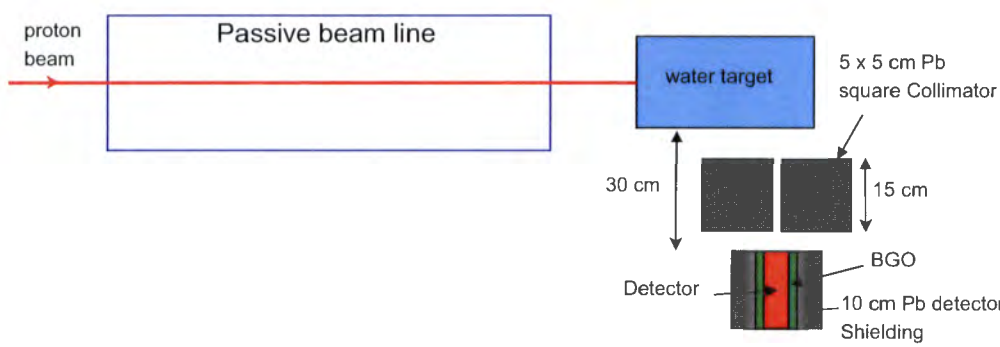

(b)

Figure 2.22: *Simulation geometry setup with (a) active-scanning proton beam and (b) passive-scatter proton beam.*

Chapter 3

Measurement of prompt gamma production from a passive-scatter proton therapy beam line

This chapter reports on the prompt gamma measurements carried out with the passive-scatter proton therapy facility at iThemba LABS in Somerset West, South Africa. Two set of experiments were conducted to measure the prompt-gamma production spectra: first, an experiment with the target at isocentre using both lead and neutron shielding; and second, an experiment with the target at 170 cm from the isocentre to minimize the secondary background radiation emitted from the final patient beam collimator. For the second set of measurements, the neutron shielding was removed and a lead collimator was used to collimate the prompt-gamma rays.

3.1 iThemba LABS

iThemba LABS (Laboratory for Accelerator-Based Sciences) at Somerset West in South Africa is a group of multi-disciplinary accelerator-based science labs part of the National Research Foundation (NRF), South Africa, and provides facilities for modern research using particle beams, particle radiotherapy for the treatment of cancers and the production of radioisotopes for nuclear medicine and research. The research facilities at iThemba LABS are used by scientists and students working in the physical, medical and biological sciences from institutions throughout the country and overseas. Protons are accelerated to a maximum energy of 200 MeV by a variable-energy Separated-Sector Cyclotron (SSC) and routed to different labs as shown in Figure 3.1. The radiotherapy treatment section consists of three beam transport lines: TC (Center Therapy) feeds 66 MeV protons to the neutron treatment unit where a thick beryllium target (p(66)/Be) is used to produced neutrons, TR (Right hand Therapy) and TL (Left hand Therapy) are proton therapy vaults. The TR line is used to transport 200 MeV protons to the passive-scatter beam nozzle which was used for the prompt gamma measurements discussed in this work. The TL line was allocated to build an active-scanning proton beam radiotherapy facility. A switching magnet is used to change the path of the proton beam from the SSC to any of the treatment vaults.

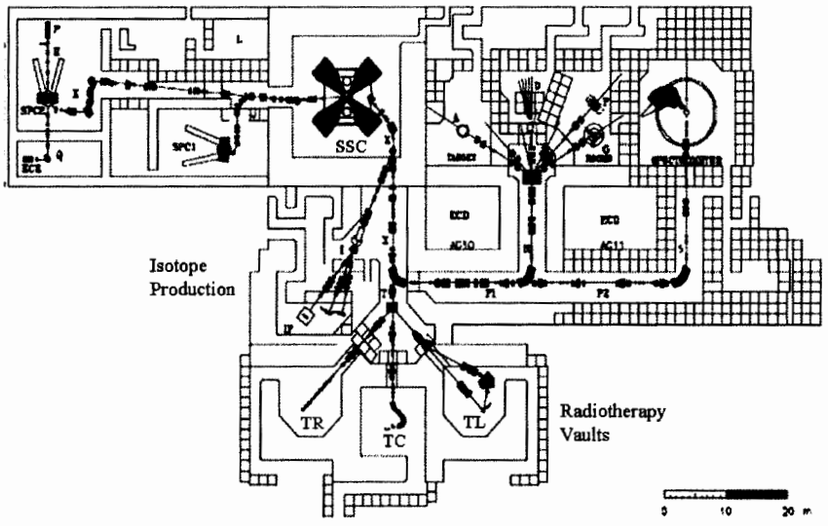

Figure 3.1: *Layout of the existing beam transport structure at iThemba Labs.*

3.1.1 The iThemba LABS proton therapy beam

The clinical passive-scatter proton facility at iThemba LABS relies on accelerated protons from the cyclotron. The cyclotron generates protons to energies up to 200 MeV at a radio frequency (RF) of 26 MHz with an RF period of 38.5 ns; the protons are transported along the beam line to the proton vault, where they are slowed down as they pass through the beam line elements (More details about the passive-scatter beam line can be found in Section 2.3). The measured proton beam energy at the isocentre (about 191 MeV) corresponds to a proton range of 24 cm calculated at the 50% distal fall-off position of the Bragg peak and has an entrance dose of 28 $\pm$ 1% (dose at the entrance point or phantom surface as shown in Figure 1.3). Full width at half maximum (FWHM) of the Bragg peak is 23 $\pm$ 1 mm.

3.2 Prompt gamma measurements with target at isocentre

The first set of prompt gamma measurements were carried out using the iThemba LABS proton beam line on 27^{th} June 2013 with the target positioned at the treatment isocentre as shown in Figure 3.2. The prompt gamma production from two different target materials (water and carbon) was investigated. The detector was a cylindrical-type $LaBr_3$ (2" x 2") scintillator consisting of its own photomultiplier tube and preamplifier, which was connected to a PC via a pocket multi-channel analyzer (Amptek Pocket MCA-8000A). The energy scale of the multi-channel analyzer was calibrated using

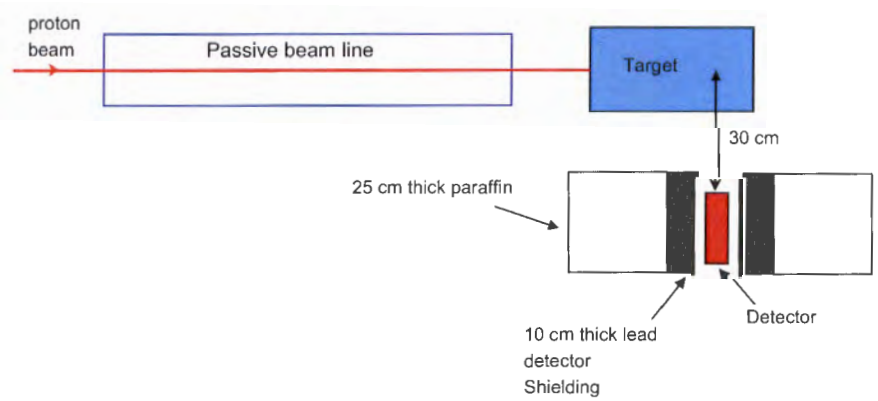

Figure 3.2: *Schematic diagram of the experimental setup.*

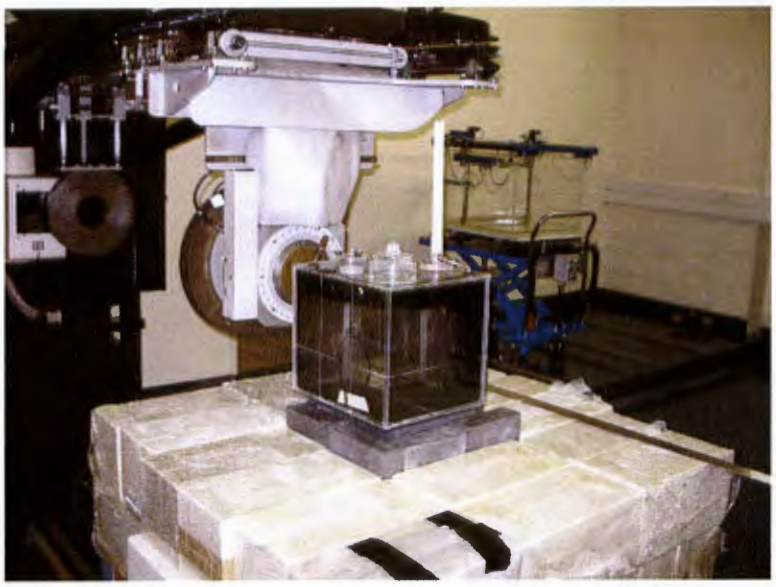

(a)

(b)

Figure 3.3: *(a) Experimental set-up. (b) View of detector surrounded by the lead and paraffin shielding.*

Table 3.1: *Summary of prompt gamma measurements with the target at the isocentre. (*Detector positions measured from the front surface of the phantom.)*

Date	Target	Proton Beam Range (cm)	Beam Current (c/s)	Acquisition Time (s)	Measurement Depth* (cm)
27^{th} June 2013	No (Background)	24	100	600	24 cm
	Water	24	100	600	24 cm
	Graphite	24	150	600	14 cm
	No (Background)	16	100	600	16 cm
	Water	16	100	600	16 cm

^{137}Cs, ^{60}Co and $^{241}AmBe$ standard gamma-emitting sources. The detector was surrounded by 10 cm of lead to attenuate the scattered gamma-rays entering the detector (the probability of a 6 MeV prompt gamma passing through 10 cm of lead without interacting is 1% (Smeets et al. (2012))). A 25-cm thick layer of paraffin wax was placed around the lead shielding (see Figure 3.3) to moderate the high-energy neutrons created in the passive-scatter beam line elements. The size of the proton beam at isocentre is determined by the final collimator, which was a 5-cm radius circular opening for these measurements. The detector system was arranged to be perpendicular to the beam axis directly beneath the target with a 30-cm distance between the detector front face and beam axis. Measurements were made of the prompt gamma spectra emitted from a water phantom of dimension 25 x 25 x 30 cm^3 and a graphite block with dimensions of 4.8 x 6.5 x 20 cm^3. The dimensions of each target were chosen to ensure that the protons were stopped within the target, thus producing the desired Bragg peak. The target was then positioned so that the location of the Bragg peak was lined up with the central axis of the detector. A data acquisition time of 600 seconds was used with typical count rates of 100-200 cps (for more details see Table 3.1). For each irradiation, a corresponding background acquisition was taken with the phantom removed from the proton path, thus eliminating the prompt gammas from the spectra. These backgrounds were subtracted from the measured spectra in order to highlight the desired prompt gamma peaks without the over-powering background noise from the beam line elements and detector shielding. The contribution of the neutron and scattered radiation coming directly from the target was not subtracted from the spectrum.

3.3 Prompt gamma measurements with target 170 cm from isocentre

In an effort of reduce the high level of radiation produced by the final collimator of the beam line, a second set of measurements were conducted on 24^{th} May 2014 with the following targets (water, graphite, Perspex and liquid nitrogen). For these measurements, the target was positioned 170 cm downstream from isocentre and the final collimator of the beam line was moved 150 cm upstream from its original position, thus increasing the distance between the collimator and the target to 320 cm. The detector set-up is shown in Figure 3.4 and is identical to the one used in the first set of measurements except for three additional details: the wax shielding was removed from around the detector, an extra 5 cm thick layer of lead was added along the beam direction and a 10 cm thick lead collimator was mounted in front of the detector. The wax shielding was removed because of its immense size and was considered redundant with the additional of the time-of-flight electronics. The lead was added in order to reduce background radiation from the beam line and from the target. The collimator in front of the detectors had a 5 cm x 10 cm rectangular opening. The modified detector system is shown in Figure 3.5. Two additional targets (Perspex and liquid nitrogen) were included with the water and graphite phantoms from the first set of measurements. The Prespex target had dimensions of 19 x 20 x 27 cm^3 and the liquid Nitrogen target was contained in a Styrofoam box with 4-cm thick walls and inner dimensions of 10 x 10 x 40 cm^3. Each spectra has an acquisition time of 1800 seconds with an approximate beam current of 0.5 nA. A list of the measurements can be found in Table 3.2. As with the previous set of measurements, for every measurement, a background spectra was taken with the target removed from the beam path.

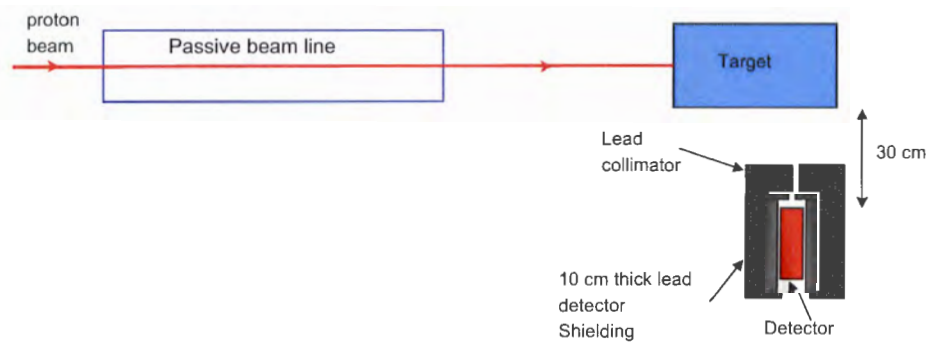

Figure 3.4: *Schematic diagram of the experiment set-up.*

Figure 3.5: *The experiment set-up with target positioned 170 cm from the isocentre (detector is hidden within the lead blocks).*

3.3.1 Data acquisition system

The data-acquisition system for the second set of prompt gamma measurements included the collection of timing pulses in addition to the standard pulse heights used for the first set of measurements. Pictures of this significantly more complex electronic arrangement and the iThemba LABS proton therapy control room are shown in figures 3.6(a) and 3.6(b). A detailed schematic of the components in the data-acquisition system can be seen in Figure 3.7. The data acquisition process started with the $LaBr_3$ detector in which any detected gamma produced a light pulse in the scintillating material that was captured by the photo multiplier tube (PMT) and amplified by the built-in preamplifier (PREAMP). This analog signal was then split and produced both the final pulse height signal and a portion of the final timing data. For the pulse height data, the signal passed through an amplifier (AMP) and a delay amplifier (DA) before being collected by the Multiparameter Data Acquisition system (MPA4) in coincidence with the timing signal. For the timing data, the signal from the detector was fed into a Constant Fraction Discriminator (CFD) [Canberra 1428A], which converted the wide, signal pulse into a sharp, nanosecond timing pulse occurring at the beginning (cross-over point) of the detector signal pulse. This then acts as the start pulse to determine the time-of-flight (TOF) of the photon. The stop pulse originates from the sinusoidal

(a)

(b)

Figure 3.6: *(a) Data acquisition set-up outside the treatment room. (b) Control console of the iThemba LABS proton beam treatment nozzle.*

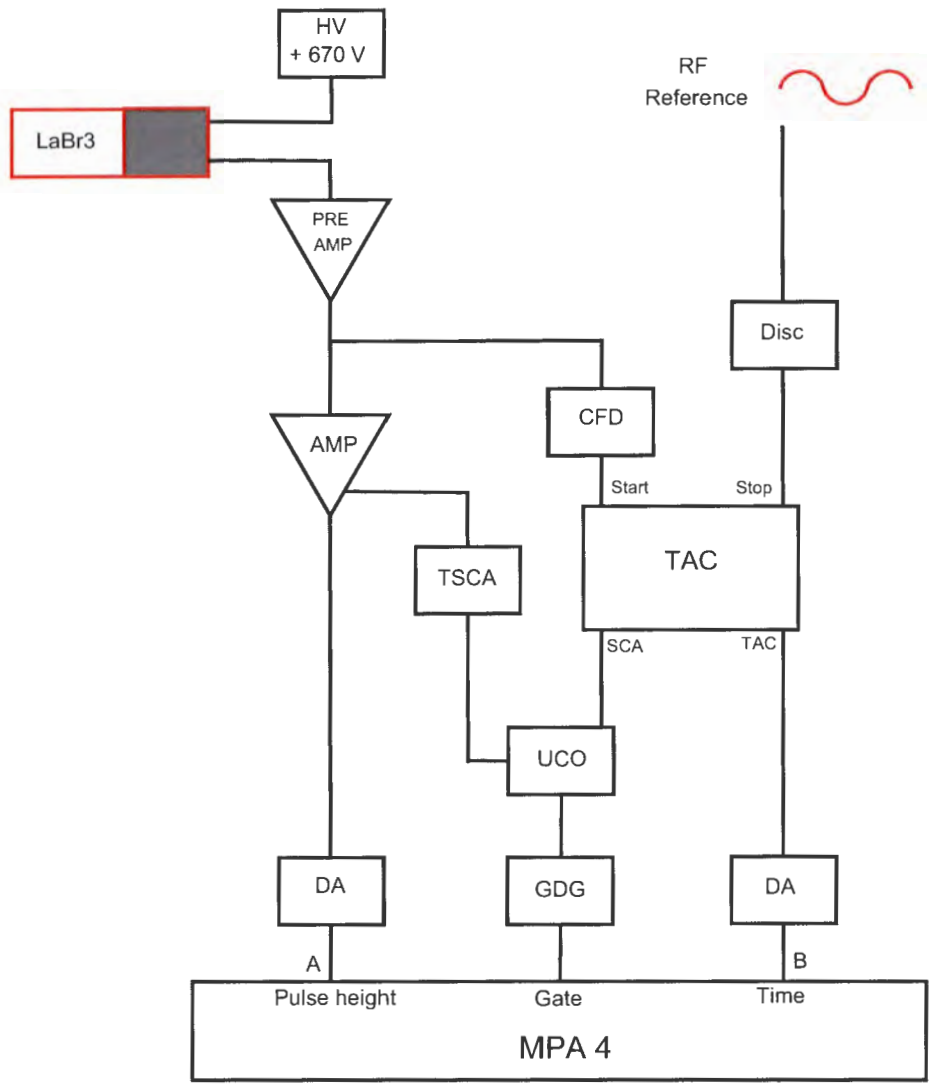

Figure 3.7: *Schematic diagram of the data acquisition set-up: HV - High Voltage, PREAMP - Preamplifier, AMP - Amplifier, DA - Delay Amplifier (427A), Disc - Pulse Discriminator, CFD - Constant Fraction Discriminator (1428A), TAC - Time to Amplitude Convertor or Time Analyser (ORTEC 567), TSCA - Timing Single Channel Analyzer (ORTEC 551), UCO - Universal Coincidence (ORTEC 418A), GDG - Gate and Delay Generator (ORTEC 416A) and MPA4 - Multiparameter Data Acquisition system.*

RF reference signal coming directly from the cyclotron (the RF period was 38.5 ns). The RF reference signal was also filtered through a discriminator (Disc) in order to produce sharp, nanosecond pulses. Both timing pulses entered the Time to Amplitude Convertor or Time Analyser (TAC) [ORTEC 567] where the time interval (Δt) between the start and stop pulses was measured. The TAC generated an output pulse whose height was proportional to the measured time interval for each detected gamma. The Universal Coincidence (UCO) unit [Ortec 418A] performed coincidence-filtering of the pulse height and the time interval signals, ensuring that coincident events were captured. While recording the prompt gamma measurement data, the MPA4 captured in list-mode all of the pulse height and time interval data as well as displaying this data simultaneously as a two-dimensional plot. The list-mode data capture gives the ability to retrospectively analyse a wide range of timing and pulse height combinations through selective gating. For system calibration, the TAC relied on using the weak background radiation presence in the proton vault and the MPA4 was calibrated using standard radioactive sources ^{137}Cs, ^{241}AmBe and ^{207}Bi. Due to the beam current fluctuations that can occur during lengthy measurements, an independent charge count was also collected during each measurement. This independent charge count (listed in Table 3.2) came from the monitor ionization chamber described in Section 2.3.9 and provides a relative charge comparison between the individual runs.

3.3.2 Measurement of prompt gamma production as a function of depth

Additional measurements were made on 24^{th} and 25^{th} May 2014 specifically to determine the prompt-gamma production within the target as a function of depth along the beam direction. The same set-up as described in Section 3.3 was used with the target 170 cm from the isocentre; the only difference was a thinner opening in the lead collimator, using a rectangular opening 1 cm width and 10 cm high. The depth measurements were carried out for the water and the Perspex phantoms at positions around the depth corresponding to the location of the Bragg peak. For the Perspex target, the Bragg peak (BP) is located 20.8 cm from the front face of the target and measurements were performed with the collimated detectors lined up at depths of 10 cm, 17.5 cm, 20 cm, 21 cm, 23 cm and 25 cm or -10.8 cm, -3.3 cm, -0.8 cm, +0.2 cm, +2.2 cm and +4.2 cm relative to BP. For the water target, the Bragg peak is located 23.6 cm from the front face of the target and measurements were performed at depths of 11.5 cm (-12 cm from

Table 3.2: *Summary of prompt gamma measurements with the target 170 cm from the isocentre. (*Detector positions measured from the front surface of the phantom.)*

Date	Target	Monitor Ion-chamber Reading	Beam Current (nA)	Acquisition Time (s)	Depth* (cm)	Collimator (cm^2)
24^{th} May 2014	No (Background)	859757	0.5 -1.0	1200		5 x 10
	Perspex	1166006	0.5 -1.0	1200	20.8	5 x 10
	Water	673092	0.5 -1.0	1200	24	5 x 10
	Water	922929	0.5 -1.0	2000	24	5 x 10
	Graphite	966668	0.5 -1.0	1200	11.8	5 x 10
	Liquid Nitrogen	1550510	0.5 -1.0	2000	32.7	5 x 10
24^{th} May 2014	Perspex	991525	0.5 -1.0	1211	10	1 x 10
	Perspex	1086316	0.5 -1.0	1200	17.5	1 x 10
	Perspex	1037955	0.5 -1.0	1200	20	1 x 10
	Perspex	1054816	0.5 -1.0	1800	21	1 x 10
	Perspex	733478	0.5 -1.0	1204	23	1 x 10
	Perspex	937653	0.5 -1.0	1200	25	1 x 10
	No (Background)	1897663	0.5 -1.0	1200		1 x 10
25^{th} May 2014	Water	1702868	0.5 -1.0	1200	11.5	1 x 10
	Water	1660439	0.5 -1.0	1241	20	1 x 10
	Water	1400789	0.5 -1.0	1209	22.5	1 x 10
	Water	2160436	0.5 -1.0	1466	23.5	1 x 10
	Water	1945127	0.5 -1.0	1200	25	1 x 10
	Water	1179126	0.5 -1.0	1095	27	1 x 10

BP), 20 cm (-3.5 cm from BP), 22.5 cm (-1 cm from BP), 23.5 cm (0 cm from BP), 25 cm (+1.5 cm from BP) and 27 cm (+3.5 cm from BP). Each measurement was taken with a data-acquisition time of 1200 seconds and a beam current at isocentre between 0.5 and 1.0 nA. At the start of each set of depth measurements, a background spectrum was also obtained with the target removed from the beam line.

Estimation of number of prompt gammas from experimental energy spectra

For each of the measured gamma energy spectra, an estimate of the number of prompt gammas for the relevant peaks, typically the 4.44 MeV peak (from ^{12}C) and the 6.13 MeV peak (from ^{16}O) and their escape peaks, was determined in order to make appropriate comparisons. A simple technique of fitting a baseline using a polynomial fit to the background-subtracted energy spectra (as shown in Figure 3.8) was used. The

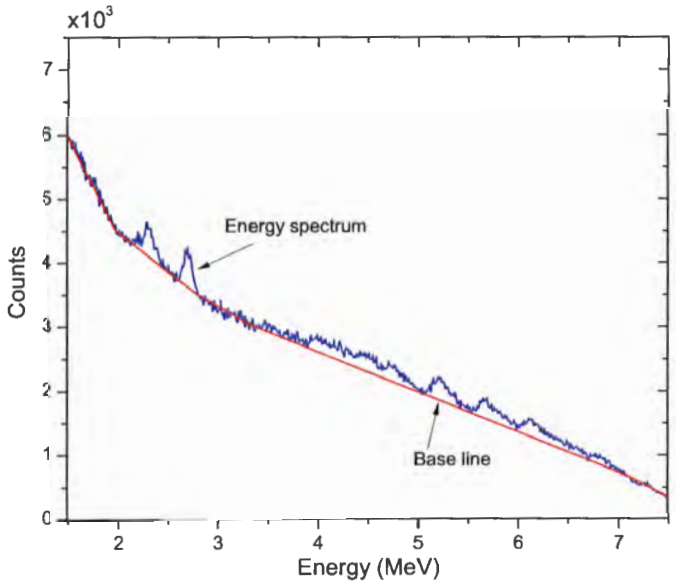

Figure 3.8: *Energy spectrum fitting with assumed smooth baseline (solid line).*

baseline was subtracted from the spectra and the resulting peaks were then integrated in order to determine the prompt gamma count. When looking at the prompt gammas produced over an energy range (like 3 - 7 MeV), the baseline-subtracted spectra was used and the total number of gammas in the desired energy range was used. The uncertainty for each peak value was calculated by integrating over the peaks several times with slightly different baselines.

3.4 Comparison of prompt gamma measurements to Monte Carlo simulations

Each of the experimental setups described in this section was modelled, along with the passive-scatter beam line, in Geant4. The measured prompt gamma spectra were then compared to simulated prompt gamma spectra. Due to the lack of appropriate data for an absolute comparison using the first set of data, the simulated spectra were scaled by a factor which is presented in the caption of each comparison in Section 5.3. For the second set of data, an absolute comparison between simulations and experiments were done calculating the number of discrete prompt gammas detected per

incident proton hitting the target as described in Section 5.4 providing an independent comparison. For each simulated spectra, 2 x 10^{10} primary protons were simulated using 256 processors requiring 150 hours of CPU time on each processor, with the computing resources provided by the Centre for High Performance Computing (CHPC). For the depth measurement comparison, simulations were performed for both targets at 10 different depths between 10 cm and 25 cm. Each depth simulation was repeated 10 times in order to estimate the statistical uncertainty in the results. The independent charge count also gives an absolute comparison between the prompt gamma measurements and the Monte Carlo simulations.

Part III

Results and Discussion

Chapter 4

Geant4 Monte Carlo simulations of prompt gamma production

This is the first analysis chapter, which contains the results of all the simulation work described in Chapter 2. The primary aim of the work presented in this chapter is to develop a Monte Carlo model of the experimental setup (passive-scattered proton beam line, phantom set-up and detector) and to test various Geant4 physics models for discrete gamma emission from the excited states of ^{16}O, ^{12}C and ^{14}N, the most abundant elements in human tissue, against the currently available experimental cross-section data. Several Geant4 parameters (number of excitons (n), Doppler broadening, Fermi breakup and Geant4 inelastic reaction cross-section data set) were also tested to identify areas of weakness and to line up the simulations as closely as possible to the experimental cross section data. These results prompted modifications to the physics settings in our Geant4 beamline simulations. Finally, we validated the iThemba LABS beam line and detector models. We have included a detector response function that reproduced the actual detector response. Once the physics was appropriately modelled, the two basic proton therapy nozzle designs (pencil beam and passive-scatter beam) are used to investigate the characteristics of the prompt gammas emitted from a water phantom.

4.1 Assessment of the Geant4 physics models for prompt gamma emission

The plan of this work is to assess the various Geant4 models (the binary cascade (BIC), precompound (PRECO) and intra-nuclear cascade (INCLXX)) and the relevant cross-section data sets (Willish and Axen (1996) and Tripathi et al. (1999)) in order to get a model that most closely resembles the experimental cross-section data and to have a good starting point for the subsequent prompt gamma simulations.

4.1.1 Effect of Doppler broadening

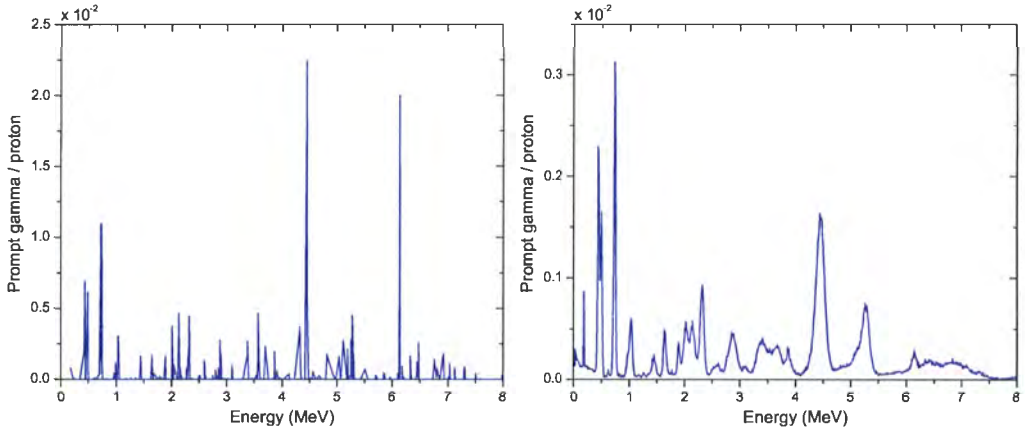

(a) (b)

Figure 4.1: *Prompt gamma emission spectra created within ^{16}O target (a) without and (b) with Doppler broadening applied. The simulation was performed with precompound model for 200 MeV active proton beam.*

Doppler broadening is the broadening of the lines in a prompt gamma spectra due to the different velocities of the nuclei during the emission of gammas produced in proton-nuclear collisions (Doppler effect). Figure 4.1(a) and Figure 4.1(b) were performed with all the same input parameters in the simulation except applying the Doppler broadening setting within the Geant4. As illustrated in Figure 4.1(a), the prompt gamma peak for a given nuclear de-excitation without the Doppler broadening is a narrow single line at the energy corresponding to the specific nuclear transition. Figure 4.1(b) shows that applying the Doppler broadening setting within a Geant4 simulation underestimates the prompt gamma peak at 6.13 MeV produced by proton inelastic collisions on ^{16}O, but the

prompt gamma peaks at 4.44 MeV and 5.20 MeV are reasonably estimated so that the total number of prompt gamma corresponding to each peak before and after applying the Doppler broadening are almost equal. Since the prompt gamma line at 6.13 MeV is the most expected experimentally (see Figure 1.16), the Doppler broadening effect was disabled using the environment variable G4AddTimeLimitToPhotonEvaporation to break the 4-momentum balance of the de-excitation. Therefore, the energy balance is considered for the prompt gamma emission directly from the specific transition assuming that the isotope is at rest.

4.1.2 Total non-elastic proton-nuclear cross-section comparison

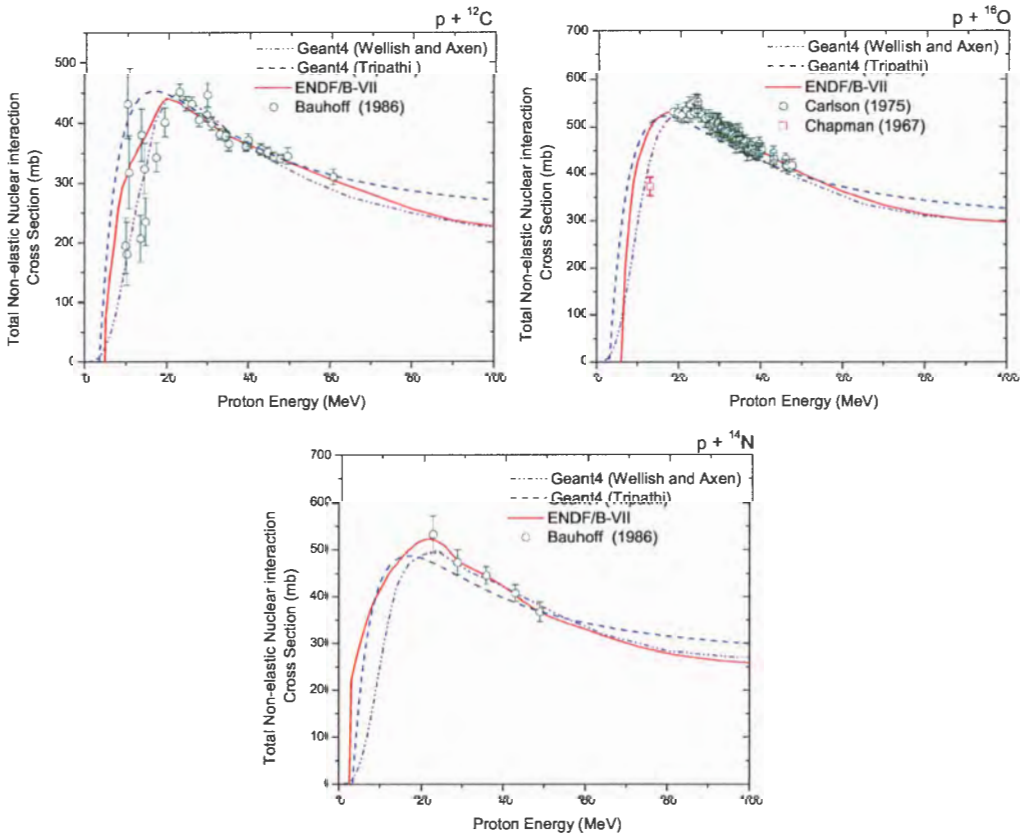

Figure 4.2: *Comparison of total non-elastic cross-section data for proton induced reactions on ^{16}O , ^{12}C and ^{14}N targets.*

A comparison of the simulated and experimental total non-elastic cross-sections for proton-induced nuclear reactions on ^{16}O, ^{12}C and ^{14}N is shown in Figure 4.2. As

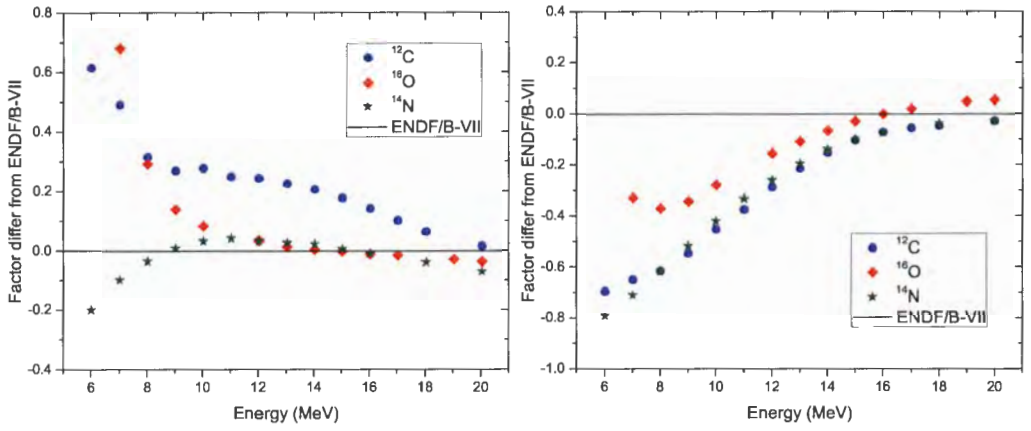

Figure 4.3: *Deviation of the Geant4-generated total nonelastic cross-sections for (a) Tripathi et al. (1999) and (b) Willish and Axen from the ENDF/B-VII data-set.*

expected, no inelastic nuclear reactions are seen below about 5 MeV because any lower energy protons are only scattered elastically; several MeV of energy is required for a proton to penetrate the Coulomb barrier of the target nucleus and produce a nuclear reaction. In Geant4, the default cross-section of Willish and Axen is provided for proton inelastic nuclear reaction. The alternative total cross-section for light systems is the Tripathi data-set (Tripathi et al. (1999)) which increases more rapidly at low incident proton energies compared to the cross-section of Willish and Axen (see Figure 4.2). The cross-section data is especially important between 7 MeV and 15 MeV, as the maximum cross-section for the 6.13 MeV prompt gamma emission from ^{16}O is at 13 MeV and at 10 MeV for the 4.44 MeV emission from ^{12}C (Dyer et al. (1981)).

Since direct experimental data for proton-induced total non-elastic cross-section from ^{16}O, ^{12}C and ^{14}N shown in Figure 4.2 were measured in the astrophysical environment and incomplete in the low energy region (below 20 MeV), the ENDF/B-VII library was used to evaluate the Geant4 simulation. The ENDF/B-VII provides a standard nuclear data for use in all nuclear applications and were evaluated from experimental nuclear data results (Chadwick (2012)). Any unmeasured data in ENDF/B-VII were generated using nuclear reaction models benchmarked to experimental data. Figure 4.3 shows the deviation of the simulated cross-section results from the standard ENDF/B-VII data-set values for the three elements (^{12}C, ^{16}O and ^{14}N). In Figure 4.3(a), we can see that the total inelastic cross-section of Tripathi et al. (1999) shows good agreement with

the ENDF/B-VII database between the 7 - 15 MeV energy range mentioned above, particularly for ^{16}O and ^{14}N. On the other hand, the cross-section of Willish and Axen shows a large discrepancy below 15 MeV (see Figure 4.3(b)) with a slightly larger and almost identical deviation from the ENDF/B-VII data for the non-elastic cross-sections of ^{12}C and ^{14}N. Looking specifically at the peak regions, at 10 MeV for ^{12}C, the deviation seen in Figure 4.3(a) is a little bit high (+0.27), but significantly better than the shift (-0.45) seen in Figure 4.3(b). Based on this comparison, it is clear that the cross-section data of Tripathi is a better choice for ^{12}C and ^{14}N simulations in the energy range 9 - 11 MeV. In the energy range (12 -14 MeV) surrounding the ^{16}O peak, both cross-section data-sets show a reasonable deviation [(-0.15 to -0.06) in case of Willish and Axen and (-0.13 to -0.04) in case of Tripathi et al. (1999)], thus not providing a clear best choice for ^{16}O.

4.1.3 Comparison of Geant4 physics models for inelastic proton-nuclear collisions

In Figure 4.4(a), three different Geant4 physics models of low-energy inelastic nuclear reaction were compared in order to assess their validity for prompt gamma production, specifically for a 200 MeV pencil proton beam hitting a water phantom. These results clearly show that the highest production rate is from the 5.180 MeV prompt gamma line resulting from the excited state of $^{15}O^{*}$ whereas the highest expected production gamma line (the 6.13 MeV peak of $^{16}O^{*}$) is extremely low for all three models. Moreover, it must be noted that the 5.180 MeV prompt gamma line should be the third most prominent emission in the energy range 3 - 7 MeV (see Figure 1.16).

Looking specifically at the Precompound model (PRECO) as seen in Figure 4.4(b), altering the number of excitons (n) shows a clear shift in the height of these peaks. From Figure 4.4(b), we see that use of $n = 2$ increased the peak at 6.13 MeV by a factor of 4.5 while decreasing the peak at 5.180 MeV by a factor of 0.9 from the default value of $n = 3$. In Geant4, the initial precompound stage is calculated by summing the initial information from the target nucleus and incident proton. Since the target nucleus in its ground state is at rest, the initial precompound stage mostly depends on the incident proton. In the model, the default number of excitons in the initial precompound nuclear stage is taken as $n = 3$ (2p, 1h). The statistical equilibrium is characterized by an equilibrium number of excitons. Each allowed transition to a new state with a change in number of excitons by $\Delta n = 0$ or ± 2.

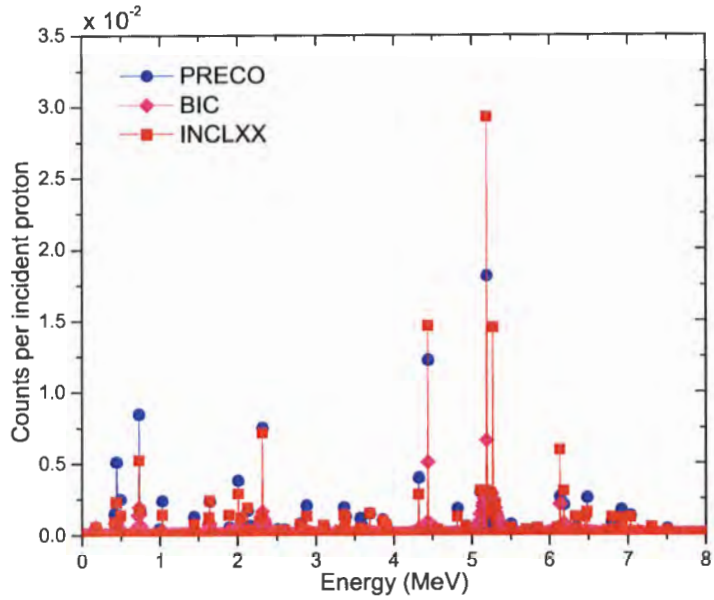

(a)

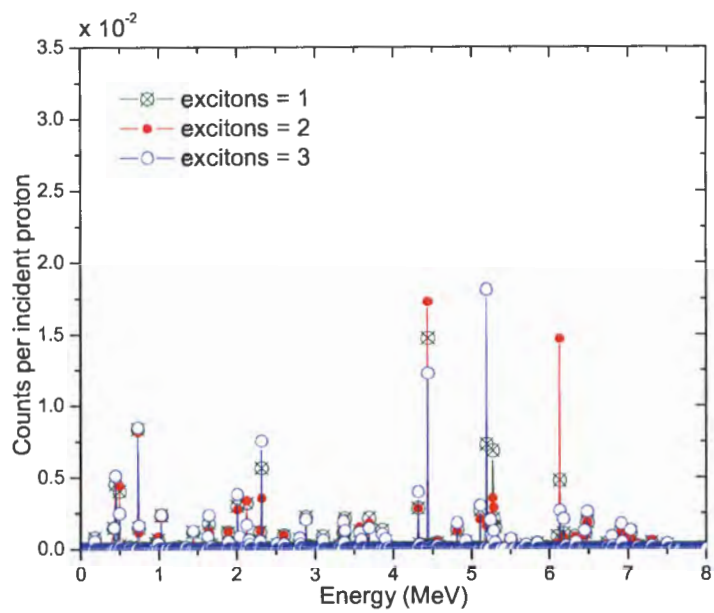

(b)

Figure 4.4: *(a) Comparison of the simulated prompt gamma spectra for three different Geant4 physics models: PRECO, BIC and INCLXX. (b) Comparison of prompt gamma spectra produced with different number of excitons (n = 1, 2 and 3) by the PRECO model.*

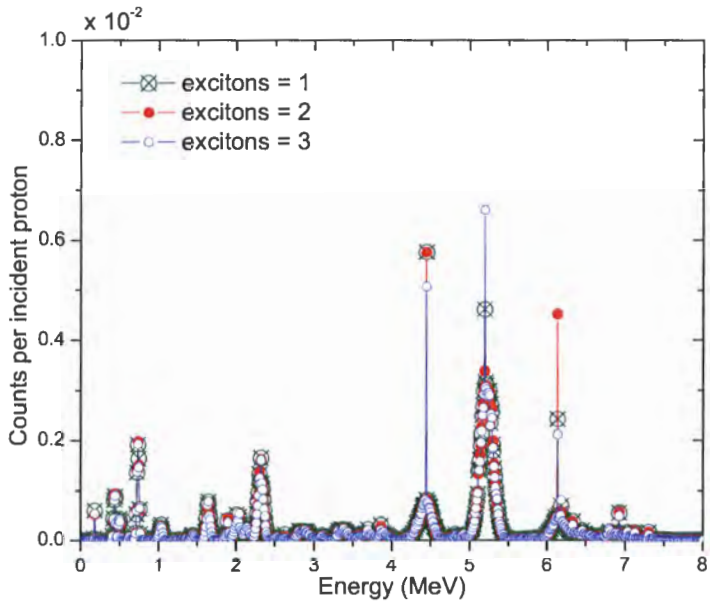

Figure 4.5: *Comparison of simulated prompt gamma emission in water for different numbers of excitons (n = 1, 2, and 3) using the binary cascade model*

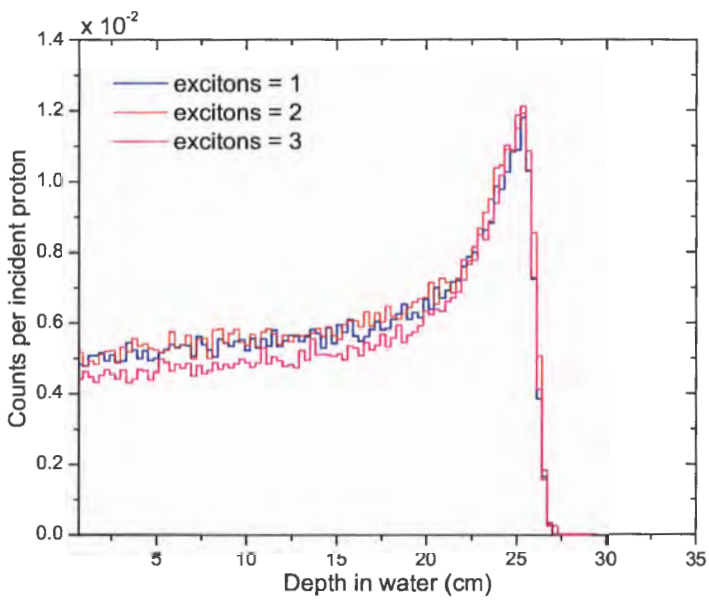

Figure 4.6: *Comparison of simulated prompt gamma emission in water for different initial exciton numbers (n = 1, 2, and 3) using the Precompound model*

As illustrated in Figure 4.5, the initial exciton number also impacts the BIC model, which uses the precompound model at the end of the cascading phase of a nuclear de-excitation of a residual nuclear system. As a result, the initial residual compound system will have its own exciton number and will be considered the initial precompound system for any further nuclear deexcitation processes. It is also noted that there is an unexpected broadening in the peaks in the spectrum even after removing the Doppler broadening effect. Figure 4.6 shows a comparison of prompt gamma creation within a water target for three different initial exciton numbers $n = 1, 2$ and 3 in the Precompound model. The prompt gamma emission obtained with number of excitons $n = 2$ is higher than the emission obtained with the default excitons $n = 3$ by about 6 % in total.

4.1.4 Simulation of discrete elemental prompt gamma emission

In this section, we will look at the discrete prompt gamma emission from the excited nuclei of ^{12}C, ^{16}O and ^{14}N, the most abundant elements in tissue, by comparing them with the available experimental reaction cross-section data published in Kiener et al. (1998), Dyer et al. (1981), Belhout et al. (2007), Narayanaswamy et al. (1981), Lang et al. (1987), Lesko et al. (1988) and Benhabiles-Mezhoud et al. (2011). The three Geant4 physics models (Binary cascade, Precompound and Intra-nuclear cascade) and the two cross-section data-sets (Willisch and Axen, and Tripathi) will be compared, with a preference given to the Precompound model with an intial exciton number of $n = 2$ using the Tripathi data-set, based on the results from the previous section.

Simulation of discrete lines for ^{12}C

The prominent 4.439 MeV gamma from the $^{12}C(p,p')^{12}C$ reaction is emitted by the de-excitation of the first excited state and is the only particle-bound excited state of ^{12}C (Belhout et al. (2007)). Spallation reactions of ^{12}C do produce gammas from ^{10}B, ^{11}B and ^{11}C (Kozlovsky et al. (2002b) and Lang et al. (1987)), where the 4.445 MeV gamma induced by the $^{12}C(p,2p)^{11}B$ contributes significantly to the 4.44 MeV peak. Prompt gamma production cross-section results for these specific reactions are shown in Figures 4.7 and 4.8, comparing the different Geant4 physics models and the various experimental data results. The two figures are identical except for the simulated cross-section data sets used; the default Wellisch and Axen was used in figure 4.7 and

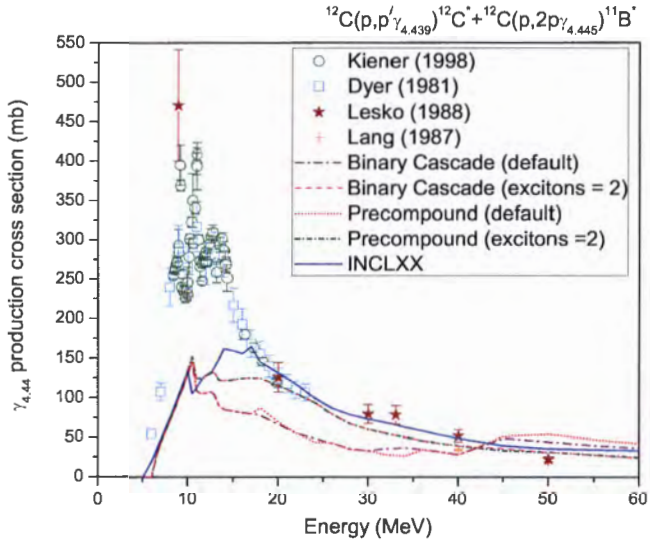

Figure 4.7: *4.44 MeV gamma production cross-section for proton-induced reactions on ^{12}C using the total inelastic cross-section data from Willish and Axen.*

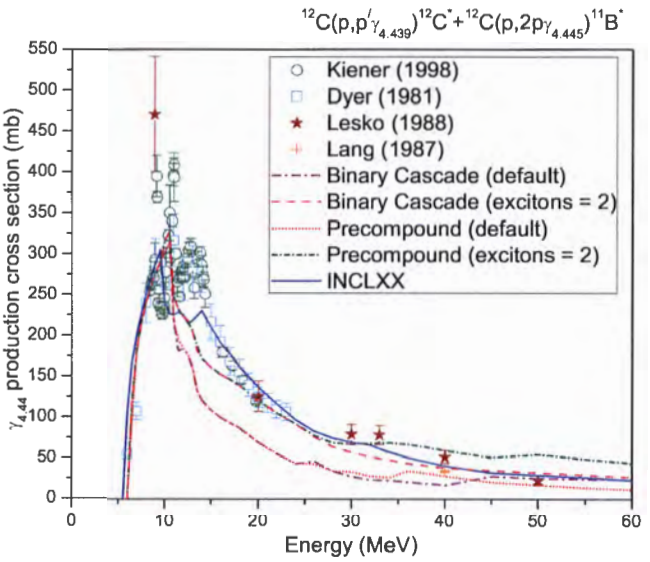

Figure 4.8: *4.44 MeV gamma production cross-section for proton-induced reactions on ^{12}C using the total inelastic cross-section data from Tripathi.*

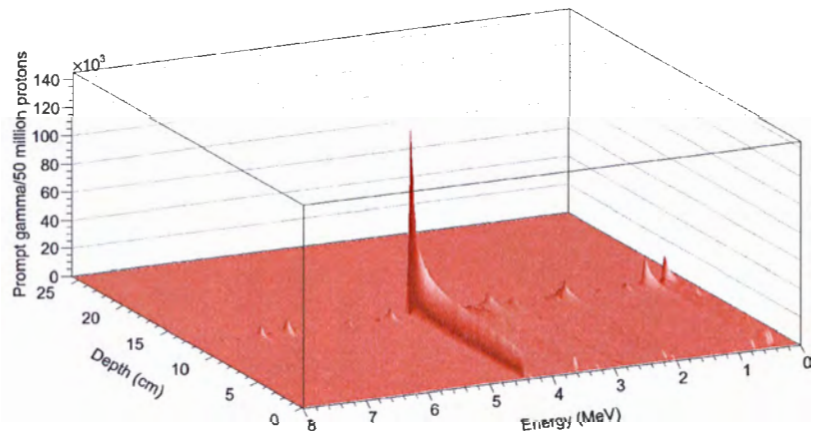

Figure 4.9: *Prompt gamma production from a 200 MeV proton pencil beam on a carbon target as a function of the gamma energy and position within the phantom. Simulation performed with the precompound model ($n = 2$) and the cross section data from Tripathi.*

the Tripathi data set was used in figure 4.8. The cross-section results for both the BIC and the PRECO models exhibit quite similar trends for both data sets, whereas the INCLXX gives a better response above proton energy $\sim$ 15 MeV for both data-sets. Comparing the two figures, it is easy to see that the results obtained with the total inelastic cross-section of Tripathi et al. (1999) are in better agreement with the experimental data than the results obtained with the default total inelastic cross-section of Wellisch and Axen. The figures also show that the simulations performed using the modified initial nuclear exciton state of $n = 2$ (1p, 1h) giving a better fit to the experimental data than the default model. Figure 4.9 shows the number of prompt gammas produced from a carbon target as a function of gamma energy and depth in the target simulated using a pencil beam of 50 million 200 MeV protons using the precompound ($n = 2$) model with the Tripathi data-set.

Simulation of discrete lines for ^{16}O

The direct inelastic nuclear collision between a proton and an oxygen nucleus ($^{16}O(p, p'\gamma)^{16}O$) produces peaks at 2.742, 6.129, 6.916 and 7.115 MeV (Dyer et al. (1981), Narayanaswamy et al. (1981), Lang et al. (1987), Lesko et al. (1988), Kiener et al. (1998) and Belhout et al. (2007)). Other possible peaks can be seen at 0.718,

1.022, 1.635, 2.313, 3.684, 3.853, 4.438, 5.105, 5.180, 5240, 5.269, 5.298, 6.175, 6.322 and 7.299 MeV (Kozlovsky et al. (2002b)). Among them the 4.438 MeV prompt gamma from the $^{16}O(p,p'\alpha\gamma_{4.438})^{12}C$ reaction is the prominent emission observed for incident proton energies above 15 MeV (Dyer et al. (1981), Lang et al. (1987), Lesko et al. (1988) and Belhout et al. (2007)). For the four most important lines [6.129, 4.438, 6.916 and 7.115 MeV], a comparison of the prompt gamma production cross-section results for three different settings for the precompound model is shown in Figure 4.10 and a comparison of the prompt gamma production cross-section results for three different physics models is shown in Figure 4.11.

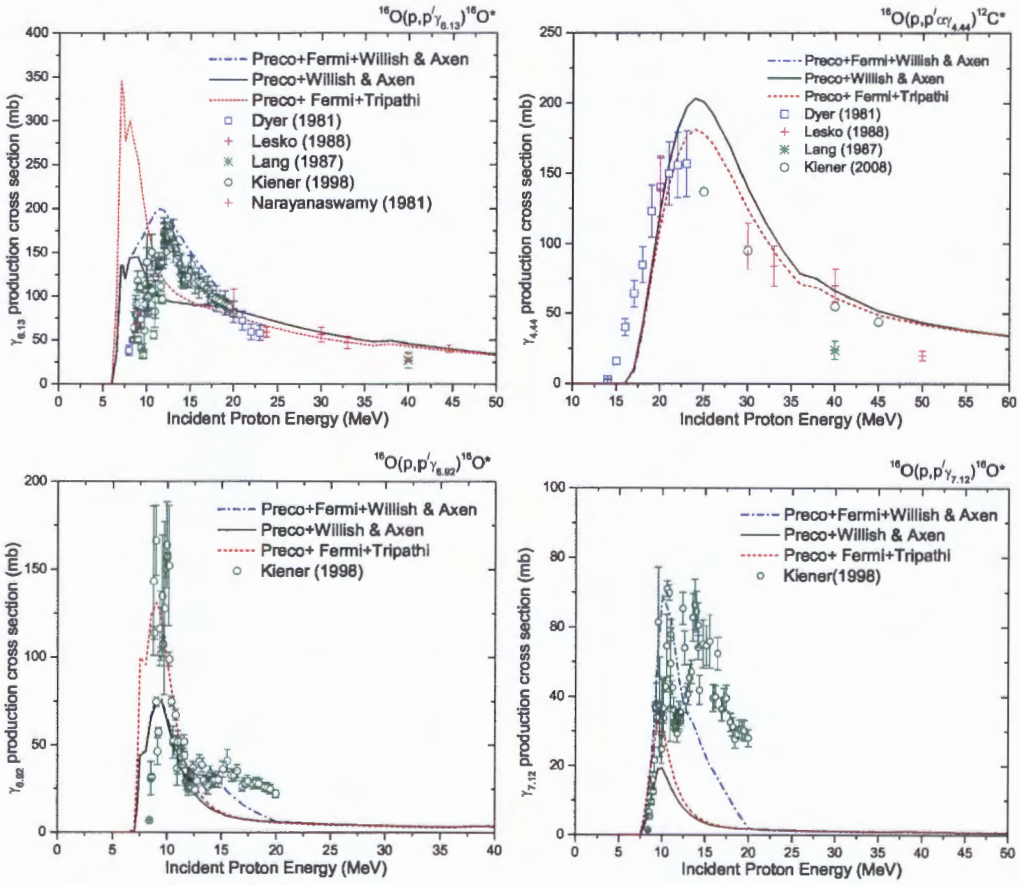

Figure 4.10: *Comparison of experimental and simulated gamma production cross-section for 6.13, 4.44, 6.92 and 7.12 MeV prompt gamma lines emitted by proton-induced ^{16}O nuclear reactions. Simulation were performed with Fermi breakup for both the Willish and Axen and Tripathi data-set and without Fermi breakup for the Willish and Axen data-set. Fermi breakup is activated below 20 MeV and the PRECO model is using the initial exciton number $n = 2$.*

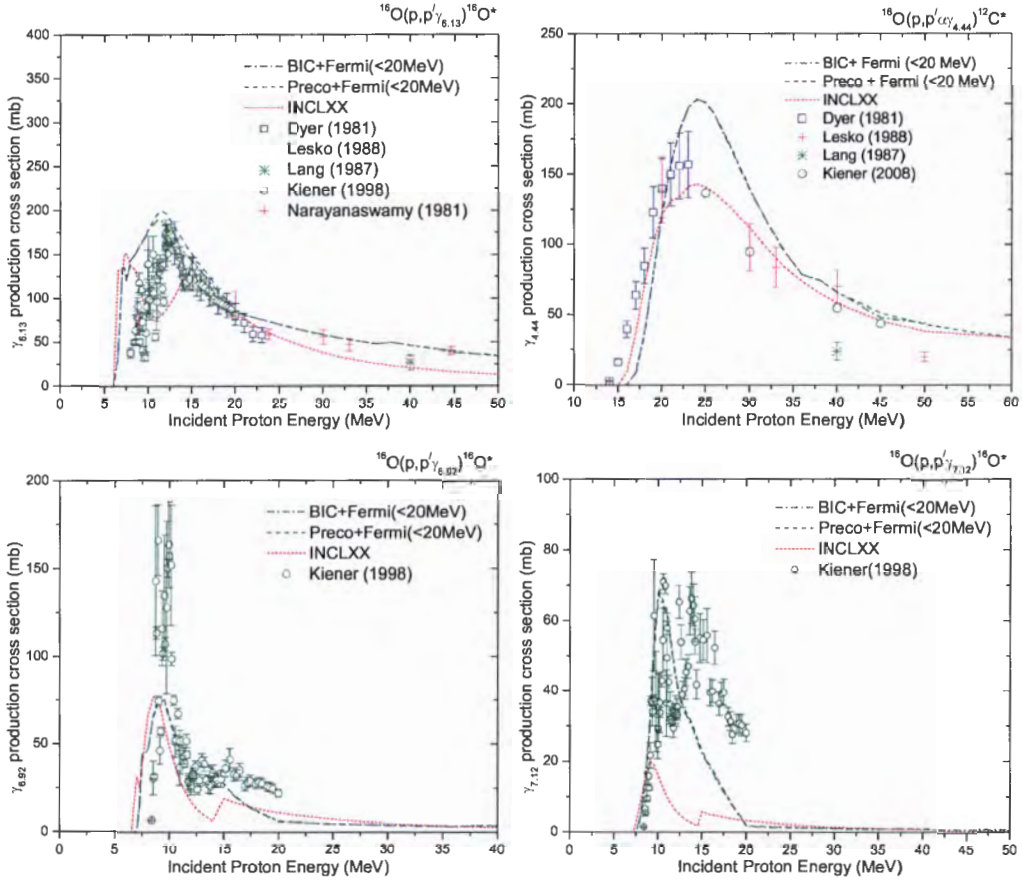

Figure 4.11: *Comparison of experimental and simulated gamma production cross-section for 6.13, 4.44, 6.92 and 7.12 MeV prompt gamma lines emitted by proton-induced ^{16}O nuclear reactions using the Willish and Axen data-set. Fermi breakup is activated for the BIC and PRECO models below 20 MeV and the PRECO model is using the initial exciton number $n = 2$.*

Figure 4.10 provides further comparison of the two Geant4 cross-section data sets (Willish and Axen, and Tripathi) as well as investigating the addition of using Fermi break-up below 20 MeV. According to (Verburg et al. (2012)), the Fermi break-up model is required below 20 MeV for the 6.13 MeV prompt gamma emission because the compound nucleus is handled by the evaporation model, followed by the Fermi break-up for residuals. For the 6.13 and 7.12 MeV results shown in Figure 4.10, there is a clear difference between the precompound model (with Willish and Axen data) with and without the inclusion of the Fermi break-up. While there is little difference in the 4.44 and 6.92 MeV, the Fermi break-up clearly provides better agreement with experimental data and

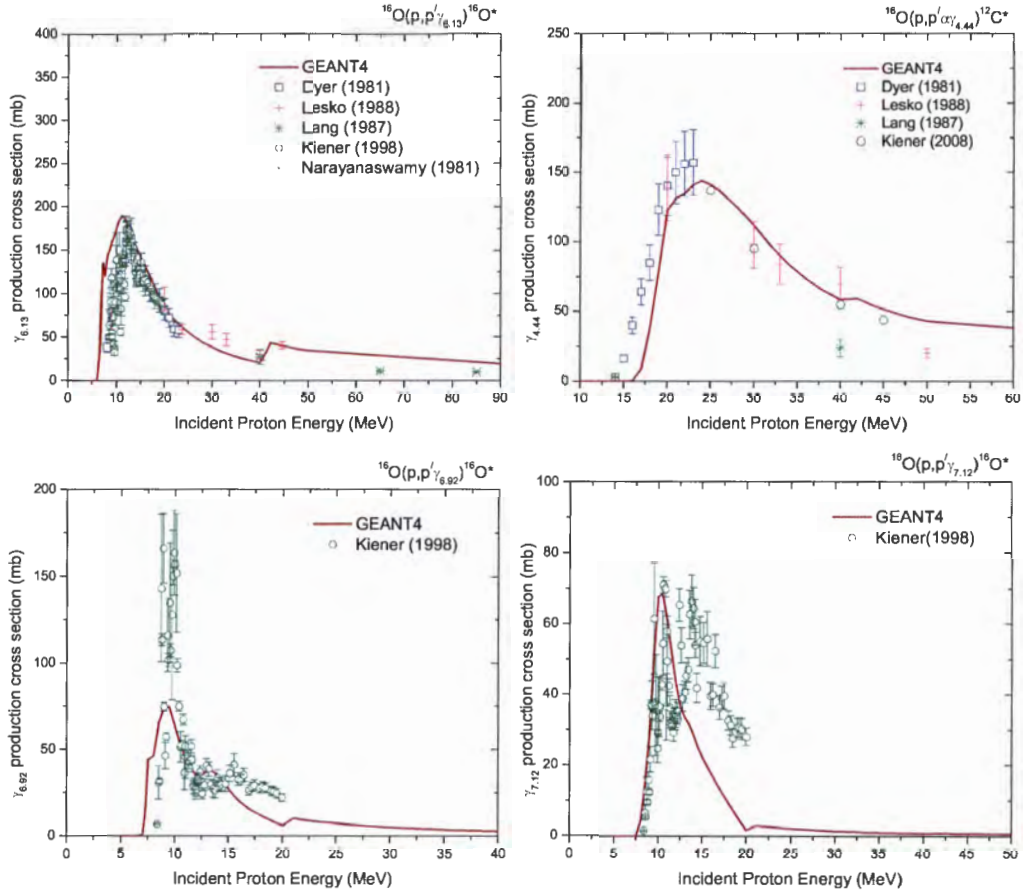

Figure 4.12: *Simulations reproduced with BIC (0-19 MeV), INCLXX (19-40 MeV), PRECO (40-300 MeV) and Fermi breakup below 20 MeV for proton-induced nuclear reaction on ^{16}O. The PRECO model is using the initial exciton number $n = 2$.*

its inclusion is justified. The results using the two different cross-section data sets in Figure 4.10 shows that the Wellish and Axen cross-section produces better agreement for the 6.13 and 7.12 MeV gammas, while the Tripahi data-set models the sharp peak in the 6.92 MeV cross-section results much better and both produce identical results for the 4.44 MeV peak. While these results are not overwhelmingly conclusive, for simulations involving ^{16}O, the cross-section data of Willish and Axen will be used as the default.

Moving forward with the Fermi break-up active below 20 MeV and using the cross-section data-set of Willich and Axen, the three physics models (binary cascade, pre-compound and intra-nuclear cascade) are compared in Figure 4.11. As illustrated in

Figure 4.11, a similarity can again be seen between the BIC and PRECO models, except for very small discrepancies observed in the energy range 10-20 MeV for the 6.129 MeV line. Also, both the BIC and PRECO models overestimate the cross-section at the lowest proton energies for the 6.129 MeV results. The 4.44 MeV prompt gamma-ray emission with INCLXX fits well to the experimental data above 15 MeV while the other two models show an overestimation between 20 and 40 MeV. Unfortunately, for the 6.129 MeV line, prompt gamma production with INCLXX drops deeply at 10 MeV and is poor below a proton energy of 15 MeV. The experimental data for 6.92 MeV gammas indicates that its production has a very narrow peak at low energies, a characteristic that is not observed in any of the Geant4 models. The INCLXX model grossly underestimates the cross-section for the 7.12 MeV line. While the BIC and PRECO models are seen to be suitable to reproduce the 7.12 MeV line, neither could reproduce the broad peak as it is observed experimentally. Among the Geant4 built-in physics models, the precompound model was favourable for prompt gamma emission as it produces a very low rate of 5.180 MeV gamma from the excited state of O^{15*}.

Based on these results, a combined model was considered with the BIC model used below 19 MeV, the INCLXX model used between 19 MeV and 40 MeV and the PRECO model used above 40 MeV, with results shown in Figure 4.12. Fermi break-up was also activated below 20 MeV. These results demonstrate that the combined model gives an improved result over using a single model for ^{16}O.

Figures 4.13 and 4.14 show the prompt gamma distribution as a function of energy and depth in an oxygen phantom using the precompound model and the combined model respectively. The simulations were performed with a 200 MeV pencil beam of 50 million protons. The third most prominent prompt gamma peak observed in the both figures at 5.25 MeV is the result of the mixed 5.270 MeV peak of ^{15}N* and 5.240 MeV and 5.180 MeV peaks of ^{15}O* in which the contribution of the 5.180 MeV is high in the combined model (see Figure 4.14). It also points to the need of comparison for the 5.180 MeV prompt gamma production cross-section which is not included in this thesis because of a lack of experimental cross-section data for the 5.180 MeV emission in the lower proton energy range.

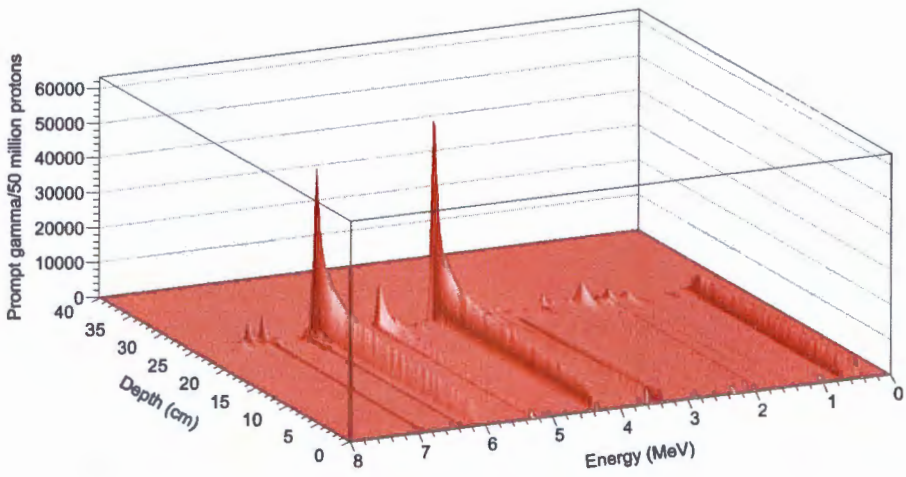

Figure 4.13: *Prompt gamma production from a 200 MeV proton pencil beam on a ^{16}O target as a function of the gamma energy and position within the phantom. Simulation performed with the precompound model ($n = 2$) and the cross-section data from Willish and Axen. Fermi breakup is activated below 20 MeV.*

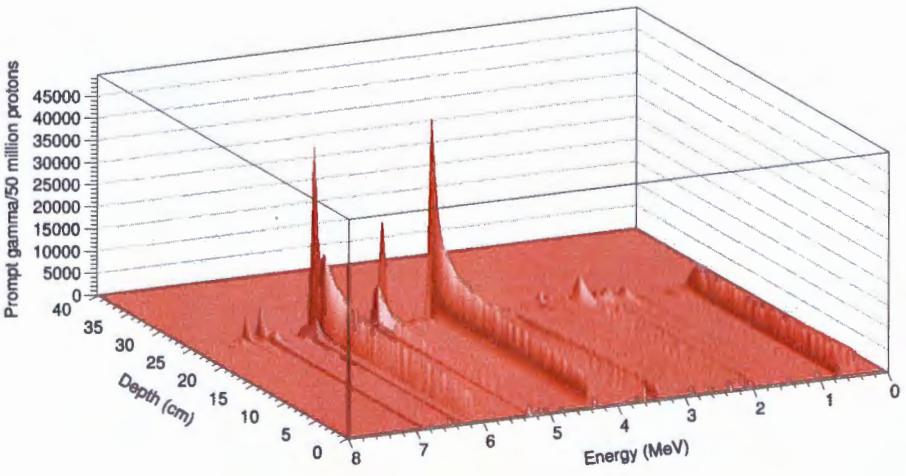

Figure 4.14: *Prompt gamma production from a 200 MeV proton pencil beam on a ^{16}O target as a function of the gamma energy and position within the phantom. Simulation performed with the combined model and the cross-section data from Willish and Axen.*

Simulation of discrete lines for ^{14}N

Benhabiles-Mezhoud et al. (2011) have recently studied the proton-induced gamma emissions from transitions in the first eleven excited states of ^{14}N using a tandem Van de Graaff accelerator over the energy ranges 0.728 - 7.029 MeV. According to their study, the first three excited state of ^{14}N produce the three strongest lines at 2.313, 1.635 (about 50% of 2.313 MeV) and 5.105 MeV. The cross-sections for the remaining lines are less than 25 mb. Comparison of the prompt gamma production cross-section data to simulated results from the different Geant4 physics models for the eight most important prompt gamma lines 0.728, 1.635, 2.313, 2.793, 3.378, 3.890, 5.106, and 7.027 MeV is shown in Figure 4.16. All three models significantly overestimate the cross-section data for the 2.313 MeV and 3.890 MeV gammas above a proton energy of 10 MeV and underestimate the line 1.635 MeV below 12.5 MeV. Simulated results for the other lines show reasonable agreement with the experimental data with the PRECO model producing slightly better agreement. Simulations were carried out using the total inelastic cross-section of Tripathi et al. (1999) that offered a good comparison against experimental data. From the results shown in Figure 4.16, the simulated spectra using the cross section of Wellisch and Axen does not fit as well to the ^{14}N experimental data. The prompt gamma distribution as a function of energy and position performed with the precompound model is shown in Figure 4.17. The strong gamma line observed at 4.44 MeV is the sum of the 4.438 MeV gamma from ^{12}C and the 4.444 MeV gamma from ^{11}B.

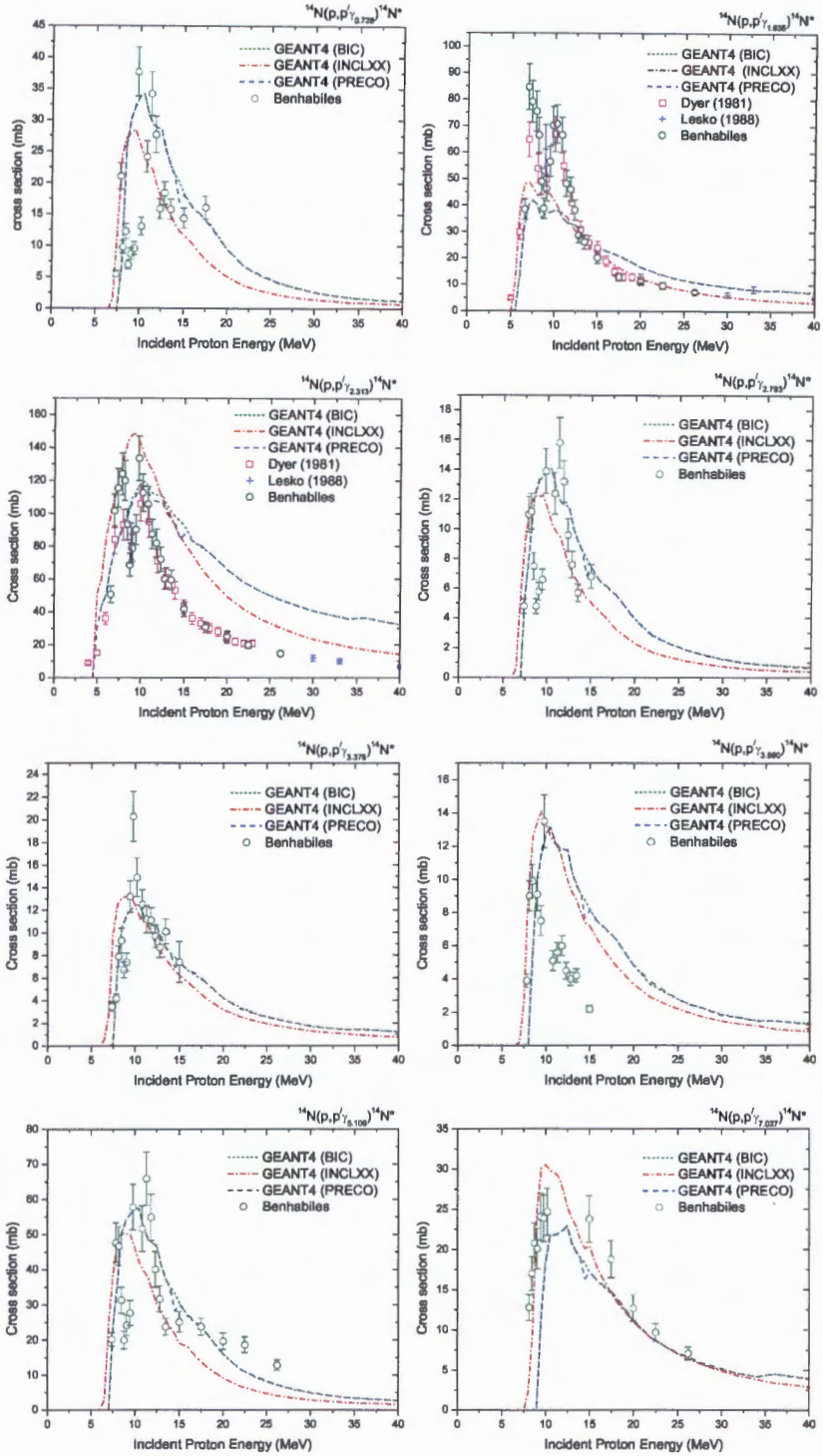

Figure 4.15: *Cross-section of 0.728, 1.635, 2.313, 2.793, 3.378, 3890, 5.106 and 7.027 MeV prompt gammas from proton-induced nuclear reactions on ^{14}N performed with the total non-elastic cross-section of Tripathi et al. (1999). The PRECO model is using the initial exciton number $n = 2$.*

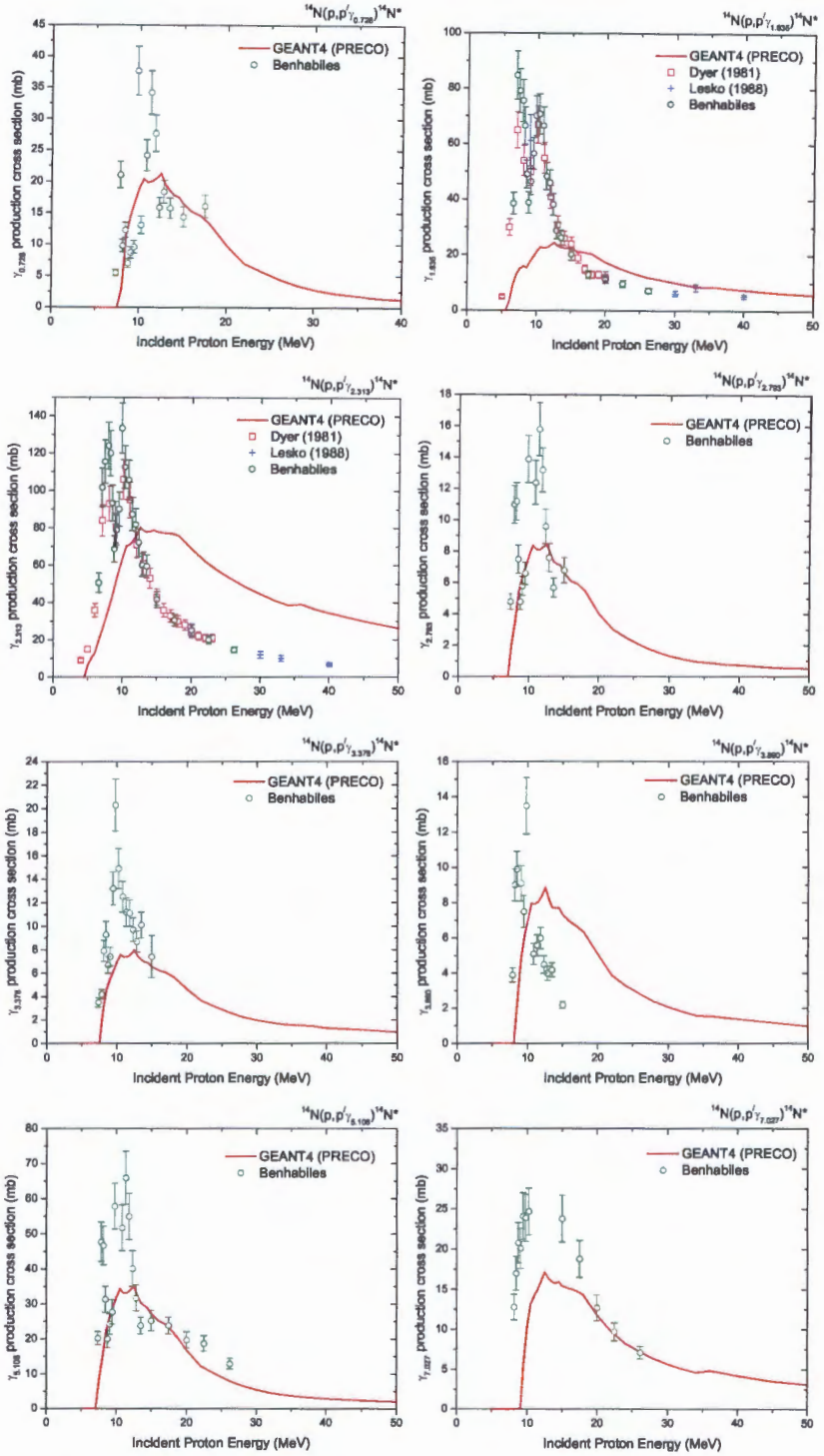

Figure 4.16: *Cross-section of 0.728, 1.635, 2.313, 2.793, 3.378, 3890, 5.106 and 7.027 MeV prompt gammas from proton-induced nuclear reactions on ^{14}N performed with the precompound model using total non-elastic cross-section of Willish and Axen. The PRECO model is using the initial exciton number $n = 2$.*

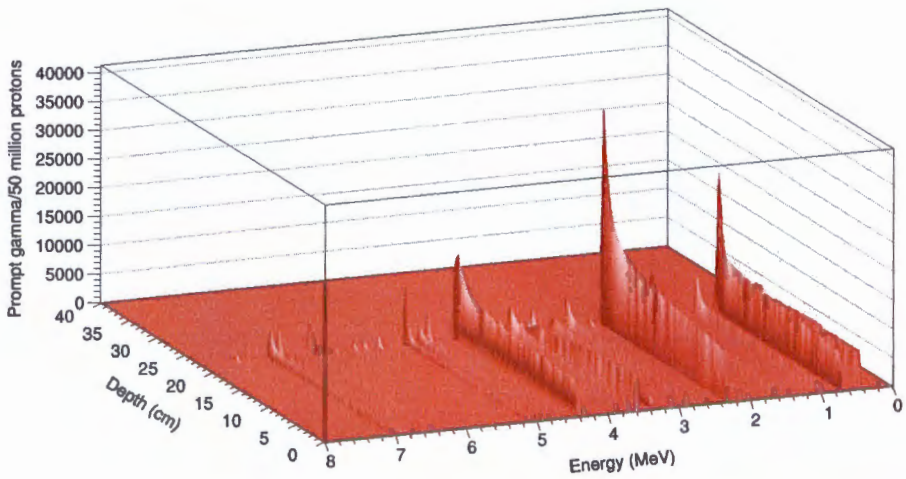

Figure 4.17: *Prompt gamma production from a 200 MeV proton pencil beam on a ^{14}N target as a function of the gamma energy and position within the phantom. Simulation performed with the precompound model ($n = 2$) and the cross-section data from Tripathi.*

4.1.5 Final model

Our physics list QGSP_BIC_EMY was modified based on the cross-section data comparisons discussed above. Despite that the binary cascade model showed reasonably similar discrete gamma production cross-section results to those from the precompound model, the results (Figures 4.4 and 4.5) show that the BIC displays a higher production rate then PRECO for the 5.180 MeV prompt gamma line resulting from the excited state of $^{15}O^*$. Therefore the default binary cascade model for proton inelastic nuclear reactions within the QGSP_BIC_EMY physics package was replaced by the precompound model (0-300 MeV) with the modified initial number exciton $n = 2$.

Since the default total inelastic cross-section of Willish and Axen (1996) has been shown to underestimate the prompt gamma creation at low proton energy for ^{12}C and ^{14}N, the cross-section of Tripathi light ion (Tripathi et al. (1999)) was used alternatively for graphite and liquid nitrogen targets. However, the cross-section data of Willish and Axen was successfully used to simulate water and Perspex targets. In addition, the Fermi break-up was activated for proton energy below 20 MeV (for water and Perspex targets). The selection of final inelastic reaction models for the different elements and materials are summarized in Table 4.1.

Table 4.1: *Summary of the final inelastic reaction models for different elements and materials used in subsequent simulations. The precompound model is applied in the energy range of 0-300 MeV.*

Elements/ materials	**Cross -section**	**Fermi breakup**	**Physics Model**	**Excitons number**
^{16}O	Willish and Axen	< 20 MeV	PRECO	2
water	Willish and Axen	< 20 MeV	PRECO	2
Perspex	Willish and Axen	< 20 MeV	PRECO	2
^{12}C	Tripathi	No	PRECO	2
graphite	Tripathi	No	PRECO	2
^{14}N	Tripathi	No	PRECO	2
Liquid nitrogen	Tripathi	No	PRECO	2

4.2 Validation of the iThemba LABS passive-scatter proton therapy beam line Monte Carlo model

In order to have a valid Monte Carlo model of a proton therapy beam line, it must be able to replicate the dose profiles used for the treatment of patients, specifically the depth dose and lateral dose profiles. The iThemba LABS proton therapy beam line is calibrated before every treatment by measuring the range of the beam, measured at the 50% distal fall-off position in water ($R_{50\%}$). Range trimmer plates are added or removed from the beam to adjust for variations in the beam until the 50% distal position is at 24 cm. For the Monte Carlo model, instead of working backwards from a 24 cm range, we must start with a detailed description of the incoming beam of protons. The expected proton energy exiting the vacuum window into the treatment room is 199.78 MeV, but this value was adjusted to 201.36 MeV in order for our simulations to line up with the measured values (see section 4.2.2 for more details). Figure 4.18 compares the simulated Bragg curve using the adjusted energy (201.36 MeV) to the measured dose profile in water. Figure 4.19 compares the measured vs simulated lateral dose profiles of a 24 cm range proton beam at depths of 10 cm and 23.55 cm (at the Bragg peak) in water. The simulated and measured ranges ($R_{50\%}$) agree within 0.3%.

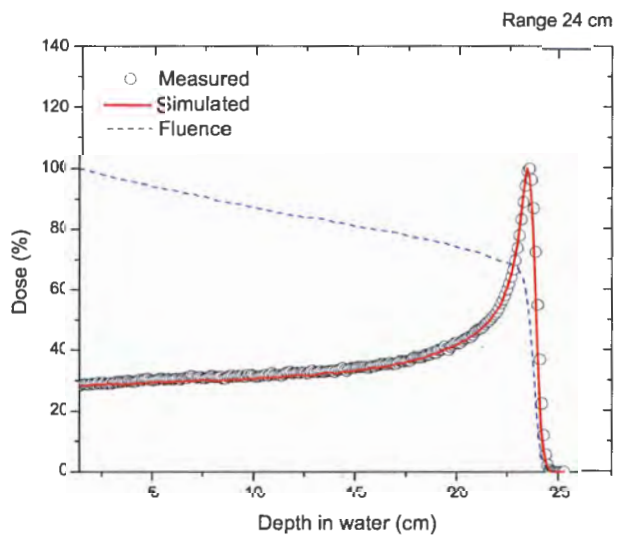

Figure 4.18: *Comparison of the measured and simulated Bragg peaks for a 24 cm range proton beam in water. Maximum values are normalized to the 100% dose level.*

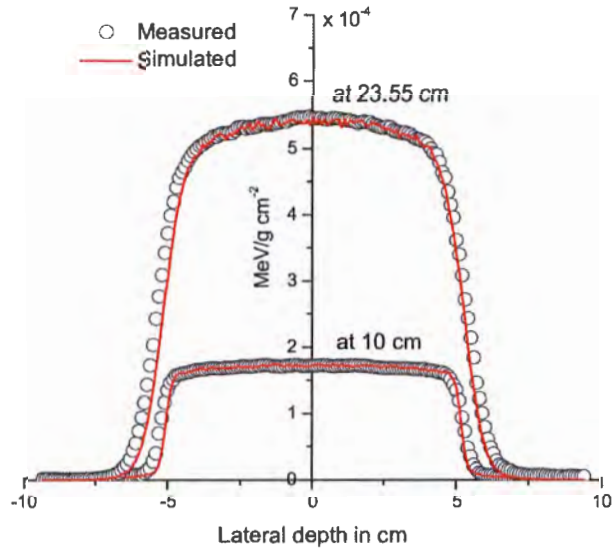

Figure 4.19: *Comparison of the measured and simulated lateral dose profiles at the depths of 10 cm and 23.55 cm for a 24 cm range proton beam.*

4.2.1 Calibration of the double wedge degrader

For ranges less than 24 cm, the double wedge degrader is used to reduce the energy of the beam. Using the Geant4 passive-scatter beam line model, the vertical wedge position (WP) of the double wedge degrader was calibrated against different proton ranges. The resulting data is shown in Figure 4.20. A linear fit of the data was obtained, giving the following relationship:

$$WP(mm) = \frac{Range - a}{b} \tag{4.1}$$

where a and b are constants ($a = 9.39337 \pm 0.00238$ cm and $b = 0.74359 \pm 0.00025$). Figure 4.21 shows the comparison of simulation against experimental results for different proton ranges in water. The agreement between the simulated and measured ranges calculated at the $R_{50\%}$ position for wedge positions corresponding to ranges between 5 and 24 cm is within 0.5%.

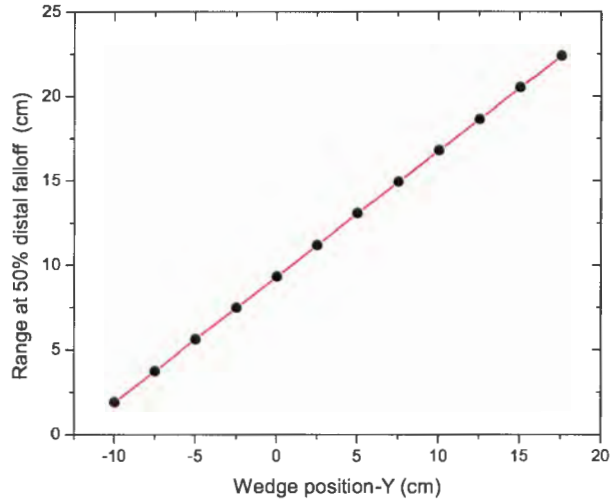

Figure 4.20: *Proton range as a function of wedge position.*

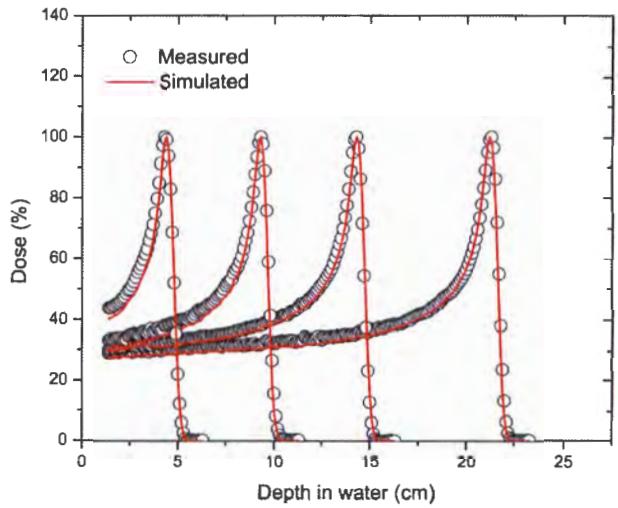

Figure 4.21: *Comparison of simulated dose profiles with measured dose profiles at ranges of 4.82, 9.7, 14.75, 24.0 cm.*

4.2.2 Effect of the mean excitation energy

In the passive-scatter beam line model, a double wedge degrader is used to modify the proton energy in the beam line instead of changing the energy at the cyclotron. It was reported by Paganetti (2012b) that the uncertainty for the reproducibility of the range due to beam-modifying devices in the beam line, such as the double wedge degrader, is about 1.0 mm. Andreo (2009) and Kumazakia et al. (2007) demonstrated the importance of the mean excitation energy of water and its ability to significantly affect range calculations. They estimated a 3 mm spread in the Bragg peak observed for a 122-MeV proton beam. Furthermore these uncertainties also depend on the beam energy.

When a proton moves through matter, it is continually losing energy through excitation or ionization of the surrounding atoms. In Geant4, the continuous energy loss per step in a track is based on the restricted stopping power calculated using the Bethe-Bloch formula. In the Bethe-Bloch equation, the energy deposition per unit length is strongly dependent on both the density and the mean excitation energy[1] (MEE) of the target material. The mean excitation energy can be approximated by $MEE = (10\text{ eV})Z$, where Z is the atomic number of the material. The MEE value for water is 75 $\pm$ 3 eV recommended by ICRU (1993), but 67.2 eV recommended in ICRU (2005). The uncertainty on the MEE value cannot be ignored because other authors have reported a range of different values: 80 $\pm$ 2 eV (Bichsel and Hiraoka (1992)) measured relative to Aluminium (Al) using Bragg curves, 81.8 eV (Janni (1982)) which was used to produce stopping power tables, 77 eV (Krämer et al. (2000)) obtained by matching the measured Bragg peaks of carbon-ions and 78.4 $\pm$ 1.0 eV (Kumazakia et al. (2007)) which was determined from proton beam ranges in water. Furthermore, in the energy range of 10 - 250 MeV, a 0.8 - 1.2% (Kumazakia et al. (2007)) variation in the stopping powers was reported to have the same impact on the absorbed dose as MEE value variations between 75 and 80 eV.

[1] also called mean ionization potential

Table 4.2: *A summary of calculated $R_{50\%}$ values over a range of mean ionization energies in water for 240 mm range protons. The measured value is 240.1 mm ($^{m}R_{50\%}$). $^{IE}R_{50\%}$ is the range simulated with different mean ionization energy (IE) listed in the table. $^{s}\Delta R_{50\%}$ shows the difference between the $^{IE}R_{50\%}$ and the ICRU (1993) range value ($^{75}R_{50\%}$).*

IEnergy (eV)	$^{IE}R_{50\%}$ (mm)	$^{m}\Delta R_{50\%}$ (mm)	$^{s}\Delta R_{50\%}$ (mm)	%
67	232.86	7.2	-3.2	-1.3
70	234.05	6.0	-2.0	-0.8
72	234.86	5.2	-1.2	-0.5
73	235.24	4.9	-0.8	-0.3
75	236.04	4.1	0	0
77	236.82	3.3	0.8	0.3
78	237.19	2.9	1.2	0.5
80	237.85	2.2	2.0	0.8
81	238.27	1.8	2.2	0.9
83	238.99	1.1	2.95	1.2
84	239.33	0.8	3.3	1.4
86	240.03	0.1	4.0	1.7
90	241.40	-0.3	5.4	2.3

$^{m}\Delta R_{50\%} = {}^{m}R_{50\%} - {}^{IE}R_{50\%}$
$^{s}\Delta R_{50\%} = {}^{IE}R_{50\%} - {}^{75}R_{50\%}$

Using the full clinical proton beam line, the proton ranges were simulated over a range of MEE values in a water phantom. Table 4.2 summarizes the simulated proton ranges for different MEE values (assuming an initial proton energy of 199.78 MeV at the vacuum tube and 188.6 MeV at the target). The calculated ranges were then compared to the measured proton range of 240.1 mm. Yet, a comparison between the simulated result ($^{75}R_{50\%}$) and the measured result ($^{m}R_{50\%}$) shows that these values line up closer to 86 eV. This can also be shown in Figure 4.22(a), where the full simulated depth dose profiles for the different MEE values are plotted. It can be clearly seen that the simulated profiles differ largely from the measurement. Figure 4.22(b) shows the correlation between the simulated range values ($^{75}R_{50\%}$) and the MEE values. As shown in Figure 4.22(b), the appropriate MEE value to produce a 24 cm range (with a 199.78

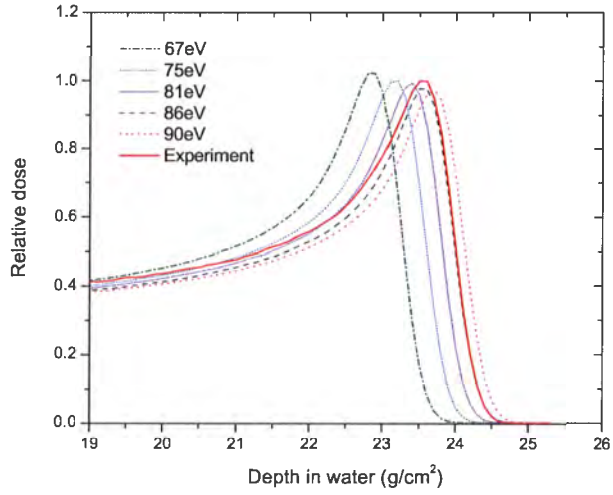

Figure 4.22: *(a) Depth dose (Bragg peak) profiles for a range of mean excitation energy of water for a 24 cm range clinical proton beam and (b) the calculated range as a function of the mean excitation energy of water.*

MeV starting proton energy) would be 85.9 eV. This MEE value falls well outside of the expected range of values discussed above, so instead of changing from the ICRU-recommended MEE value of 75 eV, the decision was made to change the energy of the incident protons entering the beam line. After further investigation, it was observed that protons starting with an initial energy of 199.78 MeV lost significant energy along the beam line in both the scatterers as well as the energy degrader. The mean proton energy exiting the final patient collimator and reaching the target was measured to be 188.6 MeV or producing an equivalent range of 23.6 cm (0.4% lower than the expected value of 24 cm). The incident proton energy was adjusted until the appropriate 24.0 cm range was achieved at the isocenter, resulting in an upward adjustment of 1.58 MeV to a corrected beam energy of 201.36 MeV.

Table 4.3: *A summary of $R_{50\%}$ values corresponding to 67.2 eV, 75 eV and 81.8 eV and uncertainties of range measurements in mm using the modified beam energy of 201.36 MeV.*

$R_{50\%}$ (mm)	$^{67.2}R_{50\%}$ (mm)	$^{75}R_{50\%}$ (mm)	$^{81.8}R_{50\%}$ (mm)	Δ (mm)	Δ(%)	$\Delta R_{50\%}$ (mm)
240	236.43	239.99	242.19	5.76	2.40	0.01
147.5	145.66	147.65	149.23	3.57	2.42	0.15
97.0	95.88	97.16	98.21	2.33	2.40	0.16
48.2	47.61	48.25	48.76	1.15	2.43	0.05

$\Delta R_{50\%}$: difference between measured ($R_{50\%}$) and simulated ($^{75}R_{50\%}$) range
Δ : $^{81.8}R_{50\%}$ - $^{67.2}R_{50\%}$
Δ(%) : (Δ/$^{75}R_{50\%}$)*100

Finally, the simulations were repeated with the modified beam energy (201.36 MeV) for different proton ranges: 24, 14.75, 9.7, and 4.82 cm. Table 4.3 summarizes the range uncertainty for different proton ranges. Our study also conformed the range uncertainty related to the difference in the I-values between 67.2 and 81.8 eV of this range (out of this selected range, the range values differ largely, and are not considered for the evaluation). The ranges were determined at the 50% distal falloff position of the Bragg peak. A consistent uncertainty up to 2.4% was calculated for MEE value between 67.2 and 81.8 eV when the proton range is decreased from 240 mm down to 48.2 mm.

4.2.3 Validation of the newly designed range monitor

Figure 4.23 illustrates the distribution of the energy deposited by a 24-cm range proton beam in the model. Protons travelling through the occluding rod are completely stopped in order to produce an uniform lateral dose distribution. The comparison between simulated and measured charge collection values in the range monitor for proton ranges of 24, 10.3 and 5.03 cm in water are shown in Figures 4.24-4.26. The simulated proton range was measured at the 50% falloff distance of the Bragg peak. The simulations were done with 10^8 proton histories. The vertical scale in the figure, charge deposit in pC, is normalized to the EM peak. The horizontal scale indicates the number of the Cu plate (or the channel). The simulation results showed good agreement with the experimental measurement and also confirmed the accuracy of the newly designed range monitor.

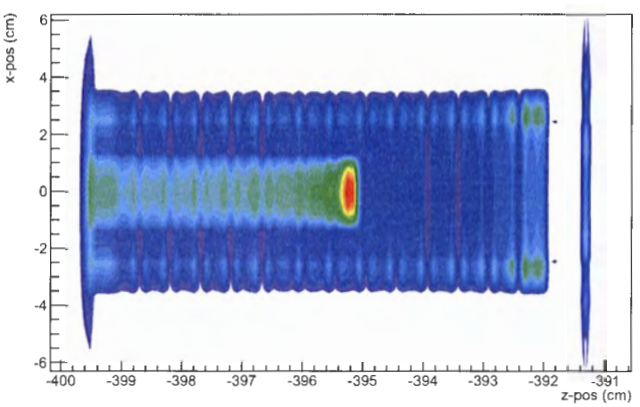

Figure 4.23: *Distribution of energy deposited by a 24 cm range proton beam within the range monitor.*

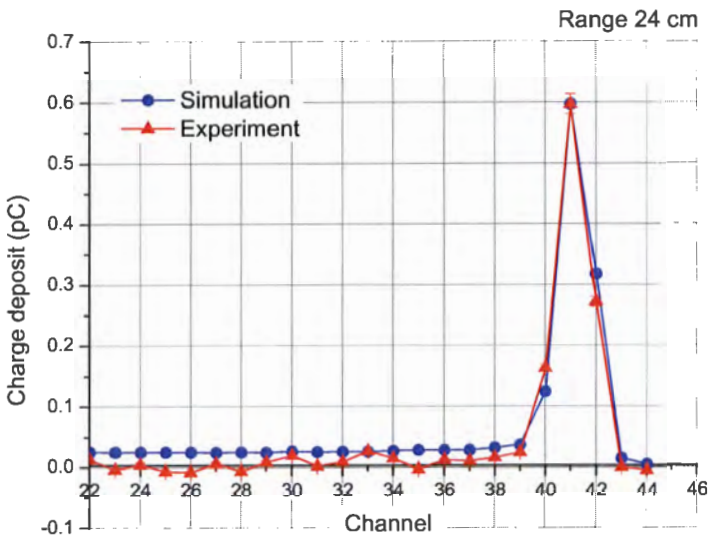

Figure 4.24: *Comparison of measured and simulated charge deposition on the Cu plates for 24 cm range protons in water.*

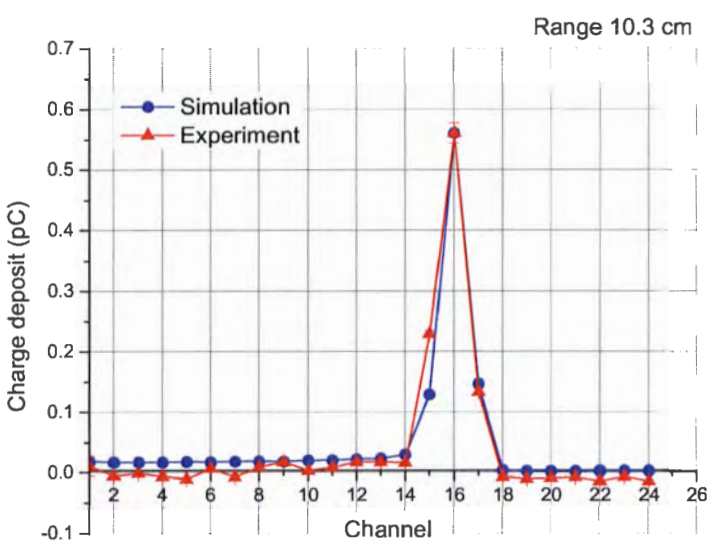

Figure 4.25: *Comparison of measured and simulated charge deposition on the Cu plates for 10.3-cm range protons in water.*

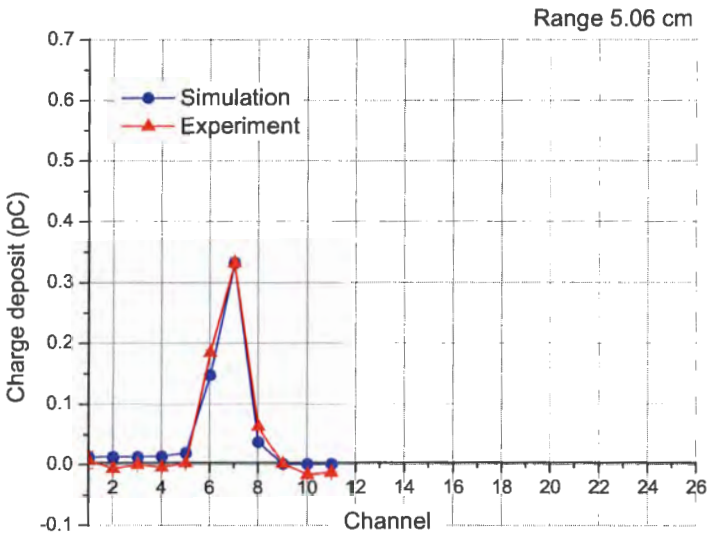

Figure 4.26: *Comparison of measured and simulated charge deposition on the Cu plates for 5.06-cm range protons in water.*

4.3 Determination of detector response functions (DRFs)

Seven standard gamma emitting sources and an $^{241}AmBe$ neutron source were used for the detector resolution calibration in the energy range of 0.661 to 4.438 MeV. Table 4.4 summarizes the detector resolution values obtained by direct measurement of FWHM from the energy spectra acquired by the NaI and $LaBr_3$ detectors. The resolution of the $LaBr_3$ detector was about 3.0% at 0.611 MeV and 2.5% at 4.438 MeV. The user defined Gaussian parameters x and y (see Equation 2.13) for each detector listed in Table 4.5 were estimated from the experimental data using a least square fit as seen in Figure 4.27. These fits show the uniqueness of the individual detectors. In our Monte Carlo detector model, Gaussian broadening is applied at the end of each event after summing all gamma energy deposited at the detector active volume.

Table 4.4: *Energy resolution of NaI 2"x2", NaI 3"x3" and $LaBr_3$ 2"x2" detectors.*

		NaI 2"x2"		NaI 3"x3"		$LaBr_3$ 2"x2"	
	E_γ	FWHM	Resolution	FWHM	Resolution	FWHM	Resolution
Isotopes	(MeV)	(MeV)	R(%)	(MeV)	R(%)	(MeV)	R(%)
^{133}Ba	0.356	0.032	8.99	0.033	9.27		
^{22}Na	0.511	0.038	7.44	0.042	8.22	0.019	3.72
^{137}Cs	0.611	0.043	6.51	0.051	7.72	0.020	3.03
^{54}Mn	0.835	0.049	5.87	0.056	6.71	0.024	2.87
^{60}Co	1.170	0.056	4.79	0.064	5.47	0.028	2.39
^{22}Na	1.277	0.061	4.78	0.067	5.25	0.029	2.27
^{60}Co	1.330	0.062	4.66	0.068	5.11	0.029	2.18
$^{241}AmBe$	4.438	0.149	3.36	0.161	3.63	0.109	2.46

Table 4.5: *Gaussian broadening parameters for NaI and $LaBr_3$ detectors.*

	x	y
NaI (2" x 2")	0.02347	0.6033
NaI (3" x 3")	0.02604	0.6045
$LaBr_3$	0.01156	0.8211

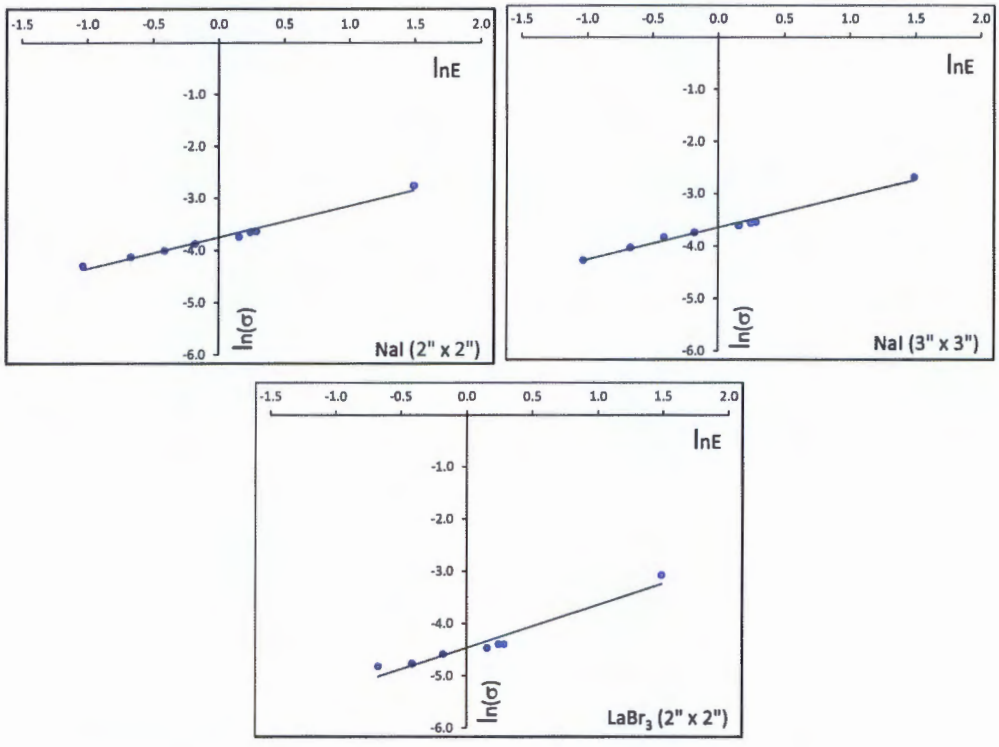

Figure 4.27: *Fitting the Gaussian broadening parameter for (a) the 2" x 2" NaI (b) the 3" x 3" NaI and (c) the 2" x 2" $LaBr_3$ detectors.*

The Geant4 generated detector response was then validated against experimental results. The comparison between the Geant4-generated energy spectra of ^{60}Co, ^{22}Na and ^{241}AmBe and experimentally measured energy spectra for NaI (2" x 2"), NaI (3" x 3") and $LaBr_3$ (2" x 2") detectors are illustrated in Figures 4.28, 4.29 and 4.30. All the spectra have been normalised to their (highest) photo-peaks. The Geant4 generated detector responses agree well with experimental results in the photo peak and Compton edge energy regions. The differences in the lower energy region could be due to the contribution of scattered gamma rays from surrounding objects that were not modelled in the simulation. This difference is significantly more in the ^{241}AmBe spectra due to the additional gamma-rays induced in the objects by the neutrons emitted from the ^{241}AmBe source.

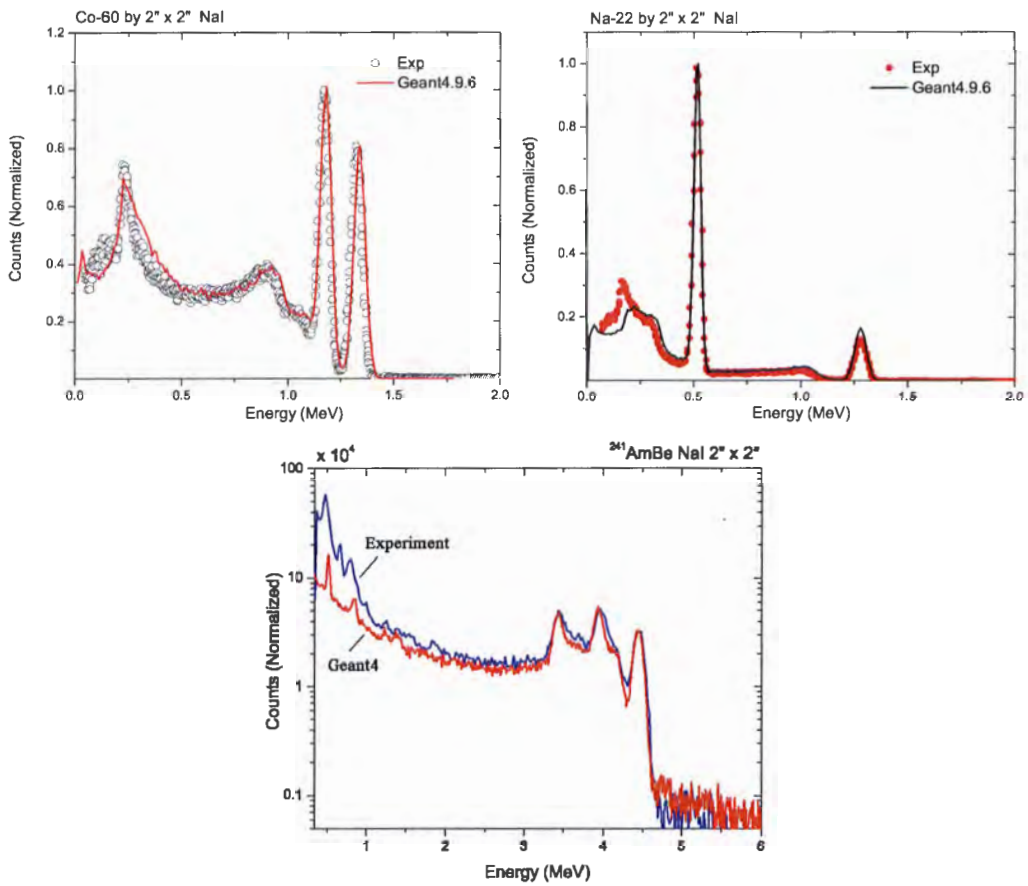

Figure 4.28: *Comparisons between experiment and simulation for 2" x 2" NaI detector.*

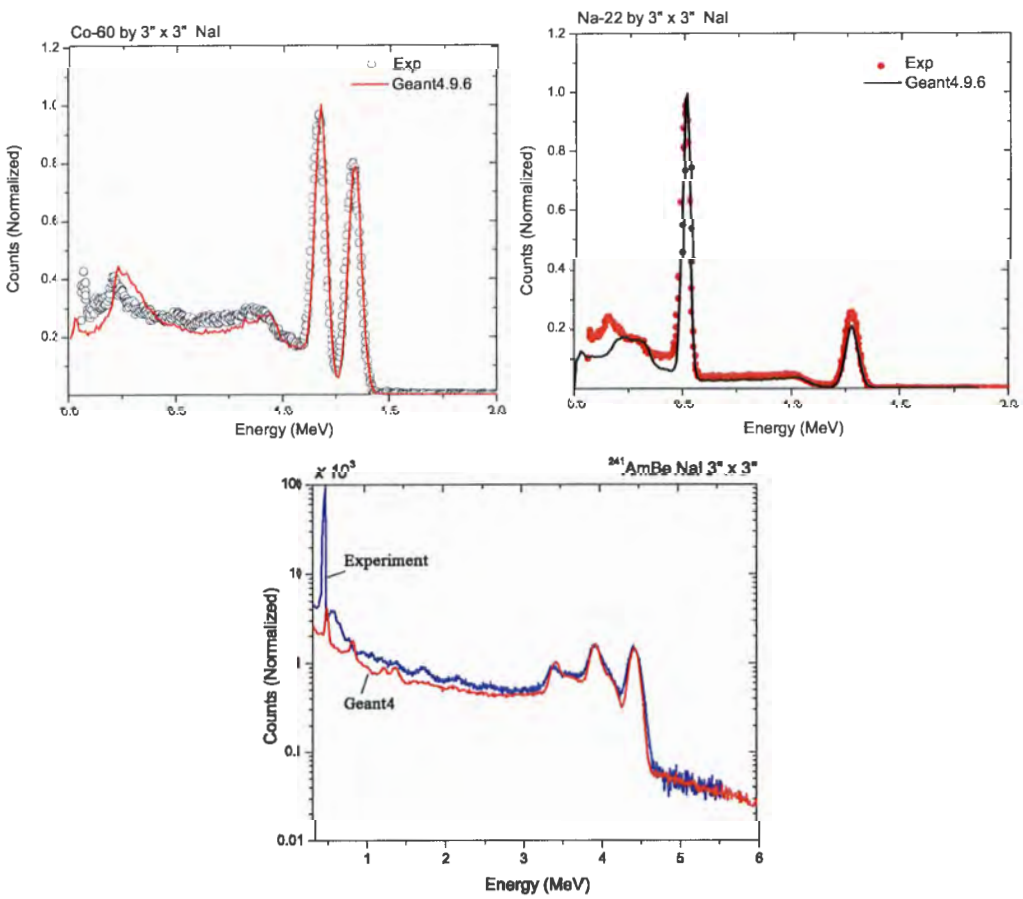

Figure 4.29: *Comparisons between experiment and simulation for 3" x 3" NaI detector.*

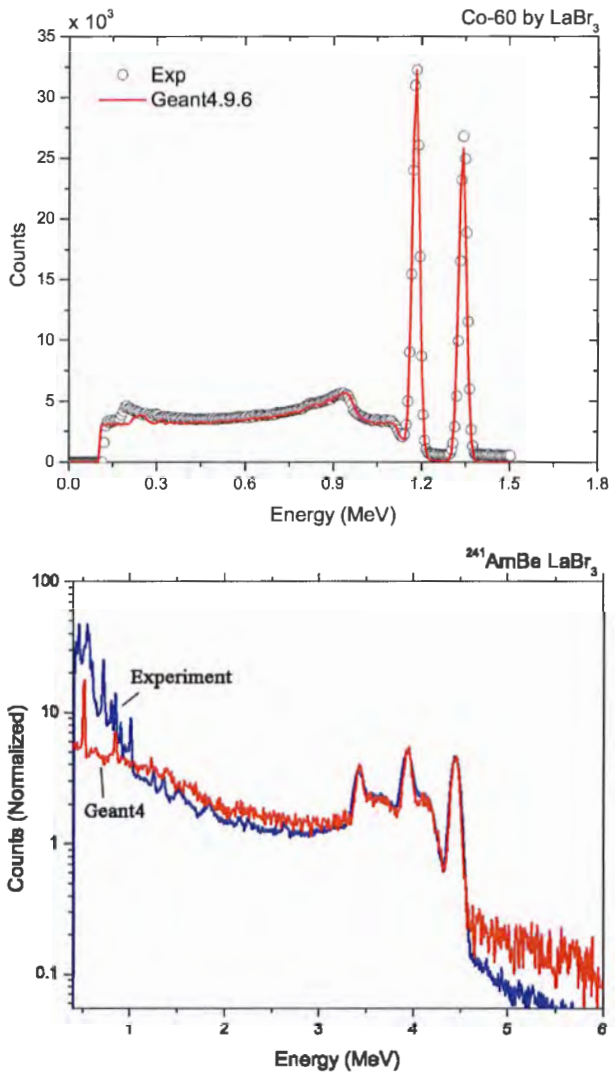

Figure 4.30: *Comparisons between experiment and simulation for 2" x 2" $LaBr_3$ detector.*

4.4 Geant4 simulation for prompt gamma detection

4.4.1 Simulation using proton pencil beam

Recently, it has been proven experimentally that the use of time-of-flight (TOF) windowing technique can improve the signal-to-background ratio in the prompt gamma spectra acquired by a pulsed proton pencil beam (Verburg et al. (2013)). A simulated TOF spectrum from gamma-rays and neutrons (produced by a 200 MeV proton pencil beam hitting a water target) impinging on a $LaBr_3$ detector is shown in Figure 4.31. It can be seen that the time-of-flight for the prompt gamma-rays emitted from the water target is comparably shorter than time-of-flight of the secondary neutrons. This difference in timing can be used as an advantage by selecting an appropriate TOF window and thus, rejecting all the late-arriving secondary neutrons and gamma rays (created primarily by neutrons hitting objects surrounding the detector).

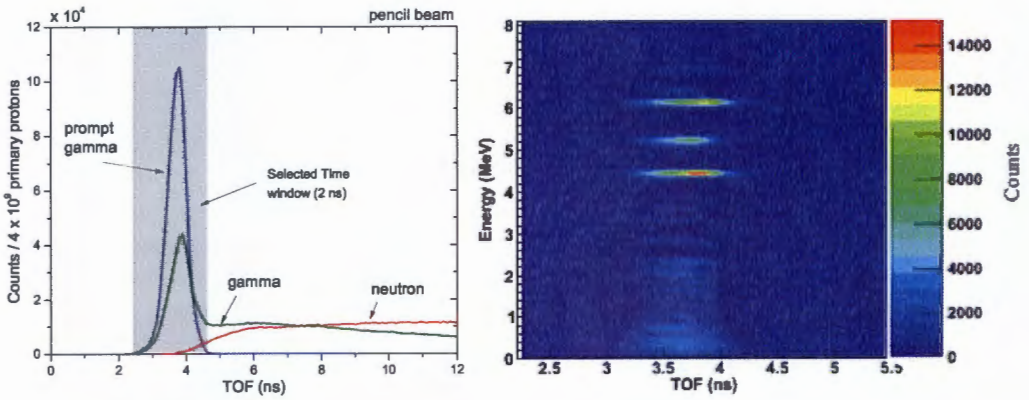

Figure 4.31: *(a) Time-of-flight spectra of particles and (b) Time-energy spectrum of prompt gammas striking the $LaBr_3$ detector.*

As illustrated in Figure 4.31, the selected TOF window of 2 ns (gray shaded area) would reduce the neutron background by 99% and the scattered gamma-rays by 60% compared to the full simulated spectra. Moreover, the TOF window can also be coupled with an energy window selection (2-7 MeV have been selected) that removes an additional 80% of the low energy scattered gamma-rays and background neutrons but does not suppress the incomplete energy deposition of Compton scattered gamma rays within the detector. Overall, there is a 90% overall background reduction achieved by using both the TOF and energy windows. Figure 4.32 shows the prompt gamma emission

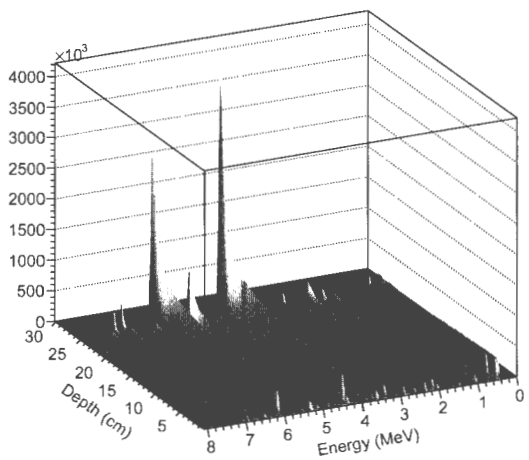

Figure 4.32: *Prompt gamma spectrum created in a water phantom as a function of depth and energy. Simulation performed with a 200 MeV pencil beam of 4 x 10^9 protons.*

spectrum from a water phantom as a function of energy and depth. The simulation was performed with 4 x 10^9 protons. Quantitatively, the most prominent prompt gamma peaks appear at 6.13 MeV from the $^{16}O(p,p\prime)^{16}O^*$ reaction and at 4.44 MeV from the $^{16}O(p,p\prime\alpha)^{12}C^*$ reaction. The third most prominent peak observed at 5.25 MeV is the result of the mixed 5.27 MeV ($^{16}O(p,px)^{15}N^*$), 5.24 MeV ($^{16}O(p,px)^{15}O^*$) and 5.18 MeV ($^{16}O(p,px)^{15}O^*$) peaks. There are also visible Oxygen peaks at 6.96 MeV and 7.11 MeV.

Figure 4.33(a) shows the Monte Carlo prompt gamma energy spectrum obtained from the $LaBr_3$ detector using both TOF (2 ns) and BGO shielding techniques. As seen in Figure 4.33(b), the BGO background subtraction reduces not only background radiation but also both the single and double escape peaks. Since the double escape peaks have been almost completely removed from the spectrum, the 5.25 MeV peak can be easily discerned from the background. Figure 4.34 shows a comparison between the energy spectra acquired with BGO active detector shielding and the combination of the BGO detector shielding and the TOF window. The similarity between the spectra in the energy window 3 - 7 MeV is due to the low number of neutrons reaching the detector in that energy range; most of neutrons fall below 3 MeV. This clearly indicates that the presence of BGO active shielding will minimize the necessity of a TOF window in the energy range above 3 MeV due to the relatively low energy of the secondary neutrons.

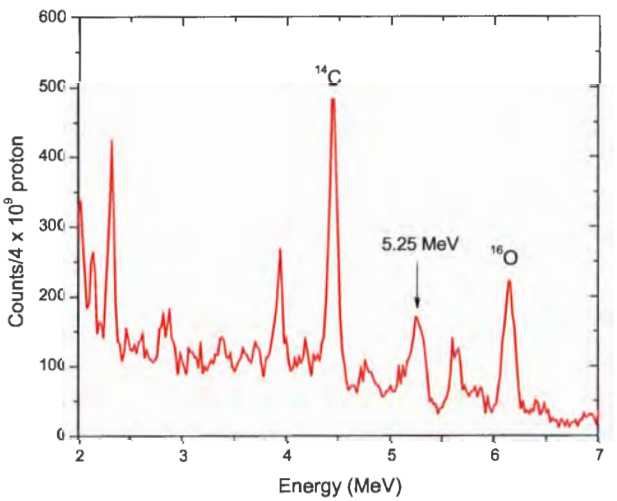

(a)

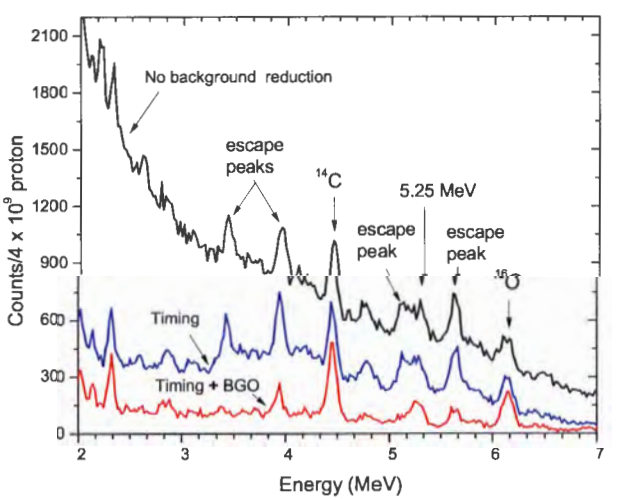

(b)

Figure 4.33: *(a) Monte Carlo prompt gamma spectrum combining both the TOF window (2 ns) and BGO active shielding. (b) Comparison of energy spectra with and without background reduction. Simulations were performed with 200 MeV pencil beam and 4 x 10^9 protons.*

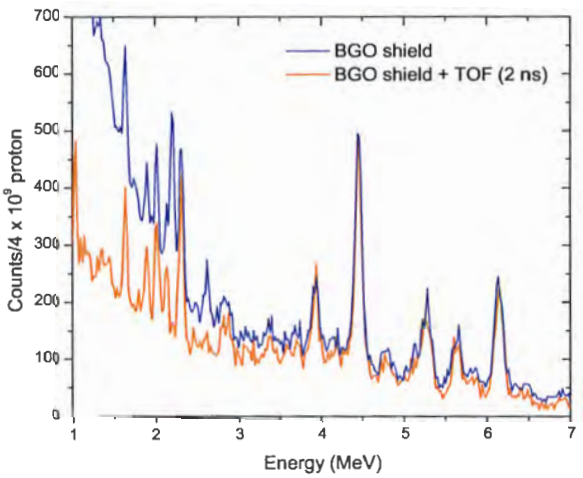

Figure 4.34: *The prompt gamma energy spectra using BGO active detector shielding compared to the combination of the BGO detector shielding and the TOF window.*

4.4.2 Simulation using passive-scatter proton beam

The Monte Carlo time of flight (TOF) spectra from the passive-scatter proton beam hitting a water target is shown in Figure 4.35(a). The corresponding TOF vs. prompt gamma energy plot is shown in Figure 4.35(b). The time of flight for the prompt gamma rays (peak 3) is shorter than the neutrons (peaks beyond 48 ns) and greater than the scattered secondary gamma rays generated in the passive beam line elements (peak 1) and in the final patient collimator (peak 2). Therefore, a TOF window of 1.8 ns (gray shaded area) would filter out the late-arriving neutrons (about 99%) from target as well as the early-arriving background gamma rays.

Figure 4.36 shows a comparison of the energy spectra simulated with and without the background reduction techniques applied. The simulation was carried out with 2.5 x 10^{10} incident protons entering the passive-scatter beam line. Only 8% of these starting protons travel the length of the beam line and reach the target; the remaining protons are stopped in the beamline elements or in the final collimator. These results indicate that the use of both timing and active shielding is able to remove up to 90% of the background radiation which includes a 10% reduction by BGO subtraction as shown in Figure 4.37(a). Peaks at 6.13, 4.44 and 5.25 MeV from $^{16}O^{*}$, $^{12}C^{*}$ and $^{15}O^{*}$ respectively can be clearly identified once both timing and BGO subtraction is included. Subtraction of the Compton-scattered background is required to resolve the 5.24 MeV peak from

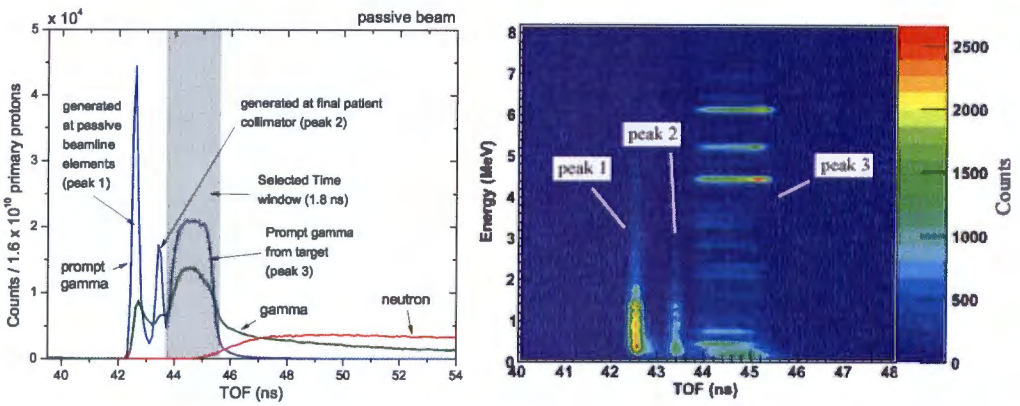

Figure 4.35: *(a) Simulated TOF spectra from the passive-scatter proton beam and (b) Time vs energy spectrum of the prompt gammas detected by the $LaBr_3$ detector.*

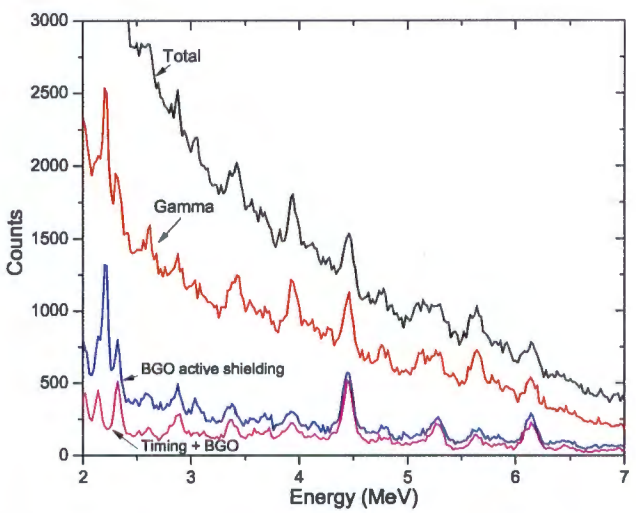

Figure 4.36: *Comparison of energy spectra with and without background reduction methods.*

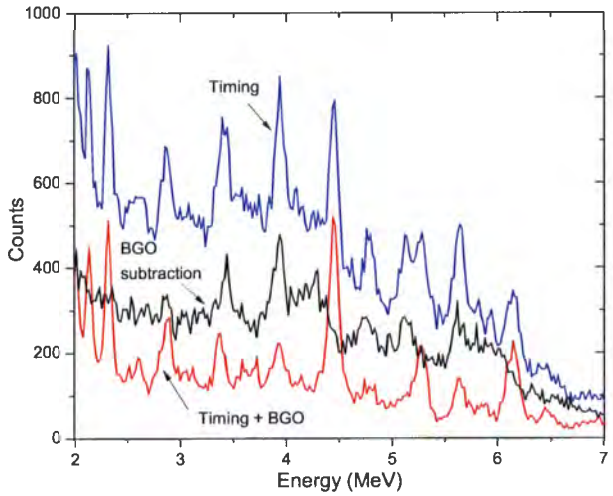

(a)

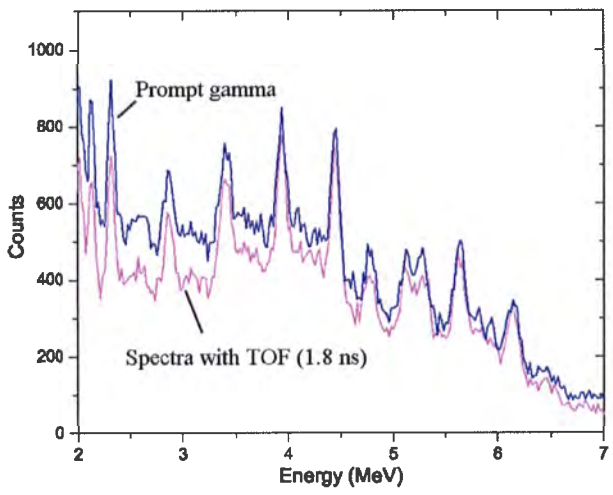

(b)

Figure 4.37: *Comparison (a) of energy spectra with TOF window (with and without BGO active shielding) of 1.8 ns and (b) between simulated prompt gamma production from the target and simulated spectra in the detector with timing.*

the second escape peak of 6.13 MeV. The comparison between the spectra of known prompt gammas (produced in the target) hitting the detector and the total gamma spectra with the TOF window activated as shown in Figure 4.37(b) is promising with 72.4% of detected gammas being prompt gammas. However, the estimated detector efficiency of the prompt gamma in the energy range of 3-7 MeV was 0.1% (0.35% in the energy range of 0-10 MeV). The efficiency was defined as the ratio of the total number of prompt gammas registered in the detector to the number of prompt gammas emitted from the target. Overall, based on the comparisons with prompt gamma cross-sections data and the rigorous model calibrations, the developed Monte Carlo model provides a good foundation on which to commence comparisons to experimental prompt gamma measurements.

Chapter 5

Measurements of prompt gamma production from a passive-scatter proton therapy beam line

This is the second analysis chapter which contains results of all the experimental work described in Chapter 3. The primary aim of the work presented in this chapter to learn more about the discrete prompt gammas emitted from tissue in the passive-scatter proton therapy environment. These are the first prompt gamma measurements using a clinical passive-scatter proton treatment beam, performed using water, Perspex, carbon and liquid-nitrogen targets. The discrete prompt gamma emissions from the ^{16}O, ^{12}C and ^{14}N were measured as well as the prompt gamma emissions at various depths within the water and Perspex targets. Finally, all the measurements were compared to Geant4-simulated results of the prompt gamma production from the Monte Carlo passive-scatter beam line.

5.1 Prompt gamma measurements with target at isocentre

In passive-scatter proton irradiation, the continual presence of background noise from the beam line elements and the final collimator are a challenge to the detection of prompt gammas. Therefore, for these measurements, a subtraction of the background spectrum with no phantom present in the beam line from the measured spectrum was required for each measurement. Each prompt gamma emission spectrum was measured using the iThemba LABS passive-scatter beam with proton energy corresponding to a 24 cm proton range in water. The prompt gamma spectrum measured during irradiation of the carbon target is shown in Figure 5.1. The acquisition time was 600 s. In the spectra, a photo peak at 4.44 MeV and its first and second escape peaks at 3.93 and 3.42 MeV are clearly visible. Figure 5.2 shows the measured energy spectra from the irradiation of the water phantom with an acquisition time of 1200 s. It is possible to identify the 6.13 MeV prompt gamma peak and the peaks at 5.61 and 5.11 MeV are the first and second escape peaks, respectively. In addition, a peak at 2.22 MeV was observed that was caused by neutrons captured by ^{1}H. Unfortunately, the expected prompt gamma peak at 4.44 MeV from the excited state of $^{12}C^{*}$ was not identified clearly and only observed with a very weak intensity. However, it could be concluded from this experiment that the prompt gamma emission from the excited state of $^{16}O^{*}$ is dominant in the proton-induced reactions on ^{16}O.

The measurement was repeated with 16-cm range protons in water (about 150 MeV) as shown in Figure 5.3. With an acquisition time of 600 s, the identified peaks are similar but sharper than the peaks observed in the 24-cm range proton beam irradiation. This is due to a smaller amount of secondary radiation produced by the lower-energy proton-induced nuclear reactions. For all of the measurements performed at the isocentre, the high amount of background radiation made it difficult to identify the prompt gamma peaks. A second set of measurements was then scheduled in order to try and obtain more defined prompt gamma peaks by reducing the impact of the background.

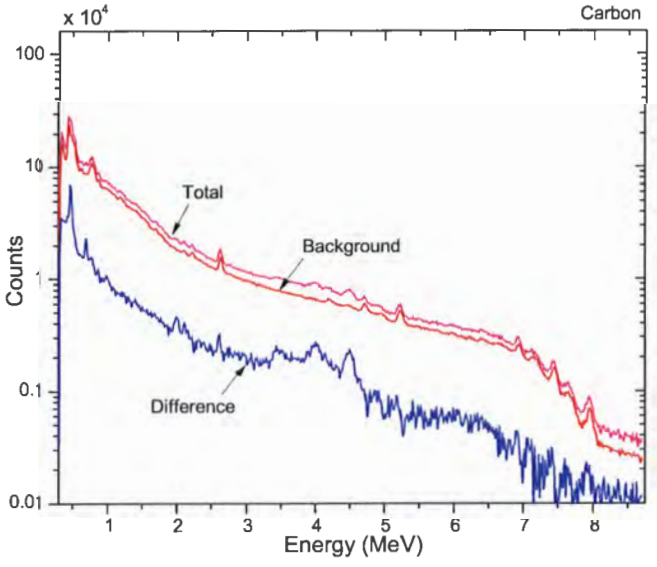

Figure 5.1: *Prompt gamma energy spectra measured from a carbon target for protons with energy corresponding to a 24-cm range in water obtained with LaBr3 detector.*

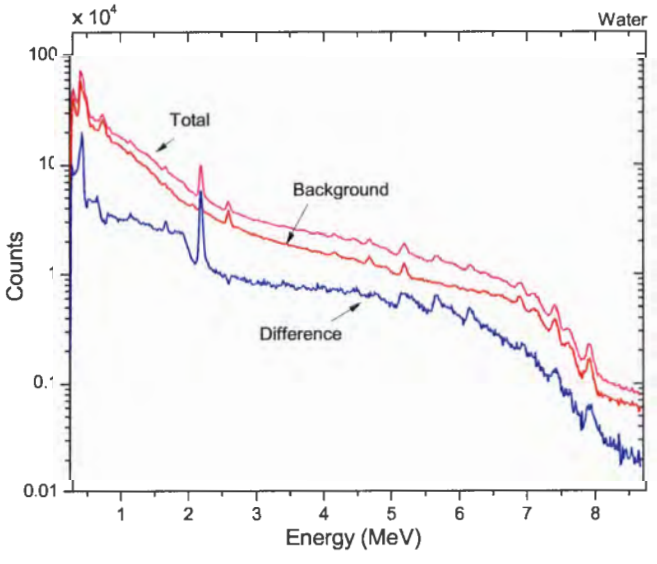

Figure 5.2: *Prompt gamma energy spectra measured from a water target for protons with energy corresponding to a 24-cm range in water obtained with LaBr3 detector.*

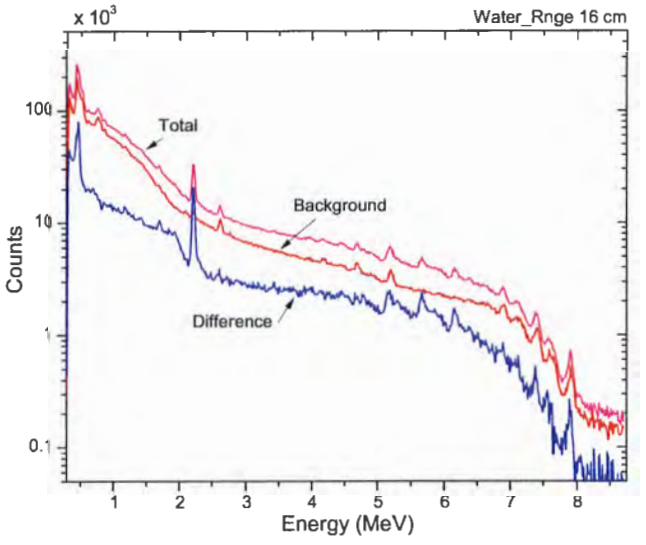

Figure 5.3: *Prompt gamma energy spectra measured a water target for protons with energy corresponding to a 16-cm range in water obtained with LaBr3 detector.*

5.2 Prompt gamma measurements with target 170 cm from isocentre

The primary modification for the second set of prompt gamma measurements was the addition of the timing electronics in order to be able to create a short time window to exclude both the secondary gammas and background neutrons as described in Section 4.4.2. Figure 5.4 shows the two-dimensional time-energy density histogram measured using the $LaBr_3$ detector with a 24-cm range proton beam on the water target. In the spectra the prompt gamma line at 6.13 MeV, as well as the first and second escape peaks for the 6.13 MeV gamma are visible, while the 4.44 MeV gamma line cannot be resolved from the background noise. Unfortunately, these gamma lines can be seen along the entire length of the selected time window and thus reveal that these gammas are being produced throughout the entirety of the 38.5 ns RF pulse. Unlike Figure 4.35(b), where a clear narrow time peak is shown, there are no peaks shown in our time-energy histogram, thus making it impossible to implement a time window. As a result, the prompt gamma spectra results shown in this work do not rely on the time-of-flight coincidence measurements instead simply use the pulse height spectra. This issue will be further investigated in order to improve time-of-flight detection in the future.

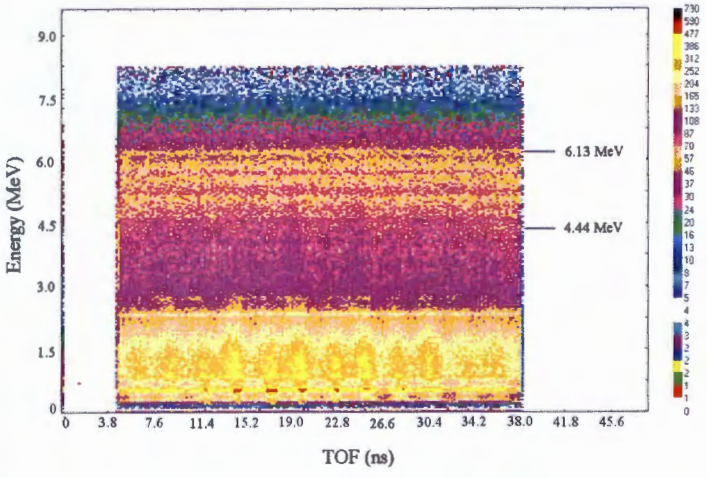

Figure 5.4: *Time-energy spectrum measured at the Bragg peak. Measurements were performed for a proton beam with a 24 cm range on a water target.*

Figures 5.5 - 5.8 show the prompt gamma spectra from the water, Perspex, carbon and liquid nitrogen targets, respectively. Background spectrum were taken with no phantom present in the beam line. In the spectra from the water phantom shown in Figure 5.5 the prompt gamma-ray emission from ^{16}O (6.13 MeV) is prominent and 5% higher than the emission from ^{12}C(4.44 MeV). Also, the prompt gamma emission from ^{12}C is clearly seen in the spectra from the plastic phantom as shown in Figure 5.6. The second most prominent peaks are from ^{16}O. In Figure 5.7, the peak at 4.44 MeV can be identified as the only predominant emission in the prompt gamma energy spectra emitted from the carbon target. The peaks at 3.92 MeV and 3.42 MeV are clearly visible and are the first and second escape peaks of the 4.44 MeV gamma. In Figure 5.8 we show the prompt gamma emission spectra from the liquid nitrogen target. The expected 2.313 MeV peak is identified but other important peaks at 0.728, 1.635, 2.793, and 5.106 MeV could not be resolved. In addition, a strong peak at 4.44 MeV from ^{12}C can be seen in the measured spectra as a result of the Styrofoam box that contained the liquid nitrogen. The expected peaks at 3.378 and 3.890 MeV also cannot be resolved due to the presence of the first and second escape peaks of the 4.44 MeV gamma at 3.92 MeV and 3.42 MeV, respectively. Note that the 2.22 MeV peak caused by the absorption of secondary thermal neutron by ^{1}H (Smeets et al. (2012)) can be seen in both the water (see Figure 5.5) and Perspex (see Figure 5.6) spectra. Also it is quite easy to see an unidentified peak at 2.62 MeV in all the spectra,including the background spectrum.

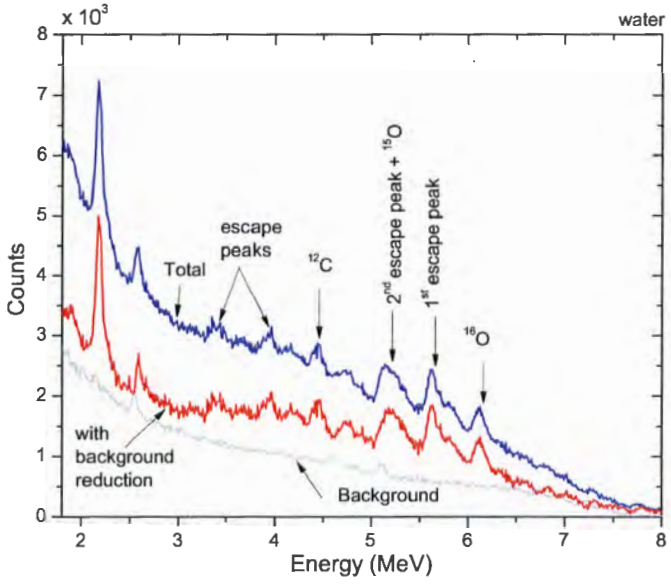

Figure 5.5: *Detected prompt gamma energy spectra emitted from a water target for protons with energy corresponding to a 24-cm range in water.*

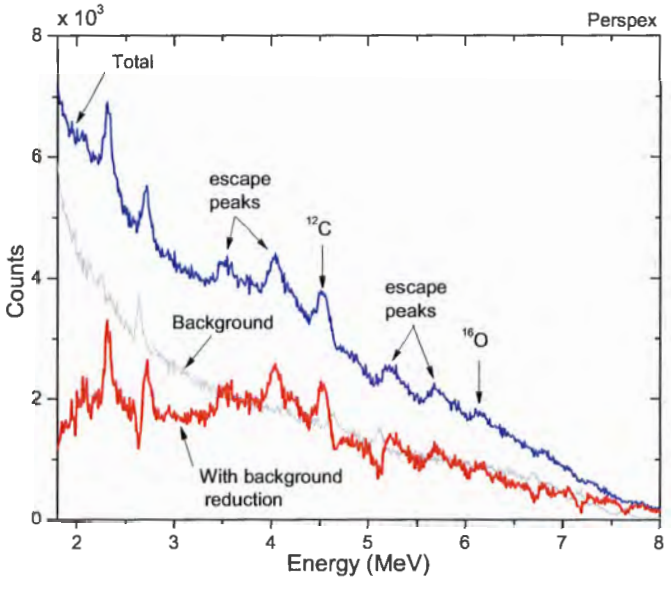

Figure 5.6: *Detected prompt gamma energy spectra emitted from a perspex target for protons with energy corresponding to a 24-cm range in water.*

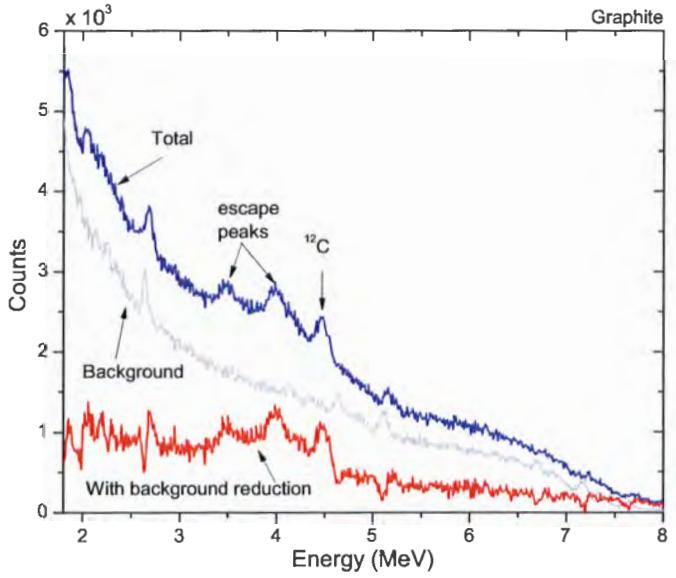

Figure 5.7: *Detected prompt gamma energy spectra emitted from a carbon target for protons with energy corresponding to a 24-cm range in water.*

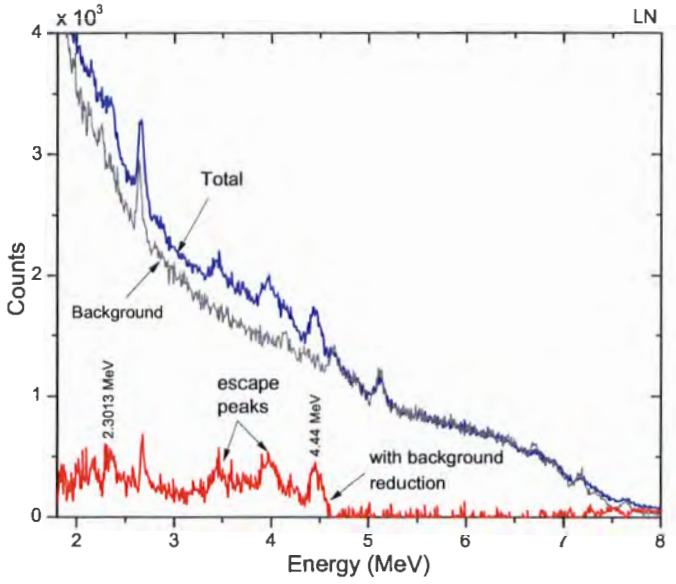

Figure 5.8: *Detected prompt gamma energy spectra emitted from a liquid nitrogen target for protons with energy corresponding to a 24-cm range in water.*

5.2.1 Measurement of prompt gamma emission along the beam path

For the series of prompt gamma measurements at various depths in water and Perspex, the two energy peaks (4.44 MeV and 6.13 MeV) plus a larger energy window (3 - 7 MeV) was used to help identifing the response of the prompt gamma production with depth. The two energy peaks are obviously connected to the prompt gamma production; the 3 - 7 MeV energy window is used because it provides a "total" prompt gamma count which includes the energy peaks, and their escape peaks, while excluding the large number of low-energy gammas. Using the method described in Section 3.3.2, the number of prompt gammas in the three energy bins was calculated and the results are shown in Figures 5.9 and 5.10. The Bragg peak is shown for reference.

From Figure 5.9, it can be seen that the number of discrete 4.44 MeV and 6.13 MeV prompt gammas produced in the water target are nearly equal (the 4.44 MeV emission is actually 15% greater than the 6.13 MeV emission near the Bragg peak). As expected, the maximum peak position is observed at 22.5 cm depth (1 cm before the Bragg peak). This is due to the partial (prompt) gamma production cross-section which has its maximum value at a proton energy of 13 MeV for the 6.13 MeV line and at 23 MeV for the 4.44 MeV emission (Kiener et al. (1998)). So the maximum prompt gamma production would be expected to occur before the protons completely run out of energy. In contrast, the 4.44 MeV emission from the Perspex target (see Figure 5.10) is considerably larger (by a factor of 1.5) than the 6.13 MeV emission. This is naturally due to the atomic concentration of Perspex (30% - ^{16}O and 60% - ^{12}C) and the resulting stronger contribution to the 4.44 MeV prompt gamma emission. The 4.44 MeV peak of ^{12}C is seen at a proton energy of around 20 MeV (0.5 cm from the Bragg peak). The "total" energy-integrated prompt gamma profiles are also shown and for both targets, the 3 - 7 MeV depth data peaks earlier than for the discrete energy peaks. For the water target, the 3 - 7 MeV results peaks at 20 cm (3.5 cm before the Bragg peak) and for the Perspex target, the 3 - 7 MeV results peak at 17.5 cm (3.4 cm before the Bragg peak). The 3 - 7 MeV depth profiles are also flatter than the 4.44 and 6.13 MeV results and better reflect the expected total gamma production based on the non-elastic cross-section data shown in Figure 4.2.

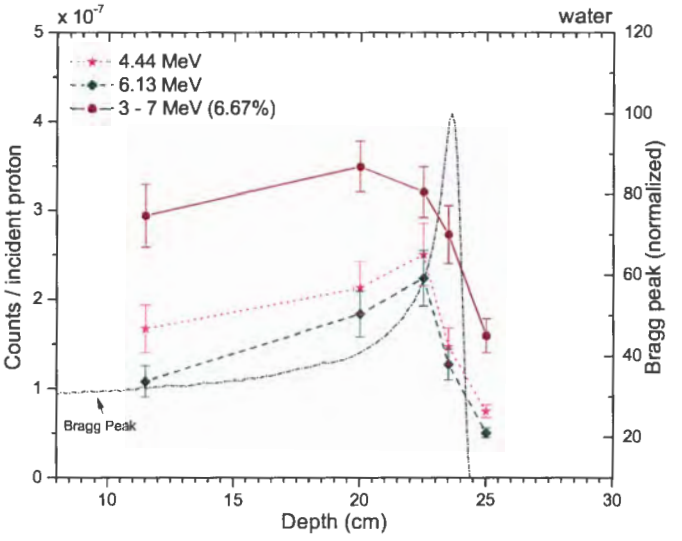

Figure 5.9: *Discrete prompt gamma (4.44 MeV peak, 6.13 MeV peak and total gamma count over 3 - 7 MeV energy range) emission per incident proton emitted from a water target using a 24 cm range clinical passive-scatter proton beam. The 3 - 7 MeV gamma count has been scaled to 6.67% of its total value for display purposes.*

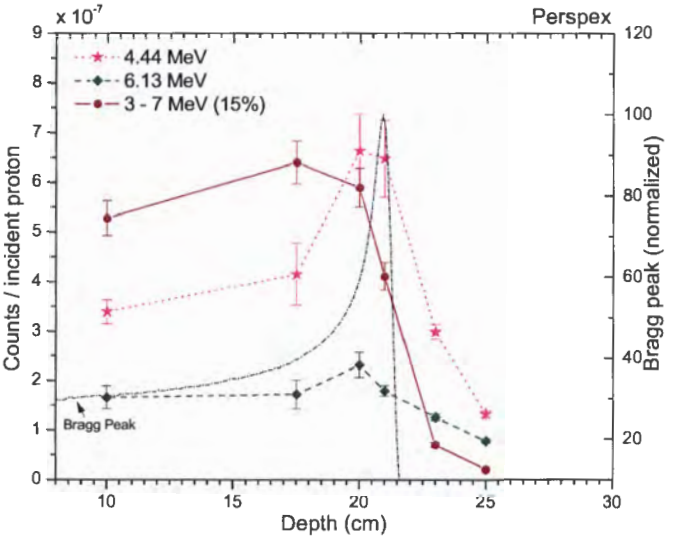

Figure 5.10: *Discrete prompt gamma (4.44 MeV peak, 6.13 MeV peak and total gamma count over 3 - 7 MeV energy range) emission per incident proton emitted from a Perspex target using a 24 cm range clinical passive-scatter proton beam. The 3 - 7 MeV gamma count has been scaled to 15% of its total value for display purposes.*

5.3 Relative comparison of prompt gamma measurements to Monte Carlo simulations

The experimental set-up was modelled by Geant4 Monte Carlo code in order to reproduce the experiments for comparisons. In this section, we focus on relative comparison between simulations and experiments due to the lack of absolute data taken for the first set of measurements. The purpose of this comparison is to quantify the discrete prompt gamma-ray emission in the interested energy range of 3 - 7 MeV. Moreover, the relative comparison helps to verify the shape of the prompt gamma emission and to compare the number of prompt gammas in each of the peaks. The absolute comparisons for the second set of data are presented in Section 5.4.

5.3.1 Comparison of measured and simulated prompt gamma productions at isocentre

Figures 5.11 and 5.12 illustrate the comparison of the prompt gamma energy spectra from the experimental results discussed in Section 5.1 and the corresponding simulation of the experimental set-up for the carbon (Figure 5.11) and water (Figure 5.12) targets. Each simulation was performed with 2.5 x 10^{10} primary protons, but then the simulated results were scaled by a scaling factor (exact factor values shown in figure captions) in order to line up the prompt gamma peaks. For the carbon irradiation the 4.44 MeV peak and the two escape peaks can be seen in both the measured and simulated spectra, with a roughly equivalent size and shape for each one. Whereas for the water target (Figure 5.12), the peak at 6.13 MeV, as well as its first and second escape peaks, are clearly visible in both spectra, but the peak at 4.44 MeV (and its escape peaks) is not evident in the experimental spectra (only a weak signal) while these peaks are clearly seen in the simulated results. The missing 4.44 MeV peaks in the experimental spectra highlight the presence of a high-level of background radiation from the passive-scatter beam line and precipitated the need for further measurements as previously discussed. The results from these additional measurements are discussed in the following sections.

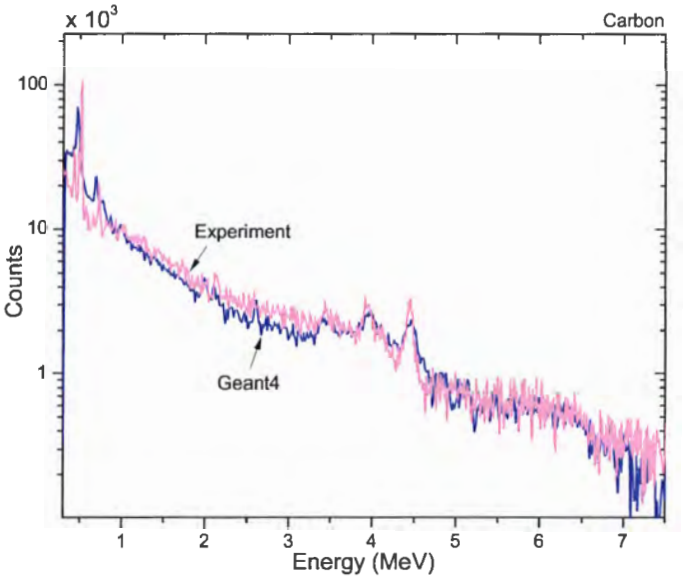

Figure 5.11: *Comparison between measured and simulated energy spectra from carbon target. The simulated spectrum is multiplied by a factor 6.8 for comparison.*

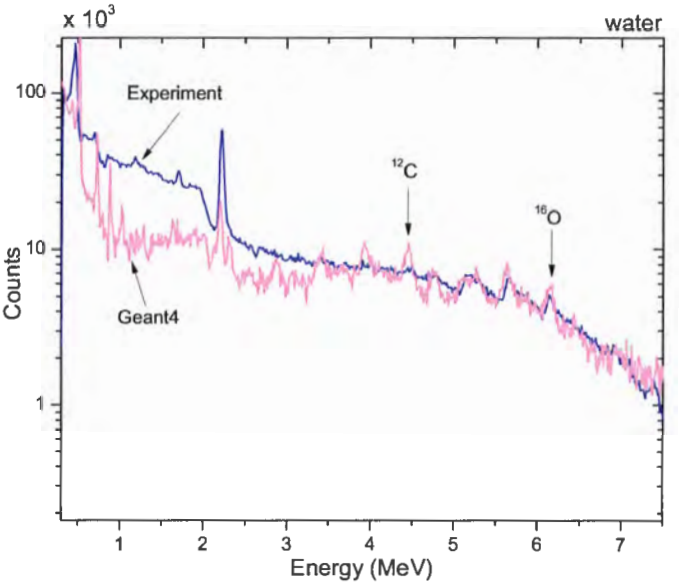

Figure 5.12: *Comparison between measured and simulated energy spectra from water target. The simulated spectrum is multiplied by a factor 13.5 for comparison.*

5.3.2 Comparison of measured and simulated prompt gamma production 170 cm from isocentre

A detailed comparison of the second set of prompt gamma measurements to simulated results for the water, Perspex and graphite (carbon) targets is shown in Figures 5.13, 5.14 and 5.15 for a 24 cm range proton beam. The simulated results used 2.3 x 10^{10} primary protons to duplicate each of the experimental measurements. The Geant4-generated energy spectra were then scaled for comparison to the measured spectra with the following scaling factor: the simulated energy spectra was multiplied by a factor of 0.85 for water, 0.8 for Perspex (shown in Figure 5.14(a)), 1.0 for Perspex (shown in Figure 5.14(b)) and 1.9 for graphite. The number of prompt gammas in the discrete energy peaks (4.44 MeV and 6.13 MeV plus their respective escape peaks) were also counted (using the baseline technique) and those values are summarized in Table 5.1. This technique was applied to both the measured and simulated energy spectra. It can be noted from Table 5.1 that the Geant4 simulation mostly underestimates the number of prompt gammas found in the peaks except for the 4.44 MeV and escape peaks emitted from the water target, where the simulated results are larger than the measured values. The liquid nitrogen target data is not included in the comparison due to the poor quality of the measured results.

In the comparison of the energy spectra from the water target (Figure 5.13), we clearly see the 6.13 MeV (from ^{16}O) and 4.44 MeV (from ^{12}C) photo peaks. In addition to the measured and the simulated total gamma energy spectra, the simulated prompt gamma spectra is included in Figure 5.13. The simulated prompt gamma spectra (dotted line) shows the fraction of the total detected gamma count that can be directly attributed to gammas produced by inelastic collisions within the target. Based on the prompt gamma counts in Table 5.1, the Geant4 simulation underestimates the 6.13 MeV peak by 14% and overestimates the 4.44 MeV prompt gamma emission from ^{12}C by 36%.

Comparisons between the experiment and the Geant4 simulation for the Perspex phantom (see Figure 5.14) were performed individually for the two total inelastic cross-section data sets of Wellisch and Axen (Figure 5.14(a)) and Tripathi et al. (1999)(Figure 5.14(b)). The experimental results in both figures are the same; the difference in the cross-section data sets only impacts the simulated results and in this case is a barely noticeable difference. The simulated prompt gamma emission corresponding to the 6.13 MeV and the 4.44 MeV photo peaks are both underestimated by 27% in the case of Wellisch and Axen and underestimated by 28% and 25%, respectively in the case of

Table 5.1: *Relative difference (S - M)/M between the Simulated (S) and Measured (M) prompt gamma counts for the 4.44 MeV and 6.13 MeV discrete prompt gamma peaks. Measurement is taken at the Bragg peak. *Simulations performed with the cross-section Tripathi et al. (1999) instead of the default Wellisch and Axen cross-section.*

		4.44 MeV			6.13 MeV			3 - 7 MeV
Target		Photo peak	1^{st} escape peak	2^{nd} escape peak	Photo peak	1^{st} escape peak	2^{nd} escape peaks	Total counts
Water	Experiment	5067	4697	3294	5606	8249	16806	140697
	Simulation	6869	7210	4394	4791	5024	8742	143160
	Difference	+0.36	+0.53	+0.33	-0.14	-0.39	-0.47	+0.02
Perspex	Experiment	12064	8941	5688	2989	4313	6120	118265
	Simulation	8780	7810	3948	2190	1843	2338	92401
	Difference	-0.27	-0.13	-0.30	-0.27	-0.57	-0.62	-0.22
	Simulation*	9032	6589	5641	2139	3804	3129	100454
	Difference*	-0.25	-0.26	-0.01	-0.28	-0.12	-0.49	-0.15
Graphite	Experiment	8991	6327	5854				56529
	Simulation	7341	5970	3086				45997
	Difference	-0.18	-0.06	-0.39				-0.18
	Simulation*	7429	4586	5538				51983
	Difference*	-0.17	-0.28	-0.05				-0.08

Tripathi et al. (1999). For the 4.44 MeV prompt gamma peak, the measured photo peak is slightly broader than that for the peak generated by Geant4, which is due to nuclear Doppler broadening being disabled in the model. The broadening present in the Geant4 spectra is due solely to the detector response function, which adequately predicts the actual shape of the spectra.

As illustrated in Figure 5.15, comparisons for the graphite phantom are also performed with both total non-elastic cross-section (see Figures 5.15(a) for Wellisch and Axen and Figures 5.15(b) for Tripathi et al. (1999)). A more noticeable difference can be seen between the simulated results in the two panes of Figure 5.15 because the difference between the two cross-section data sets is more pronounced for ^{12}C. Although from Table 5.1, this difference is actually quite small since the Geant4 simulation underestimates the 4.44 MeV peak by 18% in the case of Wellisch and Axen and 17% in the case of Tripathi et al. (1999). It should be noted that the graphite phantom measurements were accidentally performed 2.4 cm before the Bragg peak, so the results displayed in

Figure 5.15 may differ slightly from a spectra taken at the Bragg peak position. The corresponding Geant4 simulations were also run at the same position (2.4 cm before the Bragg peak) as the measurements.

Based on the above comparisons, the Geant4 Monte Carlo model for prompt gamma-ray production shows discrepancies in the simulated results of up to 28% from the measured data (excluding the 4.44 MeV peak from ^{12}C during the water irradiation). All of the simulated results underestimated the measured values except again for the 4.44 MeV peak from the water target, which produced a 36% overestimation. These results will be looked at more closely when the absolute comparisons are discussed in Section 5.4. In the following section, we present results of comparison of prompt gamma-ray emissions from different depth along the beam path.

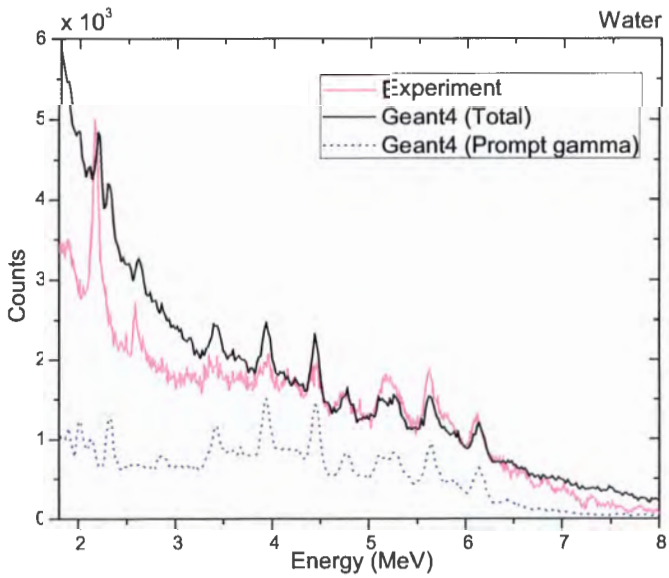

Figure 5.13: *Background-subtracted energy spectra detected from water phantom. Total measured energy spectra (gray line); total simulated energy spectra (black line); prompt gamma only simulated energy spectra (dotted line). Simulated spectra using the cross-sections of Wellisch and Axen. The Monte Carlo simulated results have been scaled by 0.85 for comparison purposes.*

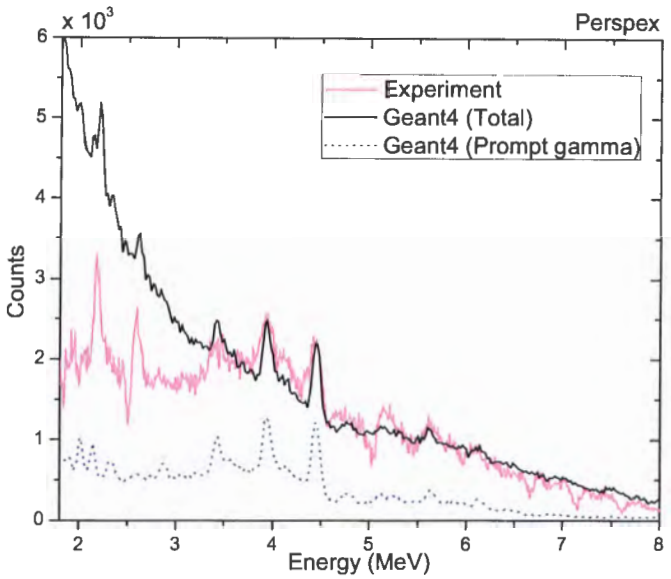

(a)

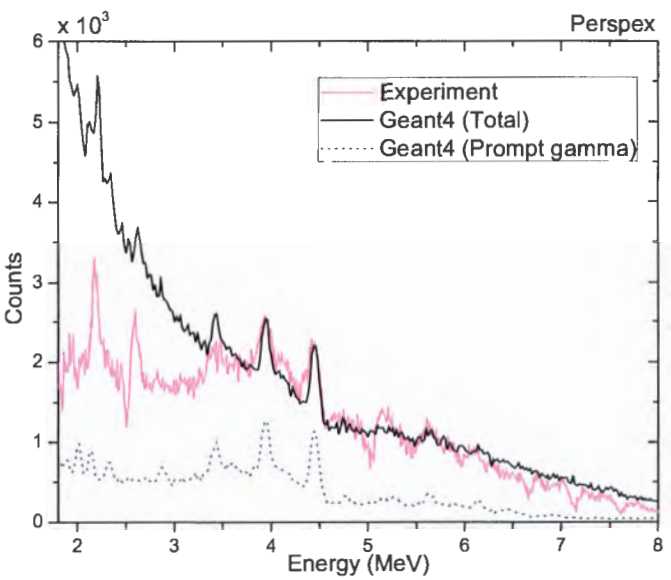

(b)

Figure 5.14: *Background-subtracted energy spectra detected from Perspex phantom. Total measured energy spectra (gray line); total simulated energy spectra (black line); prompt gamma only simulated energy spectra (dotted line). Simulated spectra using the cross-sections of (a) Wellisch and Axen and (b) Tripathi et al. (1999). The Monte Carlo simulated results have been scaled by (a) 0.8 and (b) 1.0 for comparison purposes.*

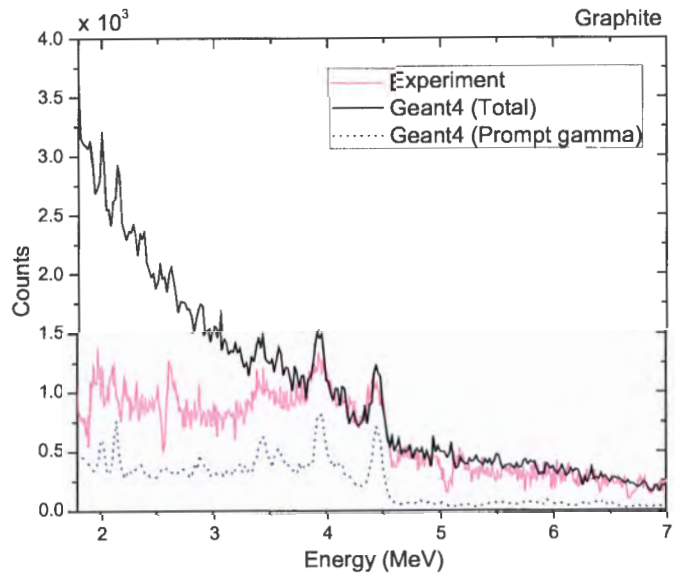

(a)

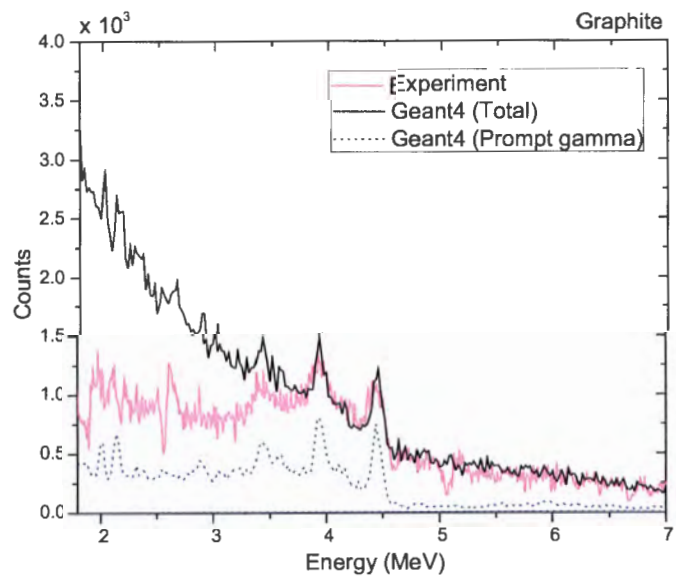

(b)

Figure 5.15: *Background-subtracted energy spectra detected from graphite phantom. Total measured energy spectra (gray line); total simulated energy spectra (black line); prompt gamma only simulated energy spectra (dotted line). Simulated spectra using the cross-sections of (a) Wellisch and Axen and (b) Tripathi et al. (1999). The Monte Carlo simulated results have been scaled by 1.9 for comparison purposes.*

5.3.3 Comparison of measured and simulated prompt gamma production along the beam path with target 170 cm from isocentre

The estimated prompt gamma counts from measurement and simulation emitted from the water and Perspex phantoms along the beam path is shown in Figures 5.16 and 5.17. For every single measurement, 2.3 x 10^{10} primary protons were simulated through the passive-scatter beam line nozzle. The Monte Carlo spectra were then scaled for comparison to the measured spectra, as indicated in the caption of each figure.

For the water phantom, the measured values (symbols) align reasonably well (within 15%) with the simulated points (dotted line) except for the 4.44 MeV emission in Figure 5.16(b) that shows some discrepancies before the Bragg peak. Both the simulations and experiments for the discrete prompt gamma energy emissions show good correlation with the depth-dose curve, peaking 1-2 cm before the Bragg peak (23.5 cm), as shown in Table 5.2. The experimental 3-7 MeV prompt gamma data peaks 2.8 cm before the Bragg peak while the simulated results over the same energy range peak at the same depth as the discrete prompt gamma peaks (2.0 cm). The consistent difference between the measured and simulated results highlights the fact there are a low number of measured data points (5) spread over a large distance. The two additional simulated data points show that the actual prompt gamma production peaks (discrete and "total") most likely occurred between two measured depths around 21.5 cm. Figure 5.16(d) also shows the measured depth results relative to the simulated prompt gamma spectra, where the discrete measured results peak 0.3 cm before the simulated peak (22.8 cm) while all the simulated results peak 1.3 cm before the prompt gamma peak. Again, the experimental prompt gamma depth production results for the 3-7 MeV energy range peaks 2.8 cm before the prompt gamma peak due largely to the lack of data closer to the actual peak.

For the Perspex phantom, Figure 5.17 shows the measured prompt gamma production results compared to the simulated values and the two sets of points line up well (within 12%) except for the points beyond the Bragg peak where the simulated results drop off more quickly than the measurements. The 4.44 and 6.13 MeV depth results both peak 0.9 cm before the Bragg peak (20.9 cm), while the 3-7 MeV measured depth curve peaks 2.4 cm before the Bragg peak. In Figure 5.17(d), the results again show that the 4.44 and 6.13 MeV depth curves peaks 0.3 cm from the maximum value of the simulated prompt gamma peak (20.3 cm), while the 3-7 MeV measured depth peaks 2.8

cm before the simulated peak. All of the distances between the Bragg peak (and also the simulated prompt gamma peak) and the peak of the prompt gamma-ray spectra from the water and perspex targets are summarized in Table 5.2.

Table 5.2: *Distances of the discrete gamma-ray spectra peaks from the Bragg peak (23.5 cm in case of water and 22.8 cm in case of Perspex) and the simulated prompt gamma peak (20.9 cm in case of water and 20.3 in case of perspex).*

		Difference from BP		Difference from PGP	
	PG	Experiment	Simulation	Experiment	Simulation
Target	(MeV)	(cm)	(cm)	(cm)	(cm)
water					
	4.44	1.0	2.0	0.3	1.3
	6.13	1.0	2.0	0.3	1.3
	3-7	3.5	2.0	2.8	1.3
Perspex					
	4.44	0.9	0.9	0.3	0.3
	6.13	0.9	0.9	0.3	0.3
	3-7	3.4	2.4	2.8	1.8

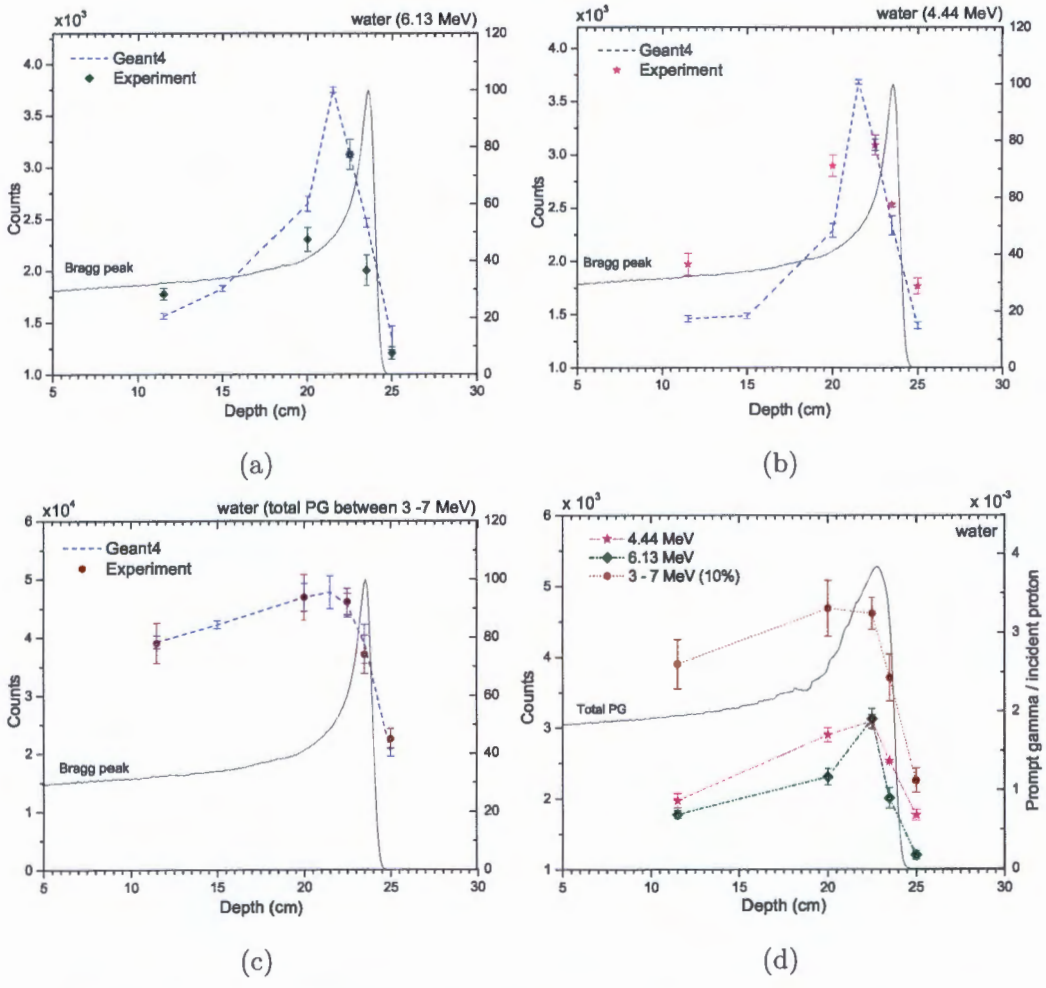

Figure 5.16: *Prompt gamma production along the beam path in water for 24 cm range passive-scatter protons for (a) 6.13 MeV peak from ^{16}O, (b) 4.44 MeV peak from ^{12}C (c) integrated over the 3 - 7 MeV energy range and (d) comparison of experimental depth results of 4.44, 6.13 and 3 - 7 MeV with simulated prompt gamma results. The simulated results have been scaled by (a) 5.5 (b) 3.0 and (c) 5.8 for comparison purposes. In Figure (d), the 3 - 7 MeV gamma counts has been scaled to 10% of its total value for display purposes. The right hand scale in (a), (b) and (c) indicates relative depth dose.*

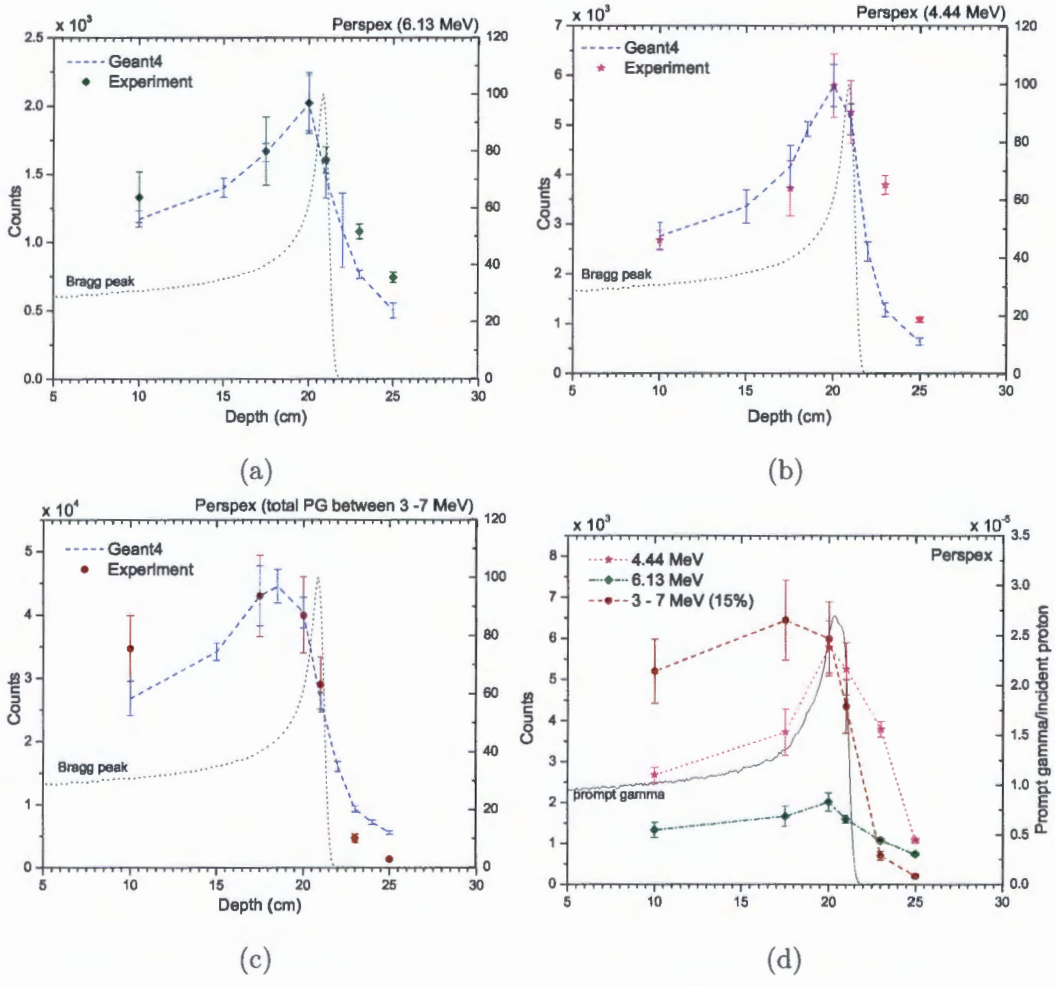

Figure 5.17: *Prompt gamma production along the beam path in Perspex for 24 cm range passive-scatter protons (in water) for (a) 6.13 MeV peak from ^{16}O , (b) 4.44 MeV peak from ^{12}C (c) integrated over the 3 - 7 MeV energy range and (d) comparison of experimental depth results of 4.44, 6.13 and 3 - 7 MeV with simulated prompt gamma results. The simulated results have been scaled by (a) 7.7 (b) 4.5 and (c) 4.2 for comparison purposes. In Figure (d), the 3 - 7 MeV gamma counts has been scaled to 15% of its total value for display purposes. The right hand scale in (a), (b) and (c) indicates relative depth dose.*

5.4 Absolute comparison of prompt gamma measurements to Monte Carlo simulations with target 170 cm from isocentre

An absolute comparison of the Monte Carlo simulations and the prompt gamma experimental measurements is presented in this section. An aspect of this work is to provide validation for the Monte Carlo simulations, so a comparison of results was done using the number of discrete prompt gammas detected per incident proton hitting the target, thus providing an independent comparison. In the Monte Carlo simulation, scaling the results into prompt gammas per incident target proton is straight forward, but for the passive-scatter beamline irradiations, this is challenging because there was no direct measurement of the number of protons hitting the target. The number of primary incident protons was estimated from the independent charge reading (measured in pulses) by the beam monitor ionization chamber positioned just before the final beam collimator in the passive-scatter beam nozzle. The estimate also relied on replicating standard calibration measurements (performed using the standard set-up at isocentre), which was then translated to the target position (at 170 cm) from the isocentre with the help of Monte Carlo simulations as described in the following section.

5.4.1 Determining the charge pulse to monitoring unit (MU) conversion factor for measurements 170 cm from isocentre

The ionization chamber calibration (using the standard set-up at isocentre) gives 48000 pulses per one monitoring unit (MU) when corrected for pressure and temperature. In our second set of measurements, a non-standard set-up was used where the ionization chamber was placed 120 cm upstream from its original position and the target was moved downstream along the beam direction 170 cm from the isocentre. Therefore, the standard calibration factor (48000 pulses/MU) was no longer valid for the new position of the ionization chamber and needed to be corrected using dose and fluence data from Monte Carlo simulations. We have assumed that the charge production in the active volume of the ionization chamber (independent charge reading) is proportional to the number of protons passing through it. The calibration factor (in pulses/MU) is directly tied to dose calibration measurements made in a water phantom. The dose is measured at 3 cm depth in a water phantom at isocentre using a small volume (0.32 x 0.32 x 0.1 cm^3) ion chamber. Using the conversion that 100 monitor unit equals 1 Gray (Gy)

of dose, the proton therapy beam line was calibrated so that 48000 pulses in the dose monitor is equivalent to 1 MU or 1 mGy. This calibration measurement was replicated in Geant4 in order to produce an updated charge pulse to monitor unit conversion factor for our non-standard experimental set-up. In the simulation, the dose estimated at isocentre with the standard set-up was 0.271 mGy from 2.399 x 10^7 protons hitting the water phantom through a 10 cm diameter collimator. For the experimental setup (dose monitor moved 120 cm upstream), the dose at isocentre was 0.266 mGy from 2.233 x 10^7 protons hitting the water phantom through a 10 cm diameter collimator. From these results, the proton fluence at isocentre was also estimated to be 1.131 x 10^7 proton/MU/cm^2 for the standard set-up and 1.070 x 10^7 proton/MU/cm^2 for the experimental set-up. Also the dose values can be used to calculate the dose conversion factor, converting the ion-chamber dose from the standard set-up to the experimental set-up, which was 0.980.

Determining the number of protons that hit the dose monitor in the two positions gives a charge pulse conversion factor of 0.619, converting dose monitor charge number from the standard set-up (2.595 x 10^7 protons) to the experimental set-up (4.164 x 10^7 protons). Taking these two conversion factors, the standard calibration factor of 48000 pulses/MU becomes 79100 pulses/MU for the experimental set-up, giving the appropriate translation of the independent charge count into monitor units, as shown in Table 5.3.

5.4.2 Calculating the number of incident protons on the different targets at 170 cm from isocentre

The number of incident protons hitting the target in the experimental set-up is dependant on converting the charge count into monitor unit conversion as well as on translating the proton fluence from the isocentre to the experimental target position. The calibrated fluence rate for the iThemba LABS passive-scatter beam is measured using a 10 cm diameter beam at the isocentre. The proton beam is considered uniform within this area. For the experimental set-up, the simulated value for the number of protons within a 10-cm diameter at isocentre is 2.079 x 10^7. In the same simulation, the number of protons within a 10-cm diameter field is 1.218 x 10^7, giving a fluence conversion factor of 0.586. The calculated fluence rate at the target position then becomes 6.27 x 10^6 protons/MU/cm^2. All above mentioned simulations were performed with 3.0 x 10^8 primary protons entering the beamline from the cyclotron.

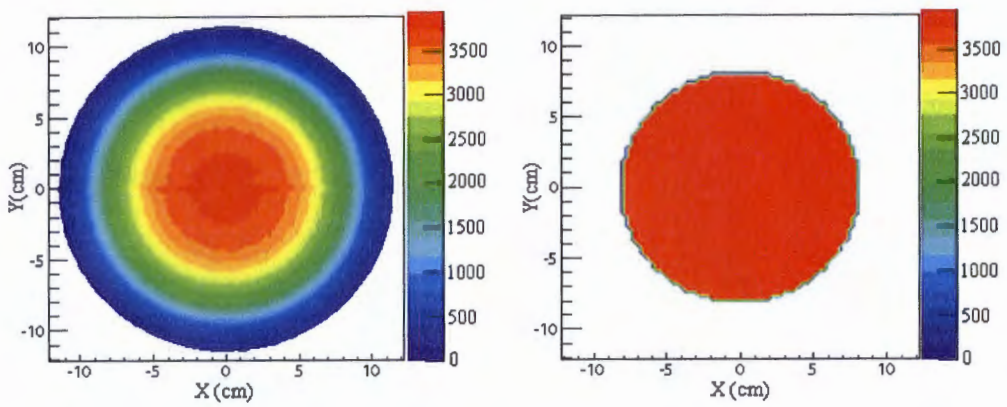

Figure 5.18: *(a) Original beam profile 170 cm from isocentre in experimental set-up and (b) a reconstructed beam profile used to estimate the equivalent field size at the surface of the water target.*

In the experimental set-up, there is significant beam divergence due to the long distance in which protons travel between the final beam collimator and target through the air. Although the final beam collimator was 10 cm in diameter, the actual field size at the target had a diameter of 22 cm, as shown in Figure 5.18(a). Since the density distribution of the protons hitting the target is non-uniform (except for the 5 cm diameter central circle) and the cross-sectional area of the targets (25 x 25 cm for water, 19 x 20 cm for perspex, and 4.8 x 6.5 cm for graphite) is exposed to this non-uniformity, effective field sizes were calculated for each target. The calculated fluence rate assumes a 10 cm diameter uniform proton beam, so to convert from fluence to number of protons, the non-uniform proton beam was reconstructed into a smaller, uniform density distribution.

The number of protons hitting the target face was estimated using the simulated 22-cm proton density distribution then that number was used to determine the density of an equivalent field with uniform density as it appears in the central spot (3740 protons/bin for this case). For the water phantom (with its 25 cm x 25 cm cross section), the entire 20 cm diameter region was reconstructed into a 14.78-cm diameter circle, shown in Figure 5.18(b). For the perspex phantom, a 16-cm diameter region was reconstructed into a 12-cm diameter circle. For the graphite block, the actual dimensions of 4.8 cm x 6.5 cm were used to estimate the particle fluence because the central spot almost

Table 5.3: *Summary of calculation of incident protons from monitor ionization chamber readings. The calibration factor of the chamber is 79100 pluses/MU and the fluence rate at the target position was 6.27 x 10^6 proton/MU/cm^2.*

Target	Dose Monitor Reading (pulse)	Monitor Units (MU)	Fluence (proton/cm^2)	Effective Area (cm^2)	Total Incident Protons
Perspex	1166006	14.74	9.24 x 10^7	113.1	10.45 x 10^9
Water	673092	8.51	5.34 x 10^7	171.6	9.15 x 10^9
Graphite	966668	12.22	7.66 x 10^7	31.20	2.39 x 10^9
Perspex	991525	12.54	7.86 x 10^7	113.1	8.89 x 10^9
(depth	1086316	13.73	8.61 x 10^7	113.1	9.74 x 10^9
Measurements)	1037955	13.12	8.23 x 10^7	113.1	9.31 x 10^9
	1054816	13.34	8.36 x 10^7	113.1	9.46 x 10^9
	733478	9.27	5.81 x 10^7	113.1	6.58 x 10^9
	937653	11.85	7.43 x 10^7	113.1	8.41 x 10^9
Water	1702868	21.53	1.35 x 10^8	171.6	2.32 x 10^{10}
(depth	1660439	20.99	1.32 x 10^8	171.6	2.26 x 10^{10}
Measurements)	1400789	17.71	1.11 x 10^8	171.6	1.91 x 10^{10}
	2160436	21.31	1.71 x 10^8	171.6	2.94 x 10^{10}
	1945127	24.59	1.54 x 10^8	171.6	2.65 x 10^{10}
	1179126	14.91	9.35 x 10^7	171.6	1.60 x 10^{10}

completely covered the target cross-section. Table 5.3 summarizes the details of the number of incident proton calculations for each measurement.

5.4.3 Comparison of measured and simulated prompt gamma production peaks

Absolute comparison between measurements and simulations of prompt gamma spectra emitted from water, Perspex and graphite target results are shown in Figures 5.19 to 5.21 for a 24-cm range proton beam. The number of prompt gammas per incident proton in the 6.13 MeV and 4.44 MeV discrete prompt gamma-ray peaks (and their single and double escape peaks) and the relative difference between the simulations from the measurements are summarized in Table 5.4. The baseline subtraction method is used to estimate the number of prompt gamma-rays in every peak. For the water target (Figure 5.19), the simulation of the 4.44 MeV peak shows a significantly large difference (simulation overestimates the photo peak by a factor of 0.56) between the measurement and simulation whereas the agreement is excellent (1%) for the 6.13 MeV gamma line. For the graphite and Perspex targets, the measured and simulated values

Table 5.4: *Absolute difference (S-M)/M of simulated (S) from the measured (M) counts per incident proton for the 6.13 MeV and,4.44 MeV and 3 - 7 MeV prompt gamma lines per incident proton. Measurement is taken at the Bragg peak. *Simulations performed with the cross-section Tripathi et al. (1999) instead of the default Wellisch and Axen cross-section.*

		4.44 MeV			6.13 MeV			3 - 7 MeV
Targets		Photo peak (x10^{-7})	1^{st} escape peak (x10^{-7})	2^{nd} escape peak (x10^{-7})	Photo peak (x10^{-7})	1^{st} escape peak (x10^{-7})	2^{nd} escape peaks (x10^{-7})	Counts per proton (x10^{-5})
Water	Experiment	7.47	7.75	7.11	8.11	10.8	23.3	1.55
	Simulation	11.7	12.1	8.66	8.04	8.43	12.8	1.40
	Difference	+0.56	+0.56	+0.21	-0.01	-0.21	-0.45	-0.10
Perspex	Experiment	14.3	11.1	8.22	3.26	6.03	5.80	2.06
	Simulation	12.9	11.4	5.41	3.27	2.71	3.03	0.943
	Difference	-0.1	-0.03	-0.34	0.00	-0.55	-0.48	-0.54
	Simulation*	15.5	11.4	5.91	2.43	7.45	5.63	1.22
	Difference*	+0.08	-0.03	-0.28	-0.25	-0.24	-0.03	-0.40
Graphite	Experiment	42.4	29.7	25.4				2.87
	Simulation	40.8	37.8	26.9				2.10
	Difference	-0.04	-0.27	+0.06				-0.27
	Simulation*	39.2	25.7	21.0				2.47
	Difference*	-0.07	-0.13	-0.17				-0.14

also agree quite well (up to 8% difference) at the photo peaks. The agreement is not as good for the escape peaks, particularly for ^{16}O where the simulation underestimates the first and second escape peak of ^{16}O by up to 55%. It should also be noted that the 5.25 MeV peak from ^{15}O is not included in our calculations. The comparison between the two cross-section data-sets for the graphite target shown in Table 5.4 shows that the peaks produced with the Tripathi et al. (1999) cross-section does not produce a significant difference with the Willish and Axen data-set except for the first escape peak where there is a 27% difference. The overall performance of the simulation is reasonable particularly at the photo peaks again except for the 4.44 MeV peak in the water target due to the deficiency in the Geant4 physics model at that point as previously mentioned. As expected, the simulated prompt gamma spectra displayed less broadening with a larger peak height than the spectra obtained experimentally due to the absence of Doppler broadening in our Geant4 model. The effect of the Doppler broadening effect will be included in the model in future work.

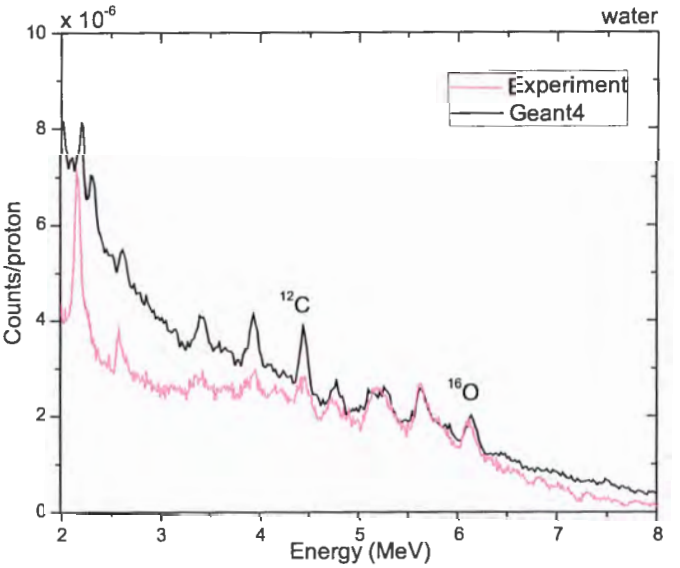

Figure 5.19: *Absolute comparison of background-subtracted energy spectra detected from water phantom. Total measured energy spectra (light pink line); total simulated energy spectra (black line)*

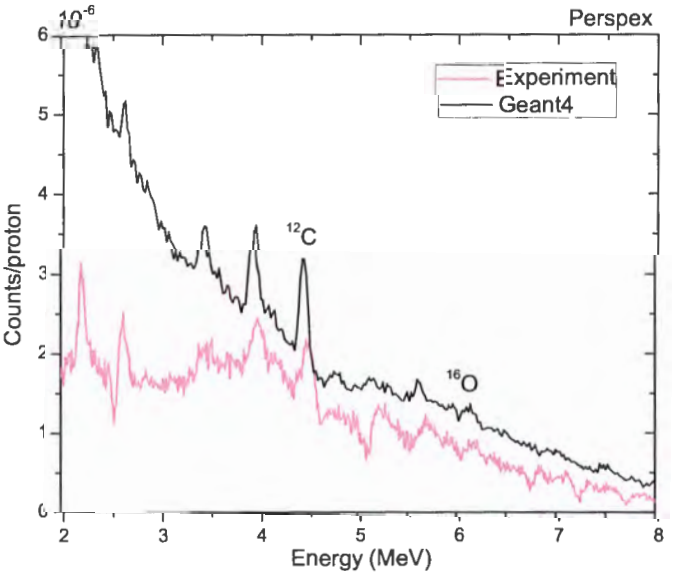

Figure 5.20: *Absolute comparison of background-subtracted energy spectra detected from Perspex phantom. Total measured energy spectra (light pink line); total simulated energy spectra (black line)*

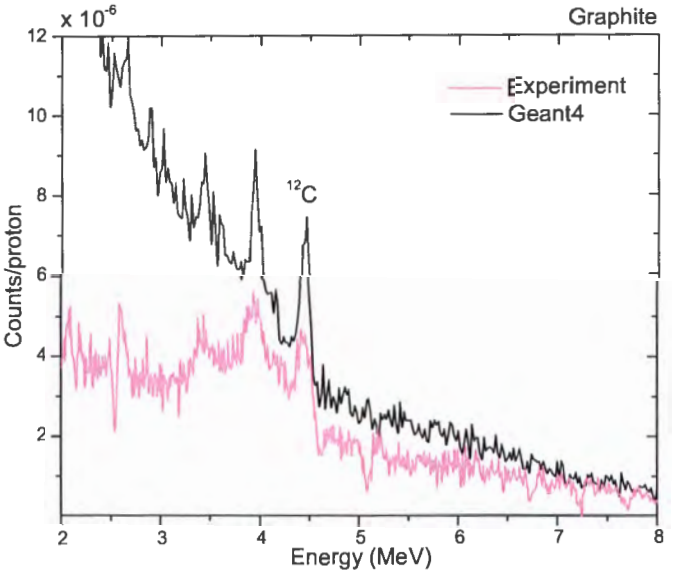

Figure 5.21: *Background-subtracted energy spectra detected from Graphte phantom. Total measured energy spectra (light pink line); total simulated energy spectra (black line). Simulated spectra using the cross-sections of) Tripathi et al. (1999) instead of the Wellisch and Axen.*

5.4.4 Comparison of measured and simulated prompt gamma production peaks along the beam path

Similar to the comparison discussed in Section 5.3.3, the results in Figure 5.22 show the number of gammas per incident proton in the discrete peaks (4.44 MeV and 6.13 MeV) and in the 3-7 MeV energy range at various depths within the targets. The basic shape of these depth curves remain the same as well as the distance measurements listed in Table 5.2. This absolute comparison provides a measure of the accuracy of the Monte Carlo simulated results against the measured experimental data. Starting with the water phantom (Figure 5.22(a)), the simulated spectra obtained for the 6.13 MeV prompt gamma emission are accurate (all results within 13% except for the point beyond the Bragg peak) whereas the simulated 4.44 MeV gamma peak values show a large discrepancy (31-95%) with the experimental results as summarised in Table 5.5. A similar difference in the 4.44 MeV gamma emission from water has been found throughout all the previous discussed comparisons (section 5.4.3 and Table 5.4). This discrepancy can be traced back to Figure 4.11, where the gamma production cross-section for 4.44 MeV emission from ^{16}O is overestimated in the proton energy range of 20-35 MeV. The

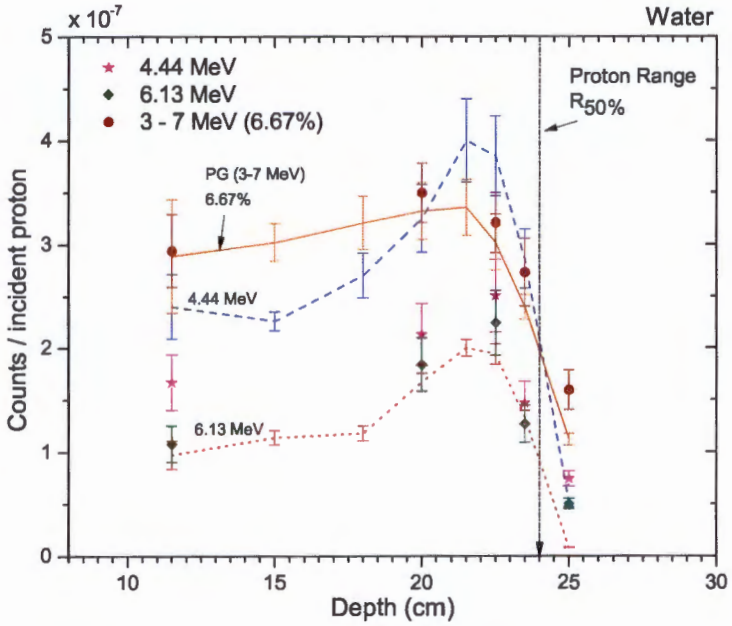

(a)

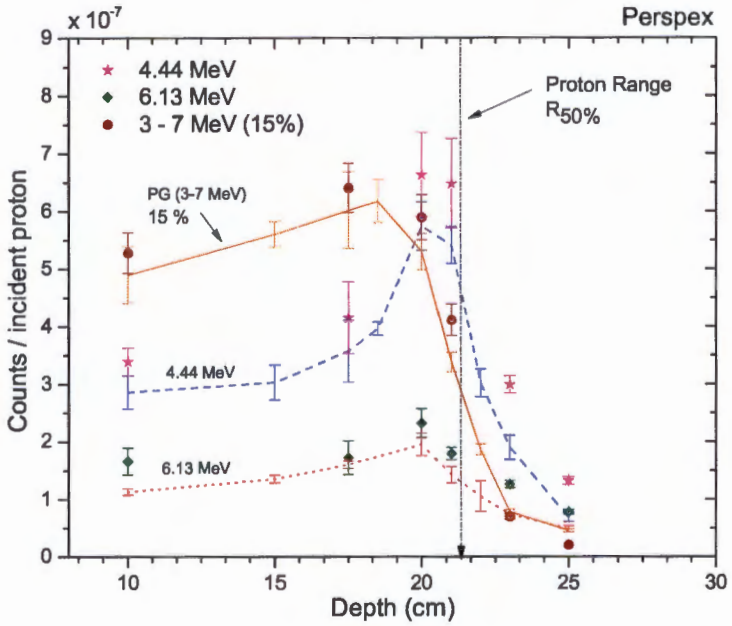

(b)

Figure 5.22: *Absolute comparison of the measured (symbols) and simulated (lines) prompt gamma production along the beam path for the 4.44 MeV (dashed line) gamma peak, the 6.13 MeV (dotted line) gamma peak and the total prompt gamma count in the 3-7 MeV energy range in the (a) water and (b) perspex phantoms. The proton range ($R_{50\%}$) is included for comparison purposes and the 3-7 MeV gamma counts have been scaled to (a) 6.67% and (b) 15% of their total values for display purposes. .*

Table 5.5: *Absolute difference (S-M)/M of simulated (S) from the measured (M) gamma counts per incident proton for the 6.13 MeV and the 4.44 MeV gamma peaks as well as over the 3-7 MeV energy range for depths within the water target.*

PG Energy	Depth	Experiment	Simulation	Difference
6.13 MeV	11.5	1.08×10^{-7}	9.74×10^{-8}	-0.10
	20.0	1.84×10^{-7}	1.67×10^{-7}	-0.09
	22.5	2.24×10^{-7}	1.94×10^{-7}	-0.13
	23.5	1.27×10^{-7}	1.33×10^{-7}	+0.05
	25.0	5.03×10^{8}	8.40×10^{9}	-0.83
4.44 MeV	11.5	1.67×10^{-7}	2.40×10^{-7}	+0.44
	20.0	2.13×10^{-7}	3.25×10^{-7}	+0.53
	22.5	2.50×10^{-7}	3.85×10^{-7}	+0.54
	23.5	1.47×10^{-7}	2.86×10^{-7}	+0.95
	25.0	7.44×10^{-8}	5.14×10^{-8}	-0.31
3 - 7 MeV	11.5	4.41×10^{-6}	2.89×10^{-6}	-0.35
	20.0	5.24×10^{-6}	3.32×10^{-6}	-0.37
	22.5	4.81×10^{-6}	3.02×10^{-6}	-0.37
	23.5	4.09×10^{-6}	2.39×10^{-6}	-0.41
	25.0	2.39×10^{-6}	1.12×10^{-6}	-0.53

alternate (combined) model described in the Section 4.1.4 (also see Figure 4.12) also produced a reasonable fit to the experimental cross-section data in the above mentioned energy range and could provide another option for accurate simulations with the water target. Of course, the physics model may not be the only reason for the discrepancy, this simulation study has not explicitly taken detector efficiency into account nor has there been an exhaustive look at the uncertainty wrapped into the proton fluence calculations, both possible areas of discrepancies. For the 3-7 MeV gammas, the simulation consistently underestimated (35-53%) the measured values which is quite interesting considering that this energy range includes the gross overestimation from the 4.44 MeV gamma peak.

For the perspex target, the overall agreement between the simulated and measured results agrees better (total average of 26%) than the results for the water phantom (total average of 40%). Both the 4.44 MeV and 6.13 MeV simulated results underestimate the measured results by 24% and 26% on average respectively (see Table 5.6), which is not surprising considering that the simulated 4.44 MeV gamma results should be

Table 5.6: *Absolute difference (S-M)/M of simulated (S) from the measured (M) gamma counts per incident proton for the 6.13 MeV and the 4.44 MeV gamma peaks as well as over the 3-7 MeV energy range for depths within the Perspex target.*

PG Energy	Depth	Experiment	Simulation	Difference
6.13 MeV	10.0	1.66×10^{-7}	1.13×10^{-7}	-0.32
	17.5	1.72×10^{-7}	1.60×10^{-7}	-0.07
	20.0	2.32×10^{-7}	1.95×10^{-7}	-0.16
	21.0	1.79×10^{-7}	1.42×10^{-7}	-0.21
	23.0	1.26×10^{-7}	7.38×10^{-8}	-0.41
	25.0	7.78×10^{-8}	4.84×10^{-8}	-0.38
4.44 MeV	10.0	3.39×10^{-7}	2.68×10^{-7}	-0.16
	17.5	4.15×10^{-7}	3.57×10^{-7}	-0.14
	20.0	6.63×10^{-7}	4.74×10^{-7}	-0.13
	21.0	6.48×10^{-7}	4.41×10^{-7}	-0.17
	23.0	2.99×10^{-7}	1.90×10^{-7}	-0.36
	25.0	1.32×10^{-8}	6.83×10^{-8}	-0.48
3 - 7 MeV	10.0	3.52×10^{-6}	3.26×10^{-6}	-0.07
	17.5	4.27×10^{-6}	4.01×10^{-6}	-0.06
	20.0	3.93×10^{-6}	3.53×10^{-6}	-0.10
	21.0	2.74×10^{-6}	2.25×10^{-6}	-0.18
	23.0	4.66×10^{-7}	5.17×10^{-6}	-0.11
	25.0	1.38×10^{-7}	3.04×10^{-6}	-1.20

lower (see Figure 4.7). As discussed in Section 4.1.4, the 4.44 MeV prompt gamma emission from ^{12}C performed with the total inelastic cross-section of Tripathi et al. (1999) was in better agreement with the experiment than the results obtained with the default total inelastic cross-section of Wellisch and Axen (see Figure 4.7), but since the cross-section of Tripathi et al. (1999) overestimates the 6.13 MeV prompt gamma from ^{16}O (see Figure 4.10), the cross-section of Wellisch and Axen was used for the Perspex target simulations, so the underestimation of the 6.13 MeV gamma peak is unexpected. It should also be mentioned that although there is reasonable agreement between the simulation and experiment for the 6.13 MeV line, the task of counting the 6.13 MeV prompt gamma emission for each depth was difficult because of the low signal to background ratio due to the high scattered radiation presence during the passive-scatter beam irradiation (see Figure 5.21 as an example). The 3-7 MeV gamma results produced excellent agreement (10% on average) except again for the point beyond the Bragg peak.

5.5 Summary

The main purpose of our work in this chapter has been to learn more about the discrete prompt gamma emitted from different materials with the clinical passive-scatter proton irradiation. The experimental results indicate that the prompt gamma measurement with the passive-scatter proton beam can be possible, but presence of high amount of radiation scattered from beam line elements and patient final collimator made it difficult to perform at the isocentre. However, the prompt gamma measurements with the target at 170 cm from the isocenter were quite well. The important prompt gamma peaks were clearly identified for the water, Perspex and graphite targets, but not resolved for the liquid nitrogen target (only the 2.313 MeV peak was identified). The agreement between the measurement and simulation showed a very satisfying at the photo peak except the simulation of the 4.44 MeV from water showed a significantly larger difference overestimated by a factor of 0.5. The prompt gamma emission at different positions along the beam path for water and Perspex were also quantified and the overall agreements between the simulation and measurement were better. The correlation between the location of each prompt gamma emission along the beam path and the location of Bragg peak is promising the feasibility of range verification for passive-scatter proton therapy. A large difference in the 4.44 MeV emission from the water was observed throughout all our comparisons because of the gamma production cross-section for 4.44 MeV emission from ^{16}O was overestimated in the proton energy range of 20-30 MeV. Overall, our developed Monte Carlo model suits well for the prompt gamma measurement.

Chapter 6

Conclusion

In this thesis, we present the first discrete prompt gamma measurements performed in the clinical passive-scatter proton beam environment. There were two specific aims for this dissertation; first, the measurement of prompt gamma production from elements ^{16}O, ^{12}C and ^{14}N (the most abundant elements in human tissue) in the clinical passive-scatter treatment environment. Second, the development of a Monte Carlo model of the experimental setup (proton beam line, phantom set-up and detector) for preliminary predictions regarding the measurements, for comparison to final measured results and investigation into the physics behind the simulated results.

For the measurements, the discrete prompt gamma-ray emitted from water, Perspex, graphite and liquid nitrogen targets irradiated by a clinical passive-scatter proton beam of 200 MeV were investigated. The spectra were detected by a high resolution $LaBr_3$ detector. Although there was additional secondary radiation activated in the beam line elements and in the final collimator, the experimental results clearly indicate that the prompt gamma measurement with the passive-scatter proton beam can be possible. The important prompt gamma peaks were clearly identified for the water, Perspex and graphite targets, but not resolved for the liquid nitrogen target. Throughout this study, we quantified the discrete prompt gamma emission from the excited state of ^{12}C (4.44 MeV) and ^{16}O (6.13 MeV) and in the interested energy range of 3 - 7 MeV. The correlation between the location of each prompt gamma emission along the beam path and the location of the Bragg peak was reasonable and shows promise in the feasibility of range verification for passive-scatter proton therapy.

In addition to the measurements, a Monte Carlo model of the entire experimental set-up including the beam line elements and $LaBr_3$ detector was developed and is based on the Geant4 Monte Carlo code (version 9.6.p02). Three different Geant4 physics models (BIC, PRECO and INCLXX) for discrete gamma emission from the excited states of ^{16}O, ^{12}C and ^{14}N were tested against the currently available experimental cross-section data by looking at Geant4 parameters; Doppler broadening, number of excitons (n), Fermi breakup and Geant4 inelastic reaction cross-section data set.

For this study, the most important prompt gamma lines are at 6.13 MeV from the excited state of $^{16}O^*$ and 4.44 MeV from the excited state of $^{12}C^*$ since almost 80% of the mass of the human body is made by Oxygen (65%) and Carbon (15%). Our simulation results show that applying the Doppler broadening setting within a Geant4 simulation underestimates the prompt gamma peak at 6.13 MeV most expected experimentally produced by proton inelastic collisions on ^{16}O, but the prompt gamma peaks at 4.44 MeV and 5.20 MeV are reasonably estimated. Therefore the Doppler broadening effect was disabled to consider the prompt gamma emission directly from the specific transition.

By default, the binary cascade model is included by default in the selected physics list QGSP_BIC_EMY for proton inelastic nuclear reactions. Our comparisons to the cross-section data clearly indicated that the binary cascade model does not accurately reflect the data, instead producing the highest prompt gamma emission at the 5.180 MeV line from the excited state of $^{15}O^*$ and producing an extremely low 6.13 MeV line. The expected peak for tissue in the interested energy range of 3 - 7 MeV should be the 6.13 MeV peak and the 5.2 MeV peak should only be the third most prominent prompt gamma line emission (Verburg et al. (2013)).

A suitable alternative was found with the precompound model, which required some modification (using an alternative initial nuclear exciton state of 2) in order to decrease the peak at 5.180 MeV while increasing the peak at 6.13 MeV. Due to the close agreement between the Geant4-generated prompt gamma emissions by the precompound model and the currently available experimental data for discrete lines from ^{12}C, ^{16}O and ^{14}N, the binary cascade model was replaced by the precompound model.

The discrete lines from ^{12}C and ^{14}N obtained with the total inelastic cross-section of Tripathi et al. (1999) were in better agreement with the experiment than the results obtained with the default total inelastic cross-section of Wellisch and Axen. Therefore the cross-section of Tripathi light ion (Tripathi et al. (1999)) was used for both the

graphite and liquid nitrogen targets. However, the cross-section data of Willish and Axen was used to simulate prompt gamma production in the water and Perspex targets. The Fermi break-up was required below 20 MeV for the water and Perspex targets.

Although the precompound model with the two different cross-section data-sets (Willish and Axen and Tripathi light ion) provided the closest possible agreement to the available experimental cross-section data, there is still room for improvement, both in the cross-section data and in the physics models. The majority of the experimental cross-section data used in this work was taken in an astrophysical context and does not provide complete coverage of the required energies. In Geant4, the total inelastic cross-section comparison was reasonable, but there were definite deficiencies in the Geant4 physics models when looking at the production of specific prompt gammas from specific elements.

The developed Geant4 Monte Carlo model was then validated against the experimental depth dose and lateral dose profiles. The developed treatment nozzle model was in good agreement with treatment-relevant measurements and had the ability to produce depth dose and lateral profiles in a water phantom for different proton ranges. The simulated and measured range (R_{50}) agreed within 0.5% for proton ranges between 5 and 24 cm. The detector was calibrated for its response in the energy range of 0.661 to 4.438 MeV using seven standard gamma emitting sources and the ^{241}AmBe neutron source listed in Table 4.4. The calculated user defined Gaussian parameters is listed in Table 4.5.

Once the selection of physics models was settled, additional investigation went into developing the Geant4 simulation for prompt gamma-rays in both the active-scanning and passive-scatter proton beam modes. Two techniques were studied to specifically minimize the background noise from the secondary scattered radiation, a significant problem during passive-scatter proton irradiations, a time-of-flight (TOF) window and Compton-suppression using a BGO detector. Both techniques significant reduced the background radiation and the BGO subtraction also helped to resolve the 5.25 MeV prompt gamma line from the second escape peak of ^{16}O. Using a TOF window, it was possible to remove 99% of the noise due to neutrons hitting the detector from the target. The results show that using both timing and active shielding in the passive beam mode can remove up to 90% of the background radiation which includes a 10% reduction by BGO subtraction.

Finally, an absolute comparison of the Monte Carlo simulations and the experimental measurements was made to align the Geant4 simulations as closely as possible to the

measured results for two separate scenarios (using a 5 cm gap and 1 cm gap in the collimator). For the 5 cm collimator gap, the Geant4 Monte Carlo model for prompt gamma-ray production for the two discrete (4.44 and 6.13 MeV) peaks underestimated the measured values by less than 10% for the water, Perspex and graphite target. The one noticeable exception was the 4.44 MeV peak from the water target, which showed an almost 50% overestimation of the number of produced prompt gammas. For prompt gamma measurements along the beam path (using the 1 cm collimator gap), the simulation did not match the measured data quite as nicely, producing on average 24-26% differences across the discrete peaks in water and perspex. Again, the 4.44 MeV peak in the water target produced a much larger variation (up to 93%). Although these numbers do not seem to agree as well, due to the thinner collimation there was a lower number of detected gammas, thus producing much higher uncertainty in the results.

Overall, the Monte Carlo model of the iThemba LABS proton therapy beamline performed well, matching validation treatment dose profiles to within 3% and replicating prompt gamma photo peak production numbers to within 10%. This model was able to adequately replicate measured prompt gamma production results and will continue to be used for further prompt gamma studies at the University of Cape Town using the passive-scatter beamline at iThemba LABS. The gross overestimation of the 4.44 MeV peak produced by the water target will be investigated and may lead to changes in the physics models within Geant4. Further improvement to the current model by being able to fully incorporate the Doppler broadening effect will also be undertaken. The uncovered deficiencies in the inelastic nuclear cross section data relevant to clinical proton radiotherapy environment have prompted a verification of the existing cross-section data and an investigation into producing more cross-section data at the energies relevant to proton therapy.

Part IV

Appendices

Appendix A

Composition and densities of materials

Table A.1: *Composition and densities of materials*

Material	Density (g/cm^3)	Symbol	Z	Percentage
Air	0.001205	C	6	0.0124
NIST definition		N	7	75.5267
Near sea level		O	8	23.1781
		Ar	18	1.2827
Aluminium	2.699	Al	13	100
Brass, Type C36000	8.496	Cu	29	56.9297
(Free-cutting brass)		Zn	30	33.7131
		Pb	82	9.3572
Carbon	2.267	C	6	100
Cerrobend	9.382	Cd	48	6.0160
(Ostalloy 158, Wood's metal		Sn	50	8.4490
Melt-point:70 Celcius)		Pb	82	29.6088
		Bi	83	55.9262
Concrete (Portland)	2.30	H	1	1.0000
		C	6	0.1000
		O	8	52.9107

Continued on next page

Table A.1 – *Continued from previous page*

Material	Density (g/cm^3)	Symbol	Z	Percentage
		Na	11	1.6000
		Mg	12	0.2000
		Al	13	3.3872
		Si	14	33.7021
		K	19	1.3000
		Ca	20	4.4000
		Fe	26	1.4000
Copper	8.960	Cu	29	100
Graphite	1.860	C	6	100
Havar	8.302	C	6	0.0394
		Cr	24	16.6239
		Mn	25	1.4412
		Fe	26	17.4889
		Co	27	40.5824
		Ni	28	12.2249
		Mo	42	3.4606
		W	74	8.1387
Kapton	1.420	H	1	2.6362
		C	6	69.1133
		N	7	7.3270
		O	8	20.9235
Lead	11.35	Pb	82	100
Lexan	1.200	H	1	4.1959
		C	6	62.5017
		O	8	33.3025
Liquid Nitrogen	0.8070	N	7	100
Mylar	1.400	H	1	4.1959
		C	6	62.5017
		O	8	33.3025
NaI	3.667	Na	11	15.34
		I	53	84.66

Continued on next page

Table A.1 – *Continued from previous page*

Material	Density (g/cm^3)	Symbol	Z	Percentage
Nitrogen	1.290	N	7	100
Oxygen	1.141	O	8	100
Paraffin Wax	0.93	H	1	14.8605
		C	6	85.1395
Perspex1 (RM wheels)	1.145	H	1	8.0538
		C	6	59.9848
		O	8	31.9614
Perspex2 (Block)	1.19	H	1	8.0538
		C	6	59.9848
		O	8	31.9614
Perspex3 (Lucite)	1.181	H	1	8.0538
		C	6	59.9848
		O	8	31.9614
Tungsten	19.30	W	74	100
Water	1.000	H	1	11.1894
		O	8	88.8106

Appendix B

GPS command for AmBe neutron source

/gps/source/intensity 1.0

/gps/particle neutron

/gps/number 1

/gps/pos/centre 0. 0. 0. cm

/gps/pos/type Volume

/gps/pos/shape Cylinder

/gps/pos/centre 0. 0. 0. cm

/gps/pos/radius 0.53975 cm

/gps/pos/halfz 1.8 cm

/gps/ang/type iso

/gps/ene/min 2.72 MeV

/gps/ene/max 10.0 MeV

/gps/ene/type Arb

/gps/ang/type iso

/gps/hist/type arb

/gps/hist/point 2.72 2.5

/gps/hist/point 2.96 2.68

/gps/hist/point 3.21 2.8

```
/gps/hist/point 3.53 2.62
/gps/hist/point 3.8 2.3
/gps/hist/point 4.11 2.05
/gps/hist/point 4.37 2.16
/gps/hist/point 4.59 1.93
/gps/hist/point 4.86 2.16
/gps/hist/point 5.11 2.11
/gps/hist/point 5.36 2.01
/gps/hist/point 5.61 1.84
/gps/hist/point 5.81 1.6
/gps/hist/point 5.988 1.41
/gps/hist/point 6.21 1.294
/gps/hist/point 6.57 1.29
/gps/hist/point 6.66 1.3
/gps/hist/point 6.9 1.41
/gps/hist/point 7.14 1.32
/gps/hist/point 7.31 1.35
/gps/hist/point 7.53 1.51
/gps/hist/point 7.74 1.58
/gps/hist/point 7.96 1.5
/gps/hist/point 8.12 1.10
/gps/hist/point 8.31 0.74
/gps/hist/point 8.49 0.6
/gps/hist/point 8.69 0.42
/gps/hist/point 9.27 0.31
/gps/hist/point 9.81 0.22
/gps/hist/point 10. 0.
/gps/hist/inter Lin
/gps/source/add 0.573
```

```
/gps/particle gamma
/gps/pos/type Volume
/gps/pos/shape Cylinder
/gps/pos/centre 0. 0. 0. cm
/gps/pos/radius 0.53975 cm
/gps/pos/halfz 1.8 cm
/gps/ang/type iso
/gps/ene/type Mono
/gps/ene/type Gauss
/gps/energy 4.438 MeV
/gps/ene/sigma 0.5 MeV
/gps/pos/centre 0. 0. 0.0 cm
```

Bibliography

Agostinelli, S., Allison, J., Amako, K., Apostolakis, J., 2003. Geant4 a simulation toolkit. Nuclear Instruments and Methods in Physics Research Section A: Accelerators, Spectrometers, Detectors and Associated Equipment 506 (3), 250 – 303.

Albertini, F., Bolsi, A., Lomax, A. J., Rutz, H. P., Timmerman, B., Goitein, G., 2008. Sensitivity of intensity modulated proton therapy plans to changes in patient weight. Radiotherapy and Oncology 86 (2), 187 – 194.

Amgarou, K., Domingo, C., Bouassoule, T., FernÃąndez, F., 2009. Monte carlo simulation of the nai(tl) detector response to measure gold activated foils. Nuclear Instruments and Methods in Physics Research Section B: Beam Interactions with Materials and Atoms 267 (17), 2944 – 2951.

Andreo, P., 2009. On the clinical spatial resolution achievable with protons and heavier charged particle radiotherapy beams. Phys. Med. Biol 54, N205–N215.

Belhout, A., Kiener, J., Coc, A., Duprat, J., Engrand, C., Fitoussi, C., Gounelle, M., Lefebvre-Schuhl, A., Séréville, N. d., Tatischeff, V., Thibaud, J.-P., Chabot, M., Hammache, F., Benhabiles-Mezhoud, H., Sep 2007. γ-ray production by proton and α-particle induced reactions on ^{12}C, ^{16}O, ^{24}Mg, and fe. Phys. Rev. C 76, 034607.

Benhabiles-Mezhoud, H., Kiener, J., Thibaud, J.-P., Tatischeff, V., Deloncle, I., Coc, A., Duprat, J., Hamadache, C., Lefebvre-Schuhl, A., Dalouzy, J.-C., de Grancey, F., de Oliveira, F., Dayras, F., de Séréville, N., Pellegriti, M.-G., Lamia, L., Ouichaoui, S., Feb 2011. Measurements of nuclear γ-ray line emission in interactions of protons and α particles with N, O, Ne, and Si. Phys. Rev. C 83, 024603.

Bichsel, H., Hiraoka, T., 1992. Energy lost of 70 mev protons in elements. Nucl. Instrum. Methods Phys. Res. B 66, 345–51.

Biegun, A. K., Seravalli, E., Lopes, P. C., Rinaldi, I., Pinto, M., Oxley, D. C., Dendooven, P., Verhaegen, F., Parodi, K., Crespo, P., Schaart, D. R., 2012. Time-of-flight neutron rejection to improve prompt gamma imaging for proton range verifiation: a simulation study. Phys. Med. Biol. 57, 6429–6444.

Brenner, D., Prael, R., 1989. Calculated differential secondary-particle production cross

sections after nonelastic neutron interactions with carbon and oxygen between 15 and 60 MeV. Atomic Data and Nuclear Data Tables 41 (1), 71 – 130.

Chadwick, M. B., 2012. ENDF nuclear data in the physical, biological, and medical sciences. Int. J. Radiat. Biol. 88, 10–4.

Cirrone, G. A. P., Cuttone, G., Guatelli, S., Nigro, S. L., Mascialino, B., Pia, M. G., Raffaele, L., Russo, G., , Sabini, M. G., 2005. Implementation of a New Monte Carlo GEANT4 Simulation Tool for the Development of a Proton Therapy Beam Line and Verification of the Related Dose Distributions. IEEE TRANSACTIONS ON NUCLEAR SCIENCE 52, 262–5.

Cirrone, G. A. P., Cuttone, G., Mazzaglia, S. E., Romano, F., Sardina, D., Agodi, C., Attili, A., Blancato, A. A., Napoli, M. D., Rosa, F. D., Kaitaniemi, P., Marchett, F., Petrovic, I., Ristic-Fira, A., Shin, J., Tarnavsky, N., Tropea, S., Zacharatou, C., 2011. Hadrontherapy: a geant4-based tool for proton/ion-therapy studies. Progress in NUCLEAR SCIENCE and TECHNOLOGY 2, 207–212.

Cortés-Giraldo, M. A., Quesada, J. M., Gallardo, M. I., Capote, R., 2009. Geant4 Interface to Work with IAEA Phase-Space Files.

Cortés-Giraldo, M. A., Quesada, J. M., Gallardo, M. I., Capote, R., 2012. An implementation to read and write iaea phase-space files in geant4-based simulations. International Journal of Radiation Biology 88, 200–208.

Dyer, P., Bodansky, D., Seamster, A. G., Norman, E. B., Maxson, D. R., 1981. Cross-sections relevant to gamma-ray astronomy-proton-induced reactions. Phys. Rev. C 23, 1865–82.

Fourkal, E., Fan, J., Veltchev, I., 2009. Absolute dose reconstruction in proton therapy using pet imaging modality:feasibility study. Phys. Med. Biol. 54, 217–28.

Friedlander, G., Kennedy, J. W., Macias, E. S., Miller, J. M., 1955. Nuclear and radiochemistry. John Wiley & Sons.

Gardner, R. P., Sood, A., 2004. A monte carlo simulation approach for generating nai detector response functions (DRFs) that accounts for non-linearity and variable flat continua. Nucl. Instrum. Methods Phys. Res. B 213 (0), 87 – 99.

Gottschalk, B., Platais, R., Paganetti, H., 1999. Nuclear interactions of 160 mev protons stopping in copper: A test of monte carlo nuclear models. Med. Phys 26, 2597–2601.

Griffin, J. J., Aug 1966. Statistical model of intermediate structure. Phys. Rev. Lett. 17, 478–481.

ICRU, 1993. Stopping Powers and Ranges for Protons and Alpha Particles. International Commission on Radiation Units and Measurements Report 49, 1993.

ICRU, 2005. Stopping of Ions Heavier than Helium. International Commission on Radiation Units and Measurements Report 73, 2005.

Jaekel, O., Reiss, P., 2007. The influence of metal artefacts on the range of ion beams. Physics in Medicine and Biology 52 (3), 635.

Janni, J. F., 1966. Calculation of energy loss, Range, Pathlength, Straggling, Multiple scattering, annd the Probability of inelastic nuclear collitions for 0.1 to 1000 mev protons. Technical report No: AFWL-TR-65-150.

Janni, J. F., 1982. Proton range energy tables, 1 kev-10gev. At. Data Nucl. Data Tables 27, 147–529.

Jarlskog, C. Z., Paganetti, H., 2008. Physics Settings for Using the Geant4 Toolkit in Proton Therapy. IEEE TRANSACTIONS ON NUCLEAR SCIENCE, 55, 1018–1025.

Kiener, J., Berheide, M., Achouri, N. L., Boughrara, A., Coc, A., Lefebvre, A., de Oliveira Santos, F., Vieu, C., Oct 1998. γ-ray production by inelastic proton scattering on ^{16}O and ^{12}C. Phys. Rev. C 58, 2174–2179.

Kim, D., Yim, H., Kim, J., 2009. Pinhole camera measurements of prompt gamma-rays for detection of beam range variation in proton therapy. J. Korean Phys. Soc. 55, 1673–6.

Knoll, G. F., 2000. Radiation Detection and Measurement. Wiley, New York.

Knopf, A., Parodi, K., Bortfeld, T., Shih, H. A., Paganetti, H., 2009. Systematic analysis of biological and physical limitations of proton beam range verification with offline pet/ct scans. Physics in Medicine and Biology 54 (14), 4477.

Knopf, A.-C., Parodi, K., Paganetti, H., Bortfeld, T., Daartz, J., Engelsman, M., Liebsch, N., Shih, H., 2011. Accuracy of proton beam range verification using post-treatment positron emission tomography/computed tomography as function of treatment site. International Journal of Radiation Oncology*Biology*Physics 79 (1), 297 – 304.

Kock, E. D., December 2007. Specification of the proton treatment nozzle in vault BG1 at ithemba labs. Medical Radiation Group, iThemba LABS, P O Box 722, Somerset West 7129, Republic of South Africa.

Kozlovsky, B., Murphy, R. J., Ramaty, R., 2002a. Nuclear deexcitation gamma-ray lines from accelerated particle interactions. The Astrophysical Journal Supplement Series 141, 523–541.

Kozlovsky, B., Murphy, R. J., Ramaty, R., 2002b. Nuclear deexcitation gamma-ray lines from accelerated particle interactions. The Astrophysical Journal 141, 523Ű541.

Krämer, M., Jäkel, O., Haberer, T., Kraft, G., Schardt, D., Weber, U., 2000. Treatment planning for heavy-ion radiotherapy: physical beam model and dose optimization. Phys. Med. Biol 45, 3299–3317.

Kumazakia, Y., Akagib, T., Yanoua, T., Suga, D., Hishikawa, Y., Teshimac, T., 2007.

Determination of the mean excitation energy ofwater from proton beam ranges. Radiat. Meas. 42, 1683–91.

Lang, F. L., Werntz, C. W., Crannell, C. J., Trombka, J. I., Chang, C. C., 1987. Cross-sections for production of the 15.10 mev and other astrophysically significant gamma-ray lines through excitation and spallation of c-12 and o-16 with protons. Phys. Rev. C 35, 1214–27.

Lara, V., Wellisch, J. P., 2000. Pre-equilibrium and equilibrium decays in Geant4. 9th Int. Conf. Calorimetry in High Energy Physics, 449–452.

Lesko, K. T., Norman, E. B., Larimer, R.-M., Kuhn, S., Meekhof, D. M., Crane, S. G., Bussell, H. G., May 1988. Measurements of cross sections relevant to γ -ray line astronomy. Phys. Rev. C 37, 1808–1817.

Liu, Z., Chen, J., Zhu, P., Li, Y., Zhang, G., 2007. The 4.438 MeV gamma to neutron ratio for the AmBe neutron source. Applied Radiation and Isotopes 65 (12), 1318 – 1321.

Lu, H.-M., 2008. A point dose method for in vivo range verification in proton therapy. Physics in Medicine and Biology 53 (23), N415.

Maccabee, H. D., Madhvanath, U., Raju, M. R., 1969. Tissue activation studies with alpha-particle beam. Phys. Med. Biol. 14, 213–24.

Matsufuji, N., Tomura, H., Futami, Y., Yamashita, H., Higashi, A., Minohara, S., Endo, M., Kanai, T., 1998. Relationship between ct number and electron density, scatter angle and nuclear reaction for hadron-therapy treatment planning. Physics in Medicine and Biology 43 (11), 3261.

Min, C., Kim, C. H., Youn, M., Kim, J., 2006. Prompt gamma measurements for locating the dose falloff region in the proton therapy. Appl. Phys. Lett. 89, 183517.

Moteabbed, M., Paganetti, H., 2011. Monte carlo patient study on the comparison of prompt gamma and pet imaging for range veri?cation in proton therapy. Phys. Med. Biol. 56, 1063.

Narayanaswamy, J., Dyer, P., Faber, S. R., Austin, S. M., 1981. Production of 6.13 mev gamma-rays from the o-16(p,p - gamma)o-16 reaction at 23.7 and 44.6 mev. Phys. Rev. C 24, 2727–30.

Newhauser, W. D., Giebeler, A., Langen, K. M., Mirkovic, D., Mohan, R., 2008. Can megavoltage computed tomography reduce proton range uncertainties in treatment plans for patients with large metal implants? Physics in Medicine and Biology 53 (9), 2327.

Paganetti, H., 2002. Nuclear interactions in proton therapy: dose and relative biological effect distributions originating from primary and secondary particles. Physics in Medicine and Biology 47 (5), 747.

Paganetti, H., 2012a. Proton Therapy Physics. CRC Press, Taylor & Franics Group.

Paganetti, H., 2012b. Proton Therapy Physics. Taylor & Francis Group.

Paganetti, H., 2012c. Range uncertainties in proton therapy and the role of Monte Carlo simulations. Phys. Med. Biol 57, R99–R117.

Paganetti, H., Gottschalk, B., 2003. Test of geant3 and geant4 nuclear models for 160 mev protons stopping in ch2. Med. Phys 30, 1926–31.

Paganetti, H., Jiang, H., Lee, S.-Y., Kooy, H. M., 2004. Accurate monte carlo simulations for nozzle design, commissioning and quality assurance for a proton radiation therapy facility. Medical Physics 31 (7), 2107–2118.

Parodi, K., Bortfeld, T., Haberer, T., 2008. Comparison between in-beam and off-line positron emission tomography imaging of proton and carbon ion therapeutic irradiation at synchrotron- and cyclotron-based facilities. International Journal of Radiation Oncology Biology Physics 71 (3), 945 – 956.

Parodi, K., Enghardt, W., Haberer, T., 2002. In-beam pet measurements of β + radioactivity induced by proton beams. Physics in Medicine and Biology 47 (1), 21.

Parodi, K., Paganetti, H., Shih, H. A., Michaud, S., Loeffler, J. S., Delaney, T. F., Liebsch, N. J., Munzenrider, J. E., Fischman, A. J., Knopf, A., Bortfeld, T., 2007. Patient study of in vivo verification of beam delivery and range, using positron emission tomography and computed tomography imaging after proton therapy. Int J Radiat Oncol Biol Phys. 68, 920–934.

Peterson, S. W., Polf, J., Bues, M., Ciangaru, G., Archambault, L., Beddar, S., Smith, A., 2009. Experimental validation of a monte carlo proton therapy nozzle model incorporating magnetically steered protons. Physics in Medicine and Biology 54 (10), 3217.

Peterson, S. W., Robertson, D., Polf, J., 2010. Optimizing a three-stage compton camera for measuring prompt gamma rays emitted during proton radiotherapy. Phys. Med. Biol. 55, 6841–56.

Polf, J. C., Panthi, R., Mackin, D. S., McCleskey, M., Saastamoinen, A., Roeder, B. T., Beddar, S., 2013. Measurement of characteristic prompt gamma rays emitted from oxygen and carbon in tissue-equivalent samples during proton beam irradiation. Physics in Medicine and Biology 58 (17), 5821.

Polf, J. C., Peterson, S., Ciangaru, G., Gillin, M., Beddar, S., 2009a. Prompt gamma-ray emission from biological tissues during proton irradiation: a preliminary study. Phys. Med. Biol. 54, 731.

Polf, J. C., Peterson, S., McCleskey, M., Roeder, B. T., Spiridon, A., Beddar, S., Trache, L., 2009b. Measurement and calculation of characteristic prompt gamma ray spectra emitted during proton irradiation. Phys. Med. Biol. 54, N519.

Richard, M. H., Chevallier, H., Dauvergne, D., Freud, N., Henriquet, P., Foulher, F. L., Letang, J. M., Montarou, G., Ray, C., Roellinghoff, F., Testa, E., Testa, M., Walenta, A. H., 2010. Design guidelines for a double scattering compton camera for prompt-gamma imaging during ion beam therapy: a Monte-Carlo simulation study. IEEE Trans. Nucl. Sci. 10.

Richard, M. H., Chevallier, M., Dauvergne, D., Freud, N., Henriquet, P., Foulher, F. L., Letang, J. M., Montarou, G., Ray, C., Roellinghoff, F., Testa, E., Testa, M., Walenta, A. H., 2009. Design study of a compton camera for prompt γ imaging during ion beam therapy. 2009 IEEE Nuclear Science Symposium Conference Record.

Rinaldi, I., Ferrari, A., Mairani, A., Paganetti, H., Parodi, K., Sala, P., 2011. An integral test of fluka nuclear models with 160 mev proton beams in multi-layer faraday cubs. Phys. Med. Biol 56, 4001–4011.

Robertson, D., Polf, J. C., Peterson, S. W., Gillin, M. T., Beddar, S., 2011. Material efficiency studies for a compton camera designed to measure characteristic prompt gamma rays emitted during proton beam radiotherapy. Physics in Medicine and Biology 56 (10), 3047.

Roellinghoff, F., Richard, M.-H., Chevallier, M., Constanzo, J., Dauvergne, D., Freud, N., Henriquet, P., Le Foulher, F., Létang, J., Montarou, G., Ray, C., Testa, E., Testa, M., Walenta, A. H., 2011. Design of a compton camera for 3d prompt-γ imaging during ion beam therapy. Nucl. Instr. Meth. A 648 (Supp. 1), S20–S23.

Schaffner, B., Pedroni, E., 1998. The precision of proton range calculations in proton radiotherapy treatment planning: experimental verification of the relation between ct-hu and proton stopping power. Physics in Medicine and Biology 43 (6), 1579.

Singh, R., Mukherjee, S. N., 1996. Nuclear reactions. New age international publishers, 312.

Smeets, J., 2011-2012. Prompt gamma imaging with a slit camera for real time range control in particle therapy. Ph.D. thesis, University of Libre de Bruxelles.

Smeets, J., Roellinghoff, F., Prieels, D., Stichelbaut, F., Benilov, A., Busca, P., Fiorini, C., Peloso, R., Basilavecchia, M., Frizzi, T., Dehaes, J. C., Dubus, A., 2012. Prompt gamma imaging with a slit camera for real-time range control in proton therapy. Phys. Med. Biol. 57, 3371–3405.

Testa, E., Bajard, M., Chevallier, M., Dauvergne, D., Foulher, F. L., Freud, N., Letang, J. M., Poizat, J. C., Ray, C., Testa, M., 2008. Monitoring the bragg peak location of 73 mev/u carbon ions by means of prompt gamma-ray measurements. Appl. Phys. Lett. 93, 093506.

Testa, M., Bajard, M., Chevallier, M., Dauvergne, D., Freud, N., Henriquet, P., Karkar, S., Foulher, F. L., Létang, J. M., Plescak, R., Ray, C., Richard, M. H., Schardt, D.,

Testa, E., 2010. Real-time monitoring of the bragg-peak position in ion therapy by means of single photon detection. Radiat. Environ. Biophys. 49, 337–43.

Tripathi, R. K., Cucinotta, F. A., Wilson, J. W., 1999. Universal parameterization of absorption cross sections:light systems. Technical Report TP-1999-209726 National Aeronautics and Space Administration (NASA).

Trofimov, A., Nguyen, P. L., Coen, J. J., Doppke, K. P., Schneider, R. J., Adams, J. A., Bortfeld, T. R., Zietman, A. L., DeLaney, T. F., Shipley, W. U., 2007. Radiotherapy treatment of early-stage prostate cancer with {IMRT} and protons: A treatment planning comparison. International Journal of Radiation Oncology*Biology*Physics 69 (2), 444 – 453.

Vacchio, S., Attanasi, F., Belcari, N., Camarda, M., Cirrone, G. A. P., Cuttone, G., 2007. A pet prototype for in-beam monitoring of proton therapy. IEEE Nucl. Sci. Symp. Conf. Record N24-362pp, 1607–11.

Verburg, J. M., Riley, K., Bortfeld, T., Seco, J., 2013. Energy- and time-resolved detection of prompt gamma-rays for proton range verification. Physics in Medicine and Biology 58 (20), L37.

Verburg, J. M., Shih, H. A., Seco, J., 2012. Simulation of prompt gamma-ray emission during proton radiotherapy. Phys. Med. Biol 57, 5459–5472.

Vitorelli, J., Silva, A., Crispim, V., da Fonseca, E., Pereira, W., 2005. Monte carlo simulation of response function for a nai(tl) detector for gamma rays from 241am/be source. Applied Radiation and Isotopes 62 (4), 619 – 622.

Wang, J., Wang, Z., Peeples, J., Yu, H., Gardner, R., 2012. Development of a simple detector response function generation program: the CEARDRFs code. Appl. Radiat. Isoy 70, 7.

Wei, J., Sandison, G. A., Hsi, W.-C., Ringor, M., Lu, X., 2006. Dosimetric impact of a ct metal artefact suppression algorithm for proton, electron and photon therapies. Physics in Medicine and Biology 51 (20), 5183.
URL `http://stacks.iop.org/0031-9155/51/i=20/a=007`

Williams, W., 1991. Nuclear and Particle Physics,. Oxford University Press, USA.